Study of metallic architected materials under mechanical and electromagnetic loads

Geoffrey Magda

INSTITUT POLYTECHNIQUE DE PARIS

NNT : 2023IPPAX138

Thèse de doctorat

ÉCOLE POLYTECHNIQUE

IP PARIS

STUDY OF METALLIC ARCHITECTED MATERIALS UNDER MECHANICAL AND ELECTROMAGNETIC LOADS

Thèse de doctorat de l'Institut Polytechnique de Paris
préparée à l'École polytechnique

École doctorale n°626 Ecole Doctorale de l'Institut Polytechnique de Paris (ED IP Paris)
Spécialité de doctorat : Mécanique des solides

Thèse présentée et soutenue à Massy, le 14/12/2023, par

GEOFFREY MAGDA

Composition du Jury :

Dennis Kochmann Professeur,ETH Zurïch	Président
Franck Vernerey Professeur, University of Colorado, Boulder	Rapporteur
Christelle Combescure Maitre de Conférence, Ecole Spéciale Militaire de Saint-Cyr	Examinateur
Laurent Rota Ingénieur, Stellantis	Examinateur
Nicolas Triantafyllidis Professeur émérite, École polytechnique (LMS)	Co-directeur de thèse
Eric Charkaluk Directeur de Recherche, CNRS (LMS)	Co-directeur de thèse

Acknowledgments

I would like to express my sincere gratitude to all those who have supported me throughout the journey of completing this thesis.

First and foremost, I am deeply thankful to my thesis advisors, Professor Nicolas Triantafyllidis and Professor Eric Charkaluk, for their time, guidance, and invaluable insights. Their mentorship has been instrumental in shaping this research.

I am also grateful to the members of my thesis committee, Professor Dennis Kochmann,Professor Franck Vernerey, Professor Christelle Combescure, and Laurent Rota, for their time, constructive feedback and expertise in evaluating this work.

I extend my appreciation to the faculty and staff of LMS, who provided a stimulating environment and resources for my research. In particular, I would like to thanks the workshop team for their very significant help with the experimental aspects.

Doing this PhD would have been far less fun without the other PhD student. To those who are yet to finish, Good luck!

My heartfelt thanks go to my family for their unwavering support and encouragement. Without their love and understanding, this journey would not have been possible.

I am fortunate to have amazing room-mates and friends who have been a constant source of motivation and positivity. Your friendship means the world to me.

Lastly, I acknowledge the financial support from DGA, which made this thesis possible.

Contents

Introduction **1**
0.1 Motivation . . . 1
0.2 Some experimental considerations . . . 2
0.3 outline . . . 4

1 Forces in Interacting Ferromagnetic Conductors Subjected to Electrical Currents and Magnetic Fields **7**
1.1 Introduction . . . 7
1.2 Theory . . . 8
1.2.1 Variational Approach . . . 9
1.2.2 Constitutive Choices . . . 14
1.2.3 Analytical Solution for a Single Conductor with Linear Magnetic Response . . . 16
1.2.4 Calculating Forces on Conductors Using Contour Integrals . . . 18
1.3 Numerical (FEM) Implementation . . . 23
1.4 Results . . . 25
1.4.1 Single Conductor Under Magnetic Field and Electric Current . . . 26
1.4.2 Two Conductors Under Magnetic Field and Same Direction Electric Currents . . . 29
1.4.3 Two Conductors Under Magnetic Field and Opposite Direction Electric Currents . . . 32
1.4.4 Periodic Array of Conductors Under Magnetic Field and Alternating Directions Electric Currents . . . 35
1.4.5 2D periodic array of conductors Subjected to Magnetic Field and Alternating Direction Electric current . . . 37
1.5 Conclusion . . . 39

2 Analysis of a partially magnetizable current carrying mesh subjected to magnetic fields **41**
2.1 Problem description . . . 42
2.1.1 Unit cell . . . 43
2.2 Principal solution . . . 45

2.3 Stability analysis . . . 46
2.3.1 Single beam . . . 47
2.3.2 Assembling of the global matrix . . . 50
2.3.3 Boundary conditions . . . 52
2.4 Results . . . 53
2.4.1 Simplified cases . . . 53
2.4.2 Complete case : Bloch analysis . . . 58
2.4.3 Beams of identical stiffness . . . 61
2.4.4 Required electromagnetic loading . . . 64
2.5 Conclusion . . . 64

3 2D layered composite with current sheets 65
3.1 Problem description . . . 66
3.2 Theory . . . 68
3.2.1 Variational principle . . . 68
3.2.2 Governing equation and interface conditions . . . 69
3.3 Principal solution . . . 71
3.4 Stability analysis . . . 75
3.4.1 Problem simplification . . . 75
3.4.2 Analytical solution to the stability problem . . . 77
3.5 Results . . . 81
3.5.1 Purely mechanical loading . . . 81
3.5.2 Electric and magnetic loading under no axial stretch . . . 84
3.5.3 Impact of electric and magnetic loading on the buckling caused by axial compression . . . 84
3.6 Conclusion and future work . . . 87

Conclusion 89

A Complete formulation of the energy in the case of the composite 91

Résumé en francais 99

Bibliography 104

List of Figures

1 Depiction of the Electromagnet in both configurations 3
2 wire mesh composed of magnetizable current carrying beams and softer plastic beams under external magnetic load 3
3 Schematics of the Electromagnet for both measurement methods . . . 4

1.1 Schematics of the boundary value problem (reference configuration). Conductor occupies domain $\Omega \subset \mathbb{R}^3$ while a magnetic field exists in the entire space $\mathbb{R}^3$. 9
1.2 Non linear magnetization law in dimensionless form: magnetization as a function of applied h-field. 16
1.3 Cross section of a cylindrical conductor of radius R subjected to a current of uniform density $\boldsymbol{j} = j\boldsymbol{e}_z$ and a remote h-field of magnitude $\boldsymbol{h}_0 = h_0\boldsymbol{e}_y$ 17
1.4 Calculating the Lorentz forces $\boldsymbol{F}_{L}$ on a conductor subjected to a current of density j and a remote h-field of magnitude h_0 using contour integrals. 19
1.5 Calculating the Lorentz forces on two parallel conductors subjected to same or opposite direction currents of density j and a remote h-field of magnitude h_0 using contour integrals. 21
1.6 Calculating the Lorentz forces on parallel conductors subjected to same or alternating direction currents of density j and a remote h-field of magnitude h_0 in an infinite array using contour integrals. . . . 22
1.7 Typical FEM meshes used for calculating the magnetic potential a inside and outside the conductor domain. In (a) for a single conductor of radius R and in (b) for two conductors of same radius R at a distance $D = 4R$. 24
1.8 Contours of the magnetic field norm $\|\boldsymbol{m}\|/m_s$ for a conductor subjected to an electric current and a remote magnetic field. In (a) for low remote magnetic field $b_0 = 0.52{\times}10^{-4}\ b_{ref}$ and current $j = 2{\times}10^{-4}\ j_{ref}$ where the entire section is in the near-linear regime of magnetization. In (b) for high remote magnetic field $b_0 = 0.66\ b_{ref}$ and current $j = 5.25\ j_{ref}$, where the entire conductor is near the saturation regime of magnetization. 26

1.9 Contours for the dimensionless magnetic stress $\overset{m}{\boldsymbol{\sigma}}/\mu_0 m_s^2$ components for a conductor subjected to an electric current and a remote magnetic field. Low remote magnetic field $b_0 = 0.52\times10^{-4}\ b_{ref}$ and current $j = 2\times10^{-4}\ j_{ref}$ where the entire section is in the near-linear regime of magnetization. 27

1.10 Contours for the dimensionless magnetic stress $\overset{m}{\boldsymbol{\sigma}}/\mu_0 m_s^2$ components for a conductor subjected to an electric current and a remote magnetic field. For high remote magnetic field $b_0 = 0.66\ b_{ref}$ and current $j = 5.25\ j_{ref}$, where the entire conductor is near the saturation regime of magnetization. 28

1.11 Dimensionless forces per unit length $F_{L}^{1,2}/F_{ref}$ as function of the remote magnetic field b_0/b_{ref} and the current density j/j_{ref} on two conductors with equal, same direction parallel currents $I = \pi j R^2$; in (a) at distance $D/R = 4$ and in (b) at distance $D/R = 20$. Lorentz force for the single conductor $-b_0 I/F_{ref}$ depicted in green for comparison. . 29

1.12 Influence of distance D/R on the dimensionless force per unit length $F_{L}^{1,2}/F_{ref}$ between two conductors with equal, same direction parallel currents $I = \pi j R^2$ as a function of the remote magnetic field b_0/b_{ref} at two different current densities; in (a) for $j/j_{ref} = 0.42$ and in (b) for $j/j_{ref} = 6.36$. Results for conductor 1 (left) are plotted in dashed lines while for conductor 2 (right) are plotted in solid lines (see Figure 1.5). 31

1.13 Dimensionless forces per unit length $F_{L}^{1,2}/F_{ref}$ as function of the remote magnetic field b_0/b_{ref} and the current density j/j_{ref} on two conductors with equal, opposite direction parallel currents $I = \pi j R^2$ for $\boldsymbol{j}_1 = j\boldsymbol{e}_z$, $\boldsymbol{j}_2 = -j\boldsymbol{e}_z$ (case i, (a) and (b)) and $\boldsymbol{j}_1 = -j\boldsymbol{e}_z$, $\boldsymbol{j}_2 = j\boldsymbol{e}_z$ (case ii, (c) and (d)); in (a) and (c) at distance $D/R = 4$ and in (b) and (d) at distance $D/R = 20$. Lorentz force for the single conductor $-b_0 I/F_{ref}$ depicted in green for comparison. 32

1.14 Influence of distance D/R on the dimensionless force per unit length $F_{L}^{1,2}/F_{ref}$ between two conductors with equal, opposite direction parallel currents $I = \pi j R^2$ for $\boldsymbol{j}_1 = j\boldsymbol{e}_z$, $\boldsymbol{j}_2 = -j\boldsymbol{e}_z$ (case i, (a) and (b)) and $\boldsymbol{j}_1 = -j\boldsymbol{e}_z$, $\boldsymbol{j}_2 = j\boldsymbol{e}_z$ (case ii, (c) and (d)) as a function of the remote magnetic field b_0/b_{ref} at two different densities; in (a) and (c) for $j/j_{ref} = 0.42$ and in (b) and (d) for $j/j_{ref} = 6.36$. Results for conductor 1 (left) are plotted in dashed lines while for conductor 2 (right) are plotted in solid lines (see Figure 1.5). 34

1.15 Dimensionless forces per unit length $F_{L}^{1,2}/F_{ref}$ as function of the remote magnetic field b_0/b_{ref} and current density j/j_{ref} in an infinite array of equally spaced conductors with alternating direction parallel currents $I = \pi j R^2$; in (a) at distance $D/R = 4$ and in (b) at distance $D/R = 20$. Lorentz force for the single conductor $-b_0 I/F_{ref}$ depicted in green for comparison. 35

1.16 Influence of distance D/R on the dimensionless force $F_{L}^{1,2}/F_{ref}$ between two adjacent conductors in an infinite array with alternating direction parallel currents $I = \pi j R^2$ as a function of the remote magnetic field b_0/b_{ref} at two different current densities; in (a) for $j/j_{ref} = 0.42$ and in (b) for $j/j_{ref} = 6.36$. Results for conductor 1 (left) are plotted in dashed lines while for conductor 2 (right) are plotted in solid lines (see Figure 1.6). 36
1.17 Calculating the Lorentz forces F_L on a a 2D array of conductor subjected to current of density j of alternating direction and a remote h-field of magnitude h_0 using contour integrals. 38
1.18 Dimensionless forces per unit length $F_{L}^{1,2}/F_{ref}$ as function of the remote magnetic field b_0/b_{ref} and current density j/j_{ref} in an infinite array of equally spaced conductors with alternating direction parallel currents $I = \pi j R^2$; a) at distance $D/R = 4$ and b) at distance $D/R = 20$. Lorentz force for the single conductor $-b_0 I/F_{ref}$ depicted in green for comparison purposes. 38

2.1 Schematic of an infinite mesh under an exterior magnetic field and currents. The red beams are magnetizable conductors carrying the current. The black ones are non conductive and non magnetizable. . . 43
2.2 Schematic of the unit cell with the numbering of the points, the d.o.f and the geometrical parameters 44
2.3 Principal solution for the unit cell under the considered load. The faded red beams indicate the reference configuration 47
2.4 Schematic of an axially loaded beam and its d.o.f 48
2.5 K and ζ_c values for various boundary conditions and related buckling modes for slender beams 54
2.6 lowest eigenvalue (except rigid body) of the reduced stiffness matrix under periodic boundary conditions depending on the loading ζ . . . 57
2.7 schematic of the critical mode for periodic boundary conditions . . . 57
2.8 $\zeta_m(\omega_x, \omega_y)$ using bloch boundary conditions for $l_v = l_h = 3cm$, $r_h = 1.5mm$, $r_v = 0.75mm$, $E_h = 210$GPa and $E_v = 2$GPa. The full range of pulsation are $\omega_{x,red} = \omega_x L_x \in [0, 2\pi]$ and $\omega_{y,red} = \omega_y L_y \in [0, 2\pi]$ . . 58
2.9 $\zeta_m(\omega_x, \omega_y)$ using bloch boundary conditions for $l_v = l_h = 3cm$, $r_h = 1.5mm$, $r_v = 0.75mm$, $E_h = 210$GPa and $E_v = 2$GPa. The full range of pulsation are$\omega_{x,red} = \omega_x L_x \in [0, 0.012]$ and $\omega_{y,red} = \omega_y L_y \in [0, \pi]$ . . 59
2.10 critical load ζ for various values of l_h and l_v and $r_h = 1.5mm$, $r_v = 0.75mm$, $E_h = 210$GPa and $E_v = 2$GPa. 60
2.11 schematic of the critical mode for bloch boundary conditions, $\omega_x = 0$ and $\omega_y = \pi/L_y$ 62
2.12 critical load ζ for various values of l_h and l_v and $r_h = r_v = 1.5mm$ and $E_h = E_v = 210$GPa 63

3.1 Schematic of the composite under consideration. The fibers are represented in dark grey, the matrix in light grey. The electromagnetic loading is composed of an external magnetic field b_{ext} and currents I . 67
3.2 Schematic of the composite unit cell under consideration. The fibers are represented in dark grey, the matrix in light grey. The electromagnetic loading is composed of an external magnetic field b_{ext} and surface currents κ. The h-field in reference configuration is plotted in blue. 67
3.3 Principal solution considering 10% of steel fiber ($E_f = 210$ GPa, $\nu_f = 0.3$) and 90% od plastic matrix ($E_m = 20$ MPa and $\nu_m = 0.4$) for b_{ext}=1T 74
3.4 Principal solution considering 10% of steel fiber ($E_f = 210$ GPa, $\nu_f = 0.3$) and 90% od plastic matrix ($E_m = 20$ MPa and $\nu_m = 0.4$) for κ=25000A/m 74
3.5 Different types of bifurcation modes in axially compressed layered media. Taken from Santisi d'Avila et al. (2016) 78
3.6 Solid line : Dependence of the microscopic (I) and macroscopic (II) critical stretch ratio λ on the fiber volume fraction V_f for the hyperelastic composite with $\mu_m/\mu_f = 0.07$ (Taken from Triantafyllidis and Maker (1985) Fig.6) Red dots : global buckling results obtained using the previously described method. Green dots : local buckling results obtained using the previously described method. 82
3.7 Solid line :Dependence of the critical stretch ratio X on the non-dimensionalized eigenmode frequency ω H for the hyperelastic composite with $\mu_m/\mu_f = 0.07$, $V_f = 0.1$ (Taken from Triantafyllidis and Maker (1985) Fig.5) Green dots : same but using the previously described method. 83
3.8 Dependence of the macroscopic critical stretch ratio λ_1 on the fiber volume fraction V_f for the hyperelastic composite with ($E_f = 210$ GPa, $\nu_f = 0.3$,$E_m = 20$ MPa and $\nu_m = 0.4$) for various magnetic loading. 85
3.9 Dependence of the macroscopic critical stretch ratio λ_1 on the pulsation ω_1 H for the hyperelastic composite with ($E_f = 210$ GPa, $\nu_f = 0.3$,$E_m = 20$ MPa and $\nu_m = 0.4$) for various magnetic loading and a fiber volume fraction V_f of 0.1. The orange line is slightly above the red one. The bleu line is slightly above the green line. . . . 86

List of Tables

1 summary of the experimental constrains 4

2.1 Summary of critical load for various geometry and their related magnetic requirement 64

3.1 range of the various parameters considered when looking for potential buckling mode 84

Introduction

0.1 Motivation

Mechanical metamaterials have attracted a strong interest, fueled largely by the transport industry, where composites and honeycomb's exceptional stiffness-to-mass ratios are greatly appreciated. Early work focused mainly on metamaterials showing exceptional mechanical properties according to classical criteria such as strength or stiffness.

More recently, these ideas have been extended to functional metamaterials that have the possibility to change their properties when subjected to non-mechanical external loadings. One such example is the application of magnetic fields to a specially designed metallic-rubber composites, obtained by embedding magnetizable iron particles in a polymeric matrix to create magnetorheological elastomers. Other techniques have also been proposed to create magneto-mechanical coupling in solids using permanent magnets Slesarenko (2020). In addition to metamaterials involving magneto-mechanical couplings, applications have also been proposed involving coupling between mechanical and electric properties (e.g. electroactive composites Kumar et al. (2020)).

However, to the best of the author's knowledge, there is very little work on applications involving current carrying magnetizable metamaterials, thus motivating the present investigation. As the ecological transition is driving up the number of systems carrying high electrical power densities, exploring the potential of using lightweight architected metamaterials seems of great interest. The objective of this thesis is to explore the response of magnetizable metamaterials under external magnetic fields, currents and mechanical loadings.

Solving such problems first requires knowledge of the magneto mechanical constitutive laws of the material. This is a widely investigated research area but not the main focus of this thesis, where we will consider some simple, non-hysteretic magneto-mechanical constitutive laws. The second important element of this thesis is a consistent coupled formulation of the problem. One approach, commonly found in the field of electrical engineering (see for instance Reyne et al. (1988)) for the couple analysis of an electrical engine) , is to solve the mechanical and magnetic problem separately in a stepwise process. To avoid the inconsistencies of this ap-

proach, Hanappier et al. (2022) have recently proposed coupled magneto-mechanics variational principles that form the basis for robust numerical solution algorithms. Using the direct approach of continuum mechanics, a general framework that couples the electromagnetic and mechanical fields is derived for the applications of interest here, using the basic principles of thermodynamics.

As an application to the general theory, two different designs will be considered as simple metamaterials involving electric current-carrying magnetizable conductors subjected to external magnetic fields: a planar grid and a two dimensional layer of magnetizable metallic sheets separated by elastomeric layers. The never before addressed (to the best of the author's knowledge) problem of the influence of magnetic response of the conductors on the Lorentz forces in the grid is the object of a separate investigation.

Moreover, and given that nonlinear geometric effects are important in architected metamaterials (large strains are possible in the applications of interest), one has also to consider the stability of these materials when subjected to external loads. The stability of the two different designs considered has been addressed using Bloch wave theory, given the periodic geometry of the composites considered. Limitations of the simple designs considered here have been established and ideas for further research based on the general methodology introduced are being proposed.

0.2 Some experimental considerations

To test our analytical and numerical results, we were expecting to use the experimental setup available at the Laboratoire de Mécanique des Solides (LMS). In the end, due to both the values obtained by numerical simulation and experimental constraints, a proper experimental campaign has not been carried out, but as those experimental constraints guided our choice of parameters for the first two chapters, we have to clarify what those constraints were.

As the point is to mix exterior magnetic field and electrical current, the electromagnet and current generator have been the two most critical elements. The electromagnet displayed in Figure 1a has two possible configurations : one with a air gap of 1 cm length and a region of uniform field corresponding to a circle of radius 1 cm, and a second one with a air gap of 8.2 cm length and a region of uniform field corresponding to a circle of radius 4.5 cm. The region of homogeneous field is a strong constraint as it imposes the maximum size of the system to study. The maximal value achieved by the magnetic field also depends on the configuration: 0.8 Tesla for the large configuration, and 2T for the narrow one. To generate current, we can use a DC current generator that can achieve constant currents up to 40 A.

The sample considered for those potential experiment was a mesh as shown in Figure 2. It is composed of two types of beams: In grey, magnetizable current carrying beams that generates the forces, but as they are metallic, they are too stiff to generates interesting mechanical behaviour. In green, soft plastic beams will show

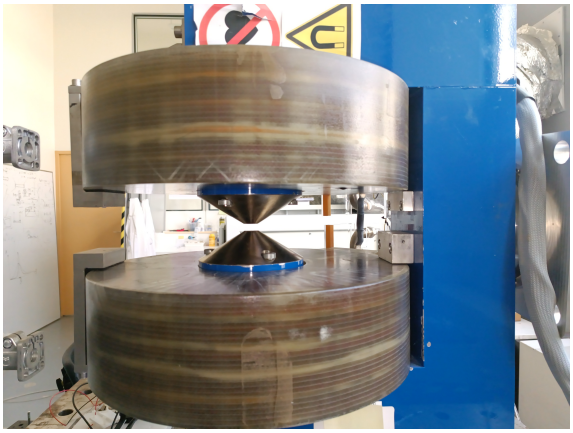

(a) Electromagnet available using the strong field small volume configuration

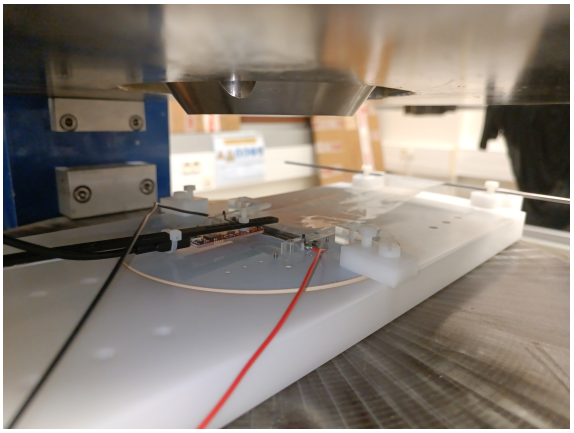

(b) Experimental setup using the weaker field and larger volume configuration

Figure 1: Depiction of the Electromagnet in both configurations

more significant deformation and are transparent in the electromagnetic problem. When considering only the metallic wires, we will use the term beam array. When considering all the wires we will use the term mesh.

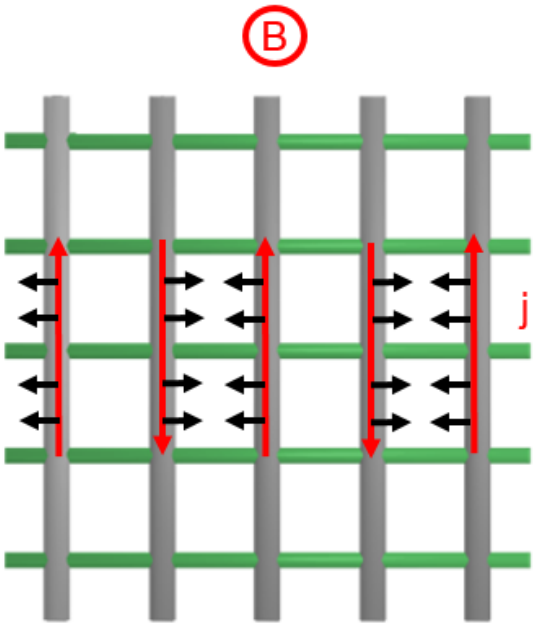

Figure 2: wire mesh composed of magnetizable current carrying beams and softer plastic beams under external magnetic load

To measure the obtain impact of the electro-magnetic loading, two approaches

have been considered : first, as depicted in Figure 3a, using a camera and digital image correlation to obtain the displacement field, and thus the forces. Second, transferring the forces vertically with a thin plastic sheet and finding the weight that equilibrate the system as depicted in Figure 1b and Figure 3b. We implemented the second system to check the orders of magnitude, not to provide actual usable scientific data as it is not precise enough.

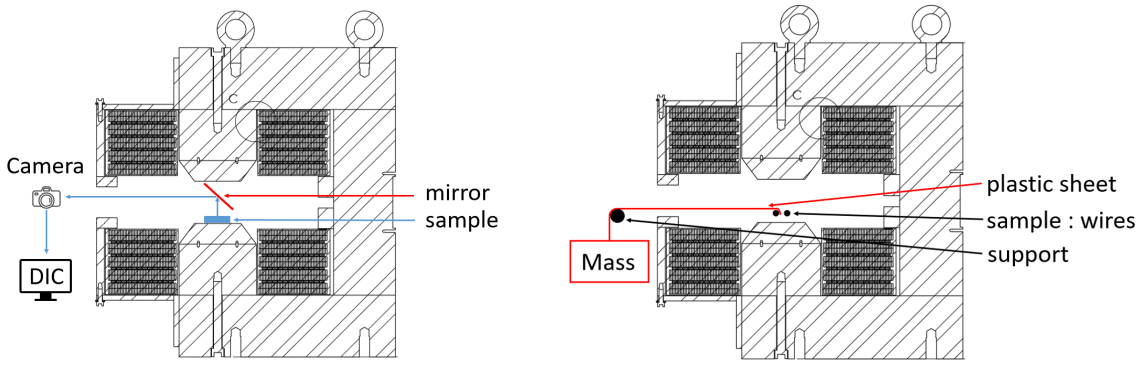

(a) schematics of the setup considered to use DIC

(b) schematics of the setup considered to use mass

Figure 3: Schematics of the Electromagnet for both measurement methods

To summarize, we provide in Table 1 the key experimental constraints.

configuration	close	far
max current (A)	40	40
max magnetic field (T)	2	0.8
max vertical dimension (cm)	1	8,2
max horizontal dimension (cm)	2	9

Table 1: summary of the experimental constrains

0.3 outline

The goal of the current thesis is to explore the possibilities offered by magneto-mechanical metallic metamaterials with non-linear magnetization laws, under both external magnetic fields and electric currents. The novelty of the present work lies in the fact that no previous work has addressed electric current carrying and magnetizable metamaterials, to the best of the author's knowledge.

We provide a general, coupled magneto-mechanical model for this problem in Chapter 1, with some adjustment in Chapter 3 for the case when an external magnetic

field is imposed in current configuration. As an application to the general theory, two different designs will be considered as simple metamaterials involving electric current-carrying magnetizable conductors subjected to external magnetic fields: a planar grid and a two dimensional layer of ferromagnetic sheets separated by elastomeric layers.

In Chapter 1 we address the problem of the influence of magnetic response of the conductors on the Lorentz forces generated between them for the case of two parallel conductors and also for the case of infinite arrays of parallel conductors. A surprising find of this investigation is that in the case of an infinite array of same direction parallel conductors their magnetic properties have no influence at all, while for an infinite array of alternating direction parallel conductors the Lorentz forces are lower than in the case of non-magnetizable materials!

In Chapter 2 we study a square unit-cell geometry current-carrying planar truss under an external magnetic field perpendicular to its plane. We investigate the principal solution and its stability and find the instability patterns for an infinite grid.

Finally, in Chapter 3, we investigate the case of a 2D fully coupled composite made of magnetizable conductive layers connected by non-conductive elastomeric layers under an external magnetic field, currents, and mechanical loadings. For this analytically tractable, simple geometry we find that the current, and to a lesser extent the external magnetic field, have only a minor impact on the principal solution and its stability, unlike the imposed axial compression.

With the present thesis we show that using electric currents and magnetic fields to control the behavior of new metamaterials is possible. In the simple geometries considered here, obtaining significant mechanical effects requires unrealistically high electric currents and magnetic fields. However, different, more complex geometries can be analyzed, where lower currents are required to obtain significant overall mechanical strains, such as in solenoids (see Elliott and Triantafyllidis (2023)). It would be interesting to investigate different composite geometries that might enhance the electro-mechanical coupling and investigate the stability of such designs, based on the general theory proposed here.

Chapter 1

Forces in Interacting Ferromagnetic Conductors Subjected to Electrical Currents and Magnetic Fields

1.1 Introduction

We revisit here the topic of Lorentz forces on electrical current carrying conductors subjected to a remote magnetic field with particular attention to the influence of the conductors' magnetic properties is an interesting topic. The case of a single conductor has been discussed by Lowes (1973) who shows that the Lorentz force per unit length is independent of magnetic properties as well of the shape of the conductor for the case of a conductor placed in a uniform magnetic field perpendicular to its axis. The same result is obtained by Casperson (2002) who in addition presents some careful experiments to back the same conclusion.

The magnetization law of common ferromagnetic conductors have been the subject of many research, with plenty of approaches: multi scale vs energetical (Aydin et al. (2017)), varied formulation : direct (Kovetz (2000)) or variational (Hanappier et al. (2022)), and various effect considered : magnetostriction (Anderson et al. (2007)), Villari effect (Bieńkowski and Kulikowski (1980)), dissipation (Perevertov (2017)), anisotropy (Lopez et al. (2009)), impact of residual stresses (Baudouin et al. (2002)), multi axial loading (Pearson et al. (2000), Daniel and Hubert (2009)) and dynamic behavior (Bao et al. (2017)) to name only a few. As explained in the introduction, as this is not the primary focus of this work, we use a simple model proposed by Danas (2017).

They are several methods to obtain the electromagnetic resultant forces, and the interested reader could find an extensive review in (McDonald (2003)) . We are going to use the maxwell tensor contour integral that avoid having to consider

simultaneously the integral of bulk forces and the integral of surfaces forces. This requires to obtain maxwell stress tensor and thus a magneto mechanical constitutive law for the material considered. Obtaining the maxwell stress will be discussed in detail in Section 1.2, but the key insight come from (Kovetz (2000), Hanappier et al. (2021), Hanappier et al. (2022) and Thomas and Triantafyllidis (2009)).

Finally, some literature exist relating to the interaction between wires : Magnetizable nano wire embedded in materials have been studied as well as the impact of their interaction on the magnetization law have been a subject of several research such as Raposo et al. (2000). But thoses wires do not carry current, and the resultant forces are not considered, only the impact on magnetization. The mechanical behaviour and stability of current carrying wire array have been studied as part of the development of Z-pinch technique (see for instance Hammer and Ryutov (1999)), but those works do not consider magnetization of the wires, and the regime is very different (μm wires, Mega amperes of current, very strong thermal effect, etc...)

However, the influence of magnetic constitutive law on the forces between two or more (periodic array) parallel conductors subjected to a uniform external magnetic field and current density has received considerably less attention to the best of the author' knowledge and is the main object of study of this work.

The outline of this chapter is a follows: after the motivation in Section 1.1 comes the general variational theory of the eddy current approximation in Section 1.2. The stresses are subsequently simplified for the case of small strains but arbitrary magnetic fields and then applied to the analytically tractable case of a single conductor with linear magnetic response subjected to an electric current and a magnetic field. We then give an efficient way to calculate the total force on a conductor using contour integrals (see Lowes (1973)). The numerical implementation is given in Section 1.3 followed by the applications in Section 1.4. For a single conductor, where the magnetic properties do not influence the force exerted, we calculate the magnetization and magnetic stress fields. For two parallel conductors the magnetic properties affect significantly the Lorentz forces when the conductors are placed close to each-other, as the magnetic fields outside them are significantly influenced by the conductors' magnetic response. For the case of an infinite array of parallel conductors there is no influence of their magnetic properties on the Lorentz forces when same direction currents are applied while only a small magnetic effect is found for currents applied in alternating directions, even for closely spaced conductors. Conclusion is presented in Section 1.5.

1.2 Theory

Coordinate-free (dyadic) continuum mechanics notation is used with bold symbols referring to tensors and script ones to scalars; all field quantities are functions of the reference position $\boldsymbol{X}$ and when appropriate on time t. Lagrangian field quantities are denoted by capital letters, e.g. magnetic potential $\boldsymbol{A}$, magnetic flux $\boldsymbol{B}$, h-field $\boldsymbol{H}$,

current density $\boldsymbol{J}$, first Piola-Kirchhoff stress $\boldsymbol{\Pi}$, while their corresponding Eulerian counterparts are denoted by script letters, e.g. magnetic potential $\boldsymbol{a}$, magnetic flux $\boldsymbol{b}$, h-field $\boldsymbol{h}$, current density $\boldsymbol{j}$, Cauchy stress $\boldsymbol{\sigma}$[1]. Moreover, the gradient operator $\boldsymbol{\nabla}$ is defined with respect to the reference configuration, i.e. $\boldsymbol{\nabla} \equiv \partial/\partial \boldsymbol{X}$, while its current configuration counterpart is $\boldsymbol{\nabla} \equiv \partial/\partial \boldsymbol{x}$.

1.2.1 Variational Approach

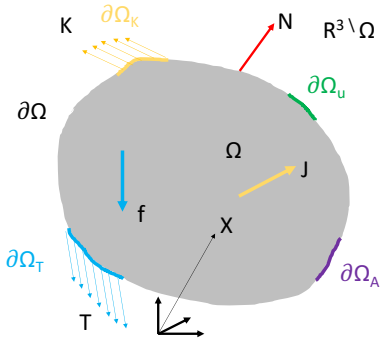

Figure 1.1: Schematics of the boundary value problem (reference configuration). Conductor occupies domain $\Omega \subset \mathbb{R}^3$ while a magnetic field exists in the entire space $\mathbb{R}^3$.

The schematics of the general boundary value problem are given in Figure 1.1. The solid occupies a volume $\Omega \subset \mathbb{R}^3$ in the reference configuration with boundary $\partial\Omega$ and an outward normal $\boldsymbol{N}$. The solid is subjected to a reference current density $\boldsymbol{J}$ and an externally applied mechanical body force (per unit mass) $\boldsymbol{f}$. On the boundary we apply a mechanical traction $\boldsymbol{T}$ and a current sheet $\boldsymbol{K}$ (per unit reference surface area). Surface tractions are applied on part of the boundary $\partial\Omega_T$ and the current sheet on part of the boundary $\partial\Omega_K$; displacement $\boldsymbol{u}$ and magnetic potential $\boldsymbol{A}$[2] can also be applied on parts of the boundary $\partial\Omega_u$ and $\partial\Omega_A$ respectively [3].

Neglecting the electric charge and the electric field energy contributions, the reference configuration "*Lagrangian density*" $\mathscr{\ell}$ (per unit reference volume) for the

[1]The capital-script letter rule is not applicable to field quantities relating the two configurations, where no ambiguity is possible and hence the usual standard notation is adopted, i.e. $\boldsymbol{F}$ for the deformation gradient or $\boldsymbol{u}$ for the displacement field.

[2]The Dirichlet condition in magnetics consists of prescribing $\boldsymbol{N} \times \boldsymbol{A}$.

[3]This formulation assume an external loading in reference configuration. If the loadings are in current configuration, this variational approach has to be slightly altered. We will provide the adaptation in Chapter 3 in the case where an external magnetic field is applied in current configuration. In this chapter this adaptation is not necessary as we will assume small strain, so loadings in reference of current configuration will provide identical results.

eddy current approximation (see Thomas and Triantafyllidis (2009)) is given by

$$\ell \equiv -\frac{1}{2\mu_0 J}\boldsymbol{B}\cdot\boldsymbol{C}\cdot\boldsymbol{B}+\boldsymbol{J}\cdot\boldsymbol{A}-\rho_0\psi(\boldsymbol{C},\boldsymbol{B})+\frac{1}{2}\rho_0(\dot{\boldsymbol{u}}\cdot\dot{\boldsymbol{u}})+\rho_0\boldsymbol{f}\cdot\boldsymbol{u}\ ; \quad \boldsymbol{B}\equiv\boldsymbol{\nabla}\times\boldsymbol{A}\ ,\ \boldsymbol{C}\equiv\boldsymbol{F}^T\cdot\boldsymbol{F}\ , \tag{1.2.1}$$

where $\boldsymbol{B}$ the reference magnetic field, $\boldsymbol{A}$ the reference magnetic potential[4], $\psi(\boldsymbol{C},\boldsymbol{B})$[5] the specific (per unit mass) Helmholtz free energy and $\boldsymbol{C}$ the right Cauchy-Green tensor, expressed in terms of the deformation gradient $\boldsymbol{F}$. Following standard notation, ρ_0 is the reference mass density of the solid and $\dot{\boldsymbol{u}}$ denotes the time-derivative (velocity) of the displacement $\boldsymbol{u}$. Moreover, μ_0 is the magnetic permeability of vacuum and $J=\det(\boldsymbol{F})$ denotes the deformation-induced volume change.

Based on (1.2.1), the reference configuration "*total Lagrangian*" $\mathscr{L}$ of the system becomes[6]

$$\mathscr{L}\equiv\int_{\mathbb{R}^3}\ell\ \mathrm{d}V+\int_{\partial\Omega}[\boldsymbol{T}\cdot\boldsymbol{u}+\boldsymbol{K}\cdot\boldsymbol{A}]\ \mathrm{d}S\ . \tag{1.2.2}$$

We also generalize the reference mass density ρ_0 in the definition of the Lagrangian density ℓ in (1.2.1) over the entire space $\mathbb{R}^3$ as follows: $\rho_0(\boldsymbol{X})\neq 0$ for $\boldsymbol{X}\in\Omega$ and $\rho_0(\boldsymbol{X})=0$ for $\boldsymbol{X}\in\mathbb{R}^3\backslash\Omega$. Integration over $\mathbb{R}^3$ is necessary to account for the electromagnetic field in both the body Ω and its surrounding space $\mathbb{R}^3\backslash\Omega$.

We proceed with the definition of the "*action integral*" $\mathscr{F}(\boldsymbol{A},\boldsymbol{u})$, obtained by integration of the Lagrangian $\mathscr{L}$ in (1.2.2) between arbitrary times t_1 and t_2. By Hamilton's principle it is stationary

$$\begin{aligned}\mathscr{F}(\boldsymbol{A},\boldsymbol{u})\equiv\int_{t_1}^{t_2}\mathscr{L}\ \mathrm{d}t\ , \quad \delta\mathscr{F}=0\\ ; \quad \delta\boldsymbol{A}(t_i)=\delta\boldsymbol{u}(t_i)=\boldsymbol{0}\ ,\ i=1,2\implies \mathscr{F}_{,\boldsymbol{A}}[\delta\boldsymbol{A}]=\mathscr{F}_{,\boldsymbol{u}}[\delta\boldsymbol{u}]=0\ .\end{aligned} \tag{1.2.3}$$

Consequently the corresponding variations with respect to the independent variables $\boldsymbol{A}$ and $\boldsymbol{u}$ yield respectively the magnetic and mechanical governing equations and interface/boundary conditions.

[4] An additional condition is needed for a unique $\boldsymbol{A}$, termed "*gauge condition*"; Coulomb gauge $\boldsymbol{\nabla}\cdot\boldsymbol{A}=0$ is a typical choice.

[5] Dissipative phenomena (e.g. magnetic hysteresis or plasticity) are ignored and thus no internal variables are needed in ψ. Temperature dependance is ignored as well. The specific free energy used here depends on $(\boldsymbol{C},\boldsymbol{B}=J\boldsymbol{F}^{-1}\cdot\boldsymbol{b})$, as opposed to $(\boldsymbol{C},\boldsymbol{b}\cdot\boldsymbol{F})$ in Hanappier (2021); Hanappier et al. (2021, 2022); Kovetz (2000). Our choice, motivated by the fact that $\boldsymbol{B}$ is the Lagrangian counterpart of Eulerian $\boldsymbol{b}$, still complies with the angular momentum balance argument made in Kovetz (2000). For a detailed explanation of this point, see Hanappier (2021).

[6] Without loss of generality, we can define the applied mechanical traction $\boldsymbol{T}$ and current sheet $\boldsymbol{K}$ on the entire boundary and impose a zero value when applicable.

Magnetics Equations: Variations with Respect to Magnetic Potential $\boldsymbol{A}$

Lagrangian version

Following (1.2.3), setting to zero the variation of $\mathscr{F}$ with respect to $\boldsymbol{A}$ one obtains

$$\mathscr{F}_{,\boldsymbol{A}}[\delta\boldsymbol{A}] = \int_{t_1}^{t_2} \left\{ \int_{\mathbb{R}^3} \left[\boldsymbol{J}\cdot\delta\boldsymbol{A} - \frac{1}{\mu_0}(\boldsymbol{B}\cdot\boldsymbol{C})\cdot(\boldsymbol{\nabla}\times\delta\boldsymbol{A}) - \rho_0\frac{\partial\psi}{\partial\boldsymbol{B}}\cdot(\boldsymbol{\nabla}\times\delta\boldsymbol{A}) \right] \mathrm{d}V + \int_{\partial\Omega} [\boldsymbol{K}\cdot\delta\boldsymbol{A}]\,\mathrm{d}S \right\} \mathrm{d}t = 0\,. \tag{1.2.4}$$

The domain $\mathbb{R}^3$ is separated into the volume Ω occupied by the body and the surrounding space $\mathbb{R}^3\backslash\Omega$. Taking into account the discontinuity of ρ_0 across $\partial\Omega$, integration by parts of (1.2.4) yields

$$\mathscr{F}_{,\boldsymbol{A}}[\delta\boldsymbol{A}] = \int_{t_1}^{t_2} \left\{ \int_{\mathbb{R}^3} \left[(\boldsymbol{J} - \boldsymbol{\nabla}\times\boldsymbol{H})\cdot\delta\boldsymbol{A} \right] \mathrm{d}V + \int_{\partial\Omega} \left[(\boldsymbol{K} - \boldsymbol{N}\times[\![\boldsymbol{H}]\!])\cdot\delta\boldsymbol{A} \right] \mathrm{d}S \right\} \mathrm{d}t = 0\,, \tag{1.2.5}$$

where $\boldsymbol{H}$ is the reference configuration "*h-field*" (see Hanappier (2021)) and is given by

$$\boldsymbol{H} \equiv -\frac{\partial\mathscr{\ell}}{\partial\boldsymbol{B}} = \begin{cases} \rho_0\dfrac{\partial\psi}{\partial\boldsymbol{B}} + \dfrac{1}{\mu_0 J}\boldsymbol{C}\cdot\boldsymbol{B}\,; & \forall\,\boldsymbol{X}\in\Omega\,, \\[2ex] \dfrac{1}{\mu_0 J}\boldsymbol{C}\cdot\boldsymbol{B}\,; & \forall\,\boldsymbol{X}\in\mathbb{R}^3\backslash\Omega\,. \end{cases} \tag{1.2.6}$$

The arbitrariness of $\delta\boldsymbol{A}$, (1.2.6) implies the following differential equation and boundary/interface condition

$$\boldsymbol{\nabla}\times\boldsymbol{H} = \boldsymbol{J}\,; \quad \forall\boldsymbol{X}\in\mathbb{R}^3\,, \qquad \boldsymbol{N}\times[\![\boldsymbol{H}]\!] = \boldsymbol{K}\,; \quad \forall\boldsymbol{X}\in\partial\Omega\,, \tag{1.2.7}$$

where one recognizes the reference configuration Maxwell-Ampère law in the eddy current approximation.

To the above governing equation and boundary condition for $\boldsymbol{H}$ one should also add its counterpart for the reference configuration magnetic field $\boldsymbol{B}$, a consequence of (1.2.1)

$$\boldsymbol{\nabla}\cdot\boldsymbol{B} = \boldsymbol{0}\,; \quad \forall\boldsymbol{X}\in\mathbb{R}^3\,, \qquad \boldsymbol{N}\cdot[\![\boldsymbol{B}]\!] = \boldsymbol{0}\,; \quad \forall\boldsymbol{X}\in\partial\Omega\,, \qquad (\boldsymbol{B} = \boldsymbol{\nabla}\times\boldsymbol{A})\,. \tag{1.2.8}$$

Eulerian version

The reference configuration h-field, magnetic potential and field and current sheet are related via the deformation gradient $\boldsymbol{F}$ to their current configuration counterparts by (e.g. see Lax and Nelson (1976))

$$\boldsymbol{A} = \boldsymbol{a}\cdot\boldsymbol{F}\,, \qquad \boldsymbol{H} = \boldsymbol{h}\cdot\boldsymbol{F}\,, \qquad \boldsymbol{B} = J\boldsymbol{F}^{-1}\cdot\boldsymbol{b}\,, \qquad \boldsymbol{K} = J\boldsymbol{F}^{-1}\cdot\boldsymbol{\kappa}\,. \tag{1.2.9}$$

Consequently, the current configuration version of the magnetic constitutive relation (1.2.6) gives

$$\boldsymbol{h} = \begin{cases} \rho_0 \dfrac{\partial \psi}{\partial \boldsymbol{B}}\cdot\boldsymbol{F}^{-1} + \dfrac{\boldsymbol{b}}{\mu_0}\,; & \forall\, \boldsymbol{x} \in \omega\,, \\[2ex] \dfrac{\boldsymbol{b}}{\mu_0}\,; & \forall\, \boldsymbol{x} \in \mathbb{R}^3\backslash\omega\,, \end{cases} \tag{1.2.10}$$

and the current configuration version counterpart of (1.2.7) becomes

$$\boldsymbol{\nabla}\times\boldsymbol{h} = \boldsymbol{j}\,; \quad \forall \boldsymbol{x} \in \mathbb{R}^3\,, \qquad \boldsymbol{n}\times[\![\boldsymbol{h}]\!] = \boldsymbol{\kappa}\,; \quad \forall \boldsymbol{x} \in \partial\omega\,. \tag{1.2.11}$$

while the current configuration version counterpart of (1.2.8) is

$$\boldsymbol{\nabla}\cdot\boldsymbol{b} = \boldsymbol{0}\,; \quad \forall \boldsymbol{x} \in \mathbb{R}^3\,, \qquad \boldsymbol{n}\cdot[\![\boldsymbol{b}]\!] = \boldsymbol{0}\,; \quad \forall \boldsymbol{x} \in \partial\omega\,, \qquad (\boldsymbol{b} = \boldsymbol{\nabla}\times\boldsymbol{a})\,, \tag{1.2.12}$$

where ω is the current configuration domain of the conductor, $\partial\omega$ its boundary and $\boldsymbol{n}$ its outward normal.

To equations (1.2.10) to (1.2.12) governing the magnetic response of a conductor, we must add the constitutive relation for the magnetic field $\boldsymbol{m}$ which is defined in the reference configuration and follows from (1.2.10)

$$\boldsymbol{b} = \mu_0(\boldsymbol{h}+\boldsymbol{m})\,; \quad \forall\, \boldsymbol{x} \in \mathbb{R}^3\,, \quad \boldsymbol{m} = -\rho_0 \frac{\partial \psi}{\partial \boldsymbol{B}}\cdot\boldsymbol{F}^{-1}\,; \quad \forall\, \boldsymbol{x} \in \omega\,, \quad \boldsymbol{m} = \boldsymbol{0}\,; \quad \forall\, \boldsymbol{x} \in \mathbb{R}^3\backslash\omega\,. \tag{1.2.13}$$

Mechanics Equations: Variations with Respect to Displacement $\boldsymbol{u}$

Lagrangian version

Once again, from Hamilton's principle (1.2.3), setting to zero the variation of $\mathscr{F}$ with respect to $\boldsymbol{u}$ gives

$$\begin{aligned} \mathscr{F}_{,\boldsymbol{u}}[\delta\boldsymbol{u}] = \int_{t_1}^{t_2} \Bigg\{ \int_{\mathbb{R}^3} \Bigg[\left(\frac{1}{\mu_0 J}\left(\frac{1}{2}(\boldsymbol{B}\cdot\boldsymbol{C}\cdot\boldsymbol{B})\boldsymbol{I} - \boldsymbol{B}(\boldsymbol{C}\cdot\boldsymbol{B})\right)\cdot\boldsymbol{F}^{-1} - \rho_0 \left(\frac{\partial \psi}{\partial \boldsymbol{C}}\right)\cdot\boldsymbol{F}^{T}\right) : (\boldsymbol{\nabla}\delta\boldsymbol{u}) \\ + \rho_0 \dot{\boldsymbol{u}}\cdot\frac{\mathrm{d}}{\mathrm{d}t}(\delta\boldsymbol{u}) + \rho_0 \boldsymbol{f}\cdot\delta\boldsymbol{u} \Bigg]\, \mathrm{d}V + \int_{\partial\Omega} [\boldsymbol{T}\cdot\delta\boldsymbol{u}]\, \mathrm{d}S \Bigg\}\, \mathrm{d}t = 0\,. \end{aligned} \tag{1.2.14}$$

As before, the domain $\mathbb{R}^3$ is separated into the volume Ω occupied by the body and the surrounding space $\mathbb{R}^3\backslash\Omega$. Taking into account the discontinuity of ρ_0 across $\partial\Omega$, integration by parts of (1.2.14) in the space and the time domains (recalling also the end conditions at t_1, t_2 in (1.2.3)) yields

$$\mathscr{F}_{,\boldsymbol{u}}[\delta\boldsymbol{u}] = \int_{t_1}^{t_2} \left\{ \int_{\mathbb{R}^3} \left[\left(\boldsymbol{\nabla}\cdot\boldsymbol{\Pi} - \rho_0\ddot{\boldsymbol{u}} + \rho_0\boldsymbol{f}\right)\cdot\delta\boldsymbol{u} \right] \mathrm{d}V + \int_{\partial\Omega} \left[\left(\boldsymbol{T} - \boldsymbol{N}\cdot[\![\boldsymbol{\Pi}]\!]\right)\cdot\delta\boldsymbol{u} \right] \mathrm{d}S \right\} \mathrm{d}t = 0 \,, \tag{1.2.15}$$

where $\boldsymbol{\Pi}$ is the "*total first Piola-Kirchhoff*" stress tensor (see Hanappier (2021))

$$\boldsymbol{\Pi} \equiv -\left(\frac{\partial\mathscr{E}}{\partial\boldsymbol{F}}\right)^T = \begin{cases} \rho_0 \left(\dfrac{\partial\psi}{\partial\boldsymbol{C}}\right)\cdot\boldsymbol{F}^T + \dfrac{1}{\mu_0 J}\boldsymbol{B}(\boldsymbol{F}\cdot\boldsymbol{B}) - \dfrac{1}{2\mu_0 J}(\boldsymbol{B}\cdot\boldsymbol{C}\cdot\boldsymbol{B})\boldsymbol{F}^{-1} \,; & \forall\, \boldsymbol{X}\in\Omega \,, \\ \dfrac{1}{\mu_0 J}\boldsymbol{B}(\boldsymbol{F}\cdot\boldsymbol{B}) - \dfrac{1}{2\mu_0 J}(\boldsymbol{B}\cdot\boldsymbol{C}\cdot\boldsymbol{B})\boldsymbol{F}^{-1} \,; & \forall\, \boldsymbol{X}\in\mathbb{R}^3\backslash\Omega \,. \end{cases} \tag{1.2.16}$$

The arbitrariness of $\delta\boldsymbol{u}$, (1.2.16) yields the following differential equation and boundary/interface condition

$$\boldsymbol{\nabla}\cdot\boldsymbol{\Pi} + \rho_0\boldsymbol{f} = \rho_0\ddot{\boldsymbol{u}} \,; \quad \forall\boldsymbol{X}\in\mathbb{R}^3 \,, \qquad \boldsymbol{N}\cdot[\![\boldsymbol{\Pi}]\!] = \boldsymbol{T} \,; \quad \forall\boldsymbol{X}\in\partial\Omega \,, \tag{1.2.17}$$

where one recognizes the reference configuration linear momentum balance of continuum mechanics.

Eulerian version

We complete (1.2.9) by recording the relation between the total stress measure of the reference configuration, the first Piola-Kirchhoff stress $\boldsymbol{\Pi}$ to the Cauchy stress tensor $\boldsymbol{\sigma}$, its current configuration counterpart as well as the reference mechanical (pseudo-)traction vector $\boldsymbol{T}$ and the current mechanical traction vector $\boldsymbol{t}$

$$\boldsymbol{\Pi} = J\boldsymbol{F}^{-1}\cdot\boldsymbol{\sigma} \,, \quad \boldsymbol{T}\mathrm{d}S = \boldsymbol{t}\mathrm{d}s \,, \quad (\boldsymbol{n}\mathrm{d}s = J\boldsymbol{N}\cdot\boldsymbol{F}^{-1}\mathrm{d}S) \,. \tag{1.2.18}$$

Consequently, the current configuration version of the mechanical constitutive relation (1.2.16) gives

$$\boldsymbol{\sigma} = \begin{cases} 2\rho\boldsymbol{F}\cdot\dfrac{\partial\psi}{\partial\boldsymbol{C}}\cdot\boldsymbol{F}^T + \dfrac{1}{\mu_0}\left[\boldsymbol{b}\boldsymbol{b} - \dfrac{1}{2}(\boldsymbol{b}\cdot\boldsymbol{b})\boldsymbol{I}\right] \,; & \forall\,\boldsymbol{x}\in\omega \,, \\ \dfrac{1}{\mu_0}\left[\boldsymbol{b}\boldsymbol{b} - \dfrac{1}{2}(\boldsymbol{b}\cdot\boldsymbol{b})\boldsymbol{I}\right] \,; & \forall\,\boldsymbol{x}\in\mathbb{R}^3\backslash\omega \,. \end{cases} \tag{1.2.19}$$

The current configuration equilibrium equation and boundary/interface condition counterpart of (1.2.17) is

$$\boldsymbol{\nabla}\cdot\boldsymbol{\sigma} + \rho\boldsymbol{f} = \rho\ddot{\boldsymbol{u}} \,; \quad \forall\boldsymbol{x}\in\mathbb{R}^3 \,, \qquad \boldsymbol{n}\cdot\boldsymbol{\sigma} = \boldsymbol{t} \,; \quad \forall\boldsymbol{x}\in\partial\omega \,. \tag{1.2.20}$$

1.2.2 Constitutive Choices

For isotropic materials in 3D, the most general form of their specific free energy can be expressed as a function of six invariants, three purely mechanical I_1, I_2, I_3 and three magneto-mechanical J_1, J_2, J_3. Since we are interested in 2D problems, we only need four invariants for the free energy, namely

$$\begin{aligned} &\psi(\boldsymbol{C}, \boldsymbol{B}) = \psi(I_1, I_2, J_1, J_2) \ ; \\ &I_1 \equiv \mathrm{tr}(\boldsymbol{C}) \ , \ I_2 \equiv \det(\boldsymbol{C}) = J^2 \ , \ J_1 \equiv \boldsymbol{B}\cdot\boldsymbol{B} \ , \ J_2 \equiv \boldsymbol{B}\cdot\boldsymbol{C}\cdot\boldsymbol{B} \ . \end{aligned} \tag{1.2.21}$$

The specific free energy, or equivalently the reference energy density $W(\boldsymbol{C}, \boldsymbol{B})$, is decomposed into a purely mechanical part and a magneto-mechanical part (see Hanappier et al. (2021)),

$$\begin{aligned} &\psi(\boldsymbol{C}, \boldsymbol{B}) = \psi_{mech}(\boldsymbol{C}) + \psi_{mag}(\boldsymbol{C}, \boldsymbol{B}) \ ; \\ &\rho_0\psi(\boldsymbol{C}, \boldsymbol{B}) \equiv W(\boldsymbol{C}, \boldsymbol{B}) = W_{mech}(\boldsymbol{C}) + W_{mag}(\boldsymbol{C}, \boldsymbol{B}) \ . \end{aligned} \tag{1.2.22}$$

Mechanical energy density

For the mechanical reference energy density $W_{mech}(\boldsymbol{C})$, a neo-Hookean behavior is chosen,

$$W_{mech}(I_1, I_2) = G\left[\frac{1}{2}(I_1 - 2 - \ln I_2) + \frac{\nu}{1-2\nu}(\sqrt{I_2} - 1)^2\right] \ , \tag{1.2.23}$$

where ν denotes the 3D Poisson ratio[7] ($-1 < \nu < 0.5$) and G the shear modulus. More refined choices may be relevant for modeling metals (e.g. see Thomas and Triantafyllidis (2009)) but the neo-Hookean model is perfectly adequate here, given the small strains expected (see Hanappier et al. (2022)).

Magnetic energy density

The magnetization law for ferromagnetic conductors is an old and well-researched topic that depends on many external factors: dissipation (e.g. see Perevertov (2017)), anisotropy (e.g. see Lopez et al. (2009)), residual stresses (e.g. see Baudouin et al. (2002)), multi axial loading (e.g. see Daniel and Hubert (2009); Pearson et al. (2000)), rate and inertia effects (e.g. see Bao et al. (2017)) to name but a few. As explained in the introduction, and given that the magnetization response of the conductor is not the primary focus of this study, we use a simple model proposed by Danas (2017).

The magnetic reference energy density W_{mag} used subsequently in the calculations assumes an non-hysteretic magnetic behavior (no dissipative phenomena considered). For small strains and an isotropic energy density W_{mag} depends, at first approximation, solely on the magnitude of the magnetic field. An appropriate choice

[7] A more appropriate expression should involve the 2D Poisson ratio $\nu' \equiv \nu/(1-\nu)$ in which case the coefficient of the volumetric part should read $\nu'/(1-\nu')$.

(see Hanappier et al. (2022)) is $W_{mag}(\boldsymbol{C},\boldsymbol{B}) = W_{mag}(I_2,J_2) = W_{mag}(\|\boldsymbol{b}\|)$, since from (1.2.9) $\boldsymbol{b}\cdot\boldsymbol{b} = \|\boldsymbol{b}\|^2 = J_2/I_2$.

For small magnetic fields the model must capture the linear magnetization behavior of the material, i.e. predict its initial magnetic susceptibility χ_0[8]. The model should also account for saturation, i.e. asymptotically approach the saturation magnetization m_s at large h-fields. To this effect, the following simple saturation magnetization law is used (see Danas (2017))

$$W_{mag}(\|\boldsymbol{b}\|) = \frac{\mu_0 m_s^2}{\chi_0}\ln\left[\cosh\left(\frac{\chi_0\|\boldsymbol{b}\|}{\mu_0 m_s}\right)\right] . \tag{1.2.24}$$

For small strains i.e. when $\|\boldsymbol{\epsilon}\| \ll 1$, where $\boldsymbol{\epsilon} \equiv (1/2)(\boldsymbol{\nabla u} + \boldsymbol{u\nabla})$, but arbitrary magnetic field amplitudes $\|\boldsymbol{b}\|$ and recalling that $\boldsymbol{C} = \boldsymbol{I}+2\boldsymbol{\epsilon}+O\|\boldsymbol{\epsilon}\|^2$, the expressions for the magnetization $\boldsymbol{m}$ and the total stress $\boldsymbol{\sigma}$ simplify considerably. It has been shown by Hanappier et al. (2021), using asymptotic expansions in (1.2.13), (1.2.19) and (1.2.21), that for the energy densities adopted in (1.2.22), (1.2.23) and (1.2.24), the total stress $\boldsymbol{\sigma}$ can be approximated by the sum of a purely elastic part $\overset{e}{\boldsymbol{\sigma}}(\boldsymbol{\epsilon})$ and a purely magnetic part $\overset{m}{\boldsymbol{\sigma}}(\boldsymbol{b})$

$$\boldsymbol{m} = \begin{cases} -\dfrac{\partial W_{mag}(\|\boldsymbol{b}\|)}{\partial \boldsymbol{b}} = \dfrac{\chi(\|\boldsymbol{b}\|)}{\mu_0[1+\chi(\|\boldsymbol{b}\|)]}\boldsymbol{b} \ ; & \forall\, \boldsymbol{x}\in\omega \ , \\ \boldsymbol{0} \ ; & \forall\, \boldsymbol{x}\in\mathbb{R}^3\backslash\omega \ , \end{cases}$$

$$\boldsymbol{\sigma} = \overset{e}{\boldsymbol{\sigma}} + \overset{m}{\boldsymbol{\sigma}} \ ; \quad \forall\, \boldsymbol{x}\in\mathbb{R}^3 \ ,$$

$$\overset{e}{\boldsymbol{\sigma}} = \begin{cases} \lambda \mathrm{tr}(\boldsymbol{\epsilon})\boldsymbol{I} + 2G\boldsymbol{\epsilon} \ ; & \forall\, \boldsymbol{x}\in\omega \ , \\ \boldsymbol{0} \ ; & \forall\, \boldsymbol{x}\in\mathbb{R}^3\backslash\omega \ . \end{cases} \tag{1.2.25}$$

$$\overset{m}{\boldsymbol{\sigma}} = \begin{cases} \dfrac{1}{\mu_0}[\boldsymbol{bb} - \dfrac{1}{2}(\boldsymbol{b}\cdot\boldsymbol{b})\boldsymbol{I}] - \dfrac{\chi(\|\boldsymbol{b}\|)}{\mu_0[1+\chi(\|\boldsymbol{b}\|)]}\left[\boldsymbol{bb} - (\boldsymbol{b}\cdot\boldsymbol{b})\boldsymbol{I}\right] \ ; & \forall\, \boldsymbol{x}\in\omega \ , \\ \dfrac{1}{\mu_0}[\boldsymbol{bb} - \dfrac{1}{2}(\boldsymbol{b}\cdot\boldsymbol{b})\boldsymbol{I}] \ ; & \forall\, \boldsymbol{x}\in\mathbb{R}^3\backslash\omega \ . \end{cases}$$

where $\chi(\|\boldsymbol{b}\|)$ is the material's "*magnetic susceptibility*"[9] since $\boldsymbol{m} = \chi(\|\boldsymbol{b}\|)\boldsymbol{h}$. The initial magnetic susceptibility introduced in (1.2.24) is $\chi_0 = \chi(0)$.

[8] It has been shown in Hanappier et al. (2021) that for small strains and magnetic fields the magnetic response is consistently characterized by two constants: magnetic susceptibility χ - considered here - and magnetostriction Λ - set to zero by selection of the energy density in (1.2.24).

[9] We note here that for a more general magnetic energy density W_{mag} the linearization procedure would have added an additional term to $\overset{m}{\boldsymbol{\sigma}}$ in (1.2.25) $\Lambda(\|\boldsymbol{b}\|)/[\mu_0(1+\chi(\|\boldsymbol{b}\|))]\boldsymbol{bb}$ where $\Lambda(\|\boldsymbol{b}\|)$ a *magneto mechanical coupling* coefficient which gives the curvature of the strain vs magnetic field in a stress-free uniaxial magnetostriction experiment.

Based on (1.2.24), one obtains from (1.2.25) the following magnetization as a function of the applied h-field, depicted in Figure 1.2 in dimensionless form where the reference magnetization has the saturation value $m_{ref} = m_s$ and the reference h-field is taken to be $h_{ref} = m_s/\chi_0$. It is also useful to establish a range where the linear magnetic response is a reasonable approximation; to this effect we set $h_l = 0.6\times10^{-2}h_{ref}$ as the limit for the linear range for the magnetic response $0 \leq h \leq h_l$, as seen in Figure 1.2a.

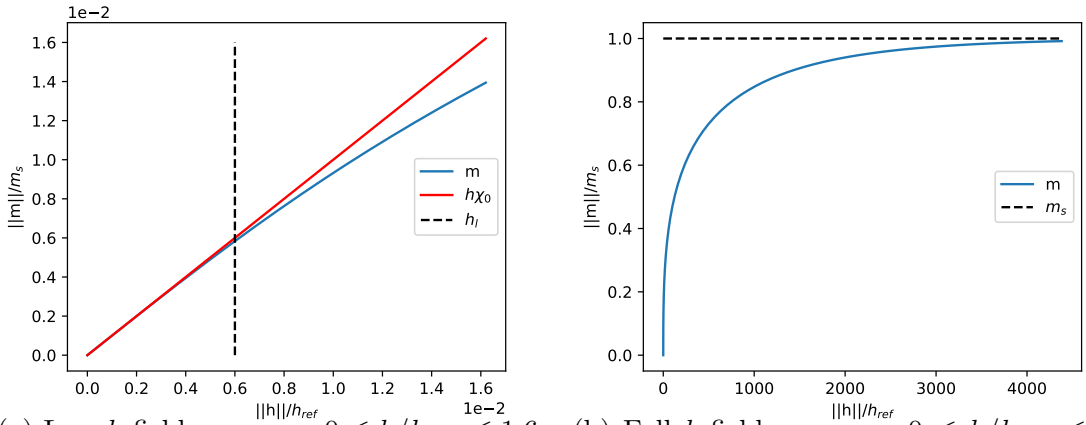

(a) Low h-field response: $0 \leq h/h_{ref} \leq 1.6\times 10^{-2}$.

(b) Full h-field response: $0 \leq h/h_{ref} \leq 5\times 10^{3}$.

Figure 1.2: Non linear magnetization law in dimensionless form: magnetization as a function of applied h-field.

As seen from (1.2.25) for small strains, the determination of the magnetic stresses $\overset{\boldsymbol{m}}{\boldsymbol{\sigma}}$ depends solely on the magnetic field $\boldsymbol{b}$ which in turn requires only finding the magnetic potential $\boldsymbol{a}$ by solving the Eulerian version of the magnetics equations (1.2.10) to (1.2.13) in conjunction to (1.2.24) and $(1.2.25)_1$. The determination of the elastic stresses $\overset{\boldsymbol{e}}{\boldsymbol{\sigma}}$ in $(1.2.25)_3$ requires the determination of the displacement $\boldsymbol{u}$ which can be found by solving the Eulerian version of the mechanics equations (1.2.20) in conjunction with (1.2.25). Since only the total forces exerted on the conductors are of interest, the determination of the displacement field is not necessary, as will be discussed in Section 1.2.4.

1.2.3 Analytical Solution for a Single Conductor with Linear Magnetic Response

Assume a circular section conductor of radius R subjected to a current of uniform density j along the cylinder's axis ($\boldsymbol{j} = j\boldsymbol{e}_z$) and a remote h-field of magnitude h_0 along the y direction ($\boldsymbol{h}_0 = h_0\boldsymbol{e}_y$) as shown in Figure 1.3. Of interest are the

resulting h-field $\boldsymbol{h}$, magnetization $\boldsymbol{m}$ and magnetic stress $\overset{m}{\boldsymbol{\sigma}}$, which for the case of a linear magnetic constitutive law can be calculated analytically.

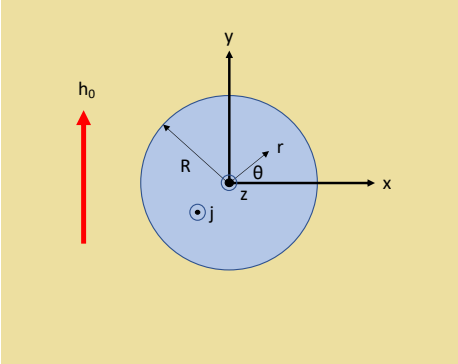

Figure 1.3: Cross section of a cylindrical conductor of radius R subjected to a current of uniform density $\boldsymbol{j} = j\boldsymbol{e}_z$ and a remote h-field of magnitude $\boldsymbol{h}_0 = h_0\boldsymbol{e}_y$.

By superposing the solutions for the remote h-field h_0 and the uniform current density j, one can verify that the solution of Ampère's equation in (1.2.11) is

$$
\begin{aligned}
r > R \ : \quad & \begin{cases} h_x = \left(\dfrac{R}{r}\right)^2 \left[(h_0 - h_{in})\sin(2\theta) - \dfrac{jr}{2}\sin\theta\right] , \\[2ex] h_y = h_0 + \left(\dfrac{R}{r}\right)^2 \left[(h_{in} - h_0)\cos(2\theta) + \dfrac{jr}{2}\cos\theta\right] , \end{cases} \\
0 \le r \le R \ : \quad & \begin{cases} h_x = -\dfrac{jr}{2}\sin\theta , \\[2ex] h_y = h_{in} + \dfrac{jr}{2}\cos\theta . \end{cases}
\end{aligned}
\tag{1.2.26}
$$

For the case of a linear, isotropic magnetic response, i.e. $\boldsymbol{m} = \chi_0\boldsymbol{h}$ and recalling that inside the conductor $\boldsymbol{b} = \mu_0(\boldsymbol{h} + \boldsymbol{m})$ and outside $\boldsymbol{b} = \mu_0\boldsymbol{h}$ one obtains by using the boundary condition for the magnetic field $\boldsymbol{b}$

$$
h_{in} = \frac{2(1+\chi_0)}{2+\chi_0}h_0 \ ; \quad 0 \le r \le R \ : \begin{cases} m_x = -\chi_0\dfrac{jr}{2}\sin\theta , \\[2ex] m_y = \chi_0\left[\dfrac{2}{2+\chi_0}h_0 + \dfrac{jr}{2}\cos\theta\right] . \end{cases}
\tag{1.2.27}
$$

From (1.2.26) and (1.2.27), the magnetic field $\boldsymbol{b}$ is thus found to be

$$
\begin{aligned}
r > R \ : \ & \begin{cases} b_x = \mu_0 \left(\dfrac{R}{r}\right)^2 \left[\dfrac{\chi_0}{2+\chi_0} h_0 \sin(2\theta) - \dfrac{jr}{2}\sin\theta\right] \ , \\ \\ b_y = \mu_0 \left\{ h_0 - \left(\dfrac{R}{r}\right)^2 \left[\dfrac{\chi_0}{2+\chi_0} h_0 \cos(2\theta) - \dfrac{jr}{2}\cos\theta\right]\right\} \ , \end{cases} \\ \\
0 \le r \le R \ : \ & \begin{cases} b_x = -\mu_0(1+\chi_0)\dfrac{jr}{2}\sin\theta \ , \\ \\ b_y = \mu_0(1+\chi_0)\left[\dfrac{2}{2+\chi_0} h_0 + \dfrac{jr}{2}\cos\theta\right] \ . \end{cases}
\end{aligned}
\tag{1.2.28}
$$

The above solution is valid as long as the linear magnetic constitutive response is a reasonable approximation, i.e. $\|\boldsymbol{b}\|_{max} \le b_l$, where $b_l = \mu_0 h_l$ (see Figure 1.2a). A straightforward calculation of the magnetic field norm $\|\boldsymbol{b}\| = (b_x^2 + b_y^2)^{1/2}$ gives from (1.2.28) that the maximum occurs at the boundary $(r, \theta) = (R, 0)$

$$
\|\boldsymbol{b}\|_{max} = \mu_0(1+\chi_0)\left[\frac{2}{2+\chi_0} h_0 + \frac{jR}{2}\right] = b_l \ , \tag{1.2.29}
$$

thus establishing the maximum value combination of the remote h-field and current density for a near-linear magnetic response.

Having obtained the magnetic field $\boldsymbol{b}$ inside and outside the conductor, we can calculate the magnetic stress $\overset{m}{\boldsymbol{\sigma}}$, both inside and outside the conductor from (1.2.25).

1.2.4 Calculating Forces on Conductors Using Contour Integrals

Single conductor

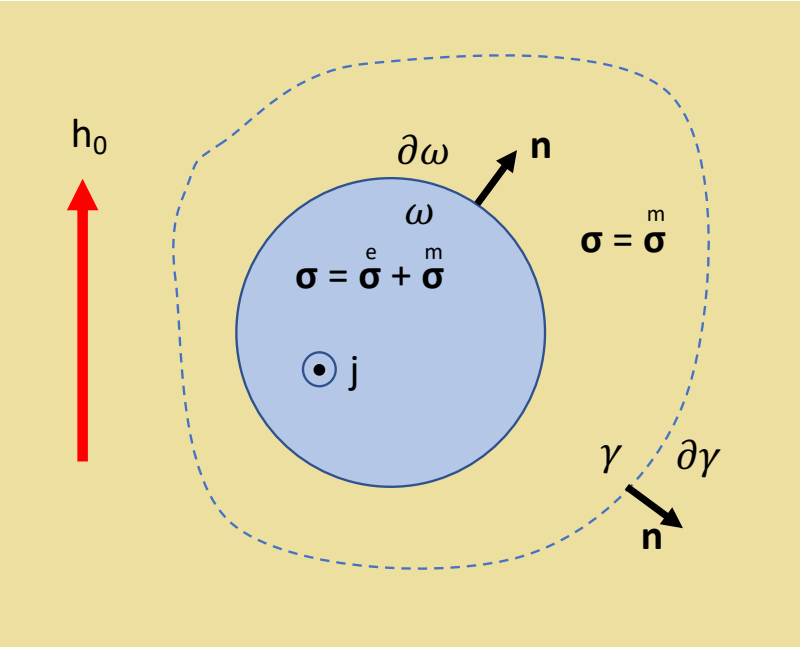

Figure 1.4: Calculating the Lorentz forces $\boldsymbol{F}_{L}$ on a conductor subjected to a current of density j and a remote h-field of magnitude h_0 using contour integrals.

We start by defining the total force per unit length $\boldsymbol{F}_{L}$ on a conductor occupying domain ω with boundary $\partial\omega$ subjected to a current of density j and a remote h-field $\boldsymbol{h}_0$ as shown in Figure 1.4.

Since the traction exerted by the magnetic field on the conductor is $\boldsymbol{n}\cdot\boldsymbol{\sigma}$ the force is

$$\boldsymbol{F}_{L} \equiv \int_{\partial\omega} \mathbf{n}\cdot\boldsymbol{\sigma}\, \mathrm{d}l \,. \tag{1.2.30}$$

Using Gauss' divergence theorem in the domain $\gamma\backslash\omega$ and recalling that the total stress there is the magnetic stress (i.e. $\boldsymbol{\sigma} = \overset{m}{\boldsymbol{\sigma}}$) and recalling the equilibrium equation (1.2.20) for that domain $\boldsymbol{\nabla}\cdot\overset{m}{\boldsymbol{\sigma}} = \mathbf{0}$ since the material density in vacuum (the domain $\gamma\backslash\omega$) is $\rho = 0$

$$\begin{aligned} &\int_{\partial(\gamma\backslash\omega)} \mathbf{n}\cdot\boldsymbol{\sigma}\, \mathrm{d}l = \int_{\gamma\backslash\omega} \boldsymbol{\nabla}\cdot\boldsymbol{\sigma}\, \mathrm{d}s = \int_{\gamma\backslash\omega} \boldsymbol{\nabla}\cdot\overset{m}{\boldsymbol{\sigma}}\, \mathrm{d}s = 0 \\ \Longrightarrow \quad &\int_{\partial\gamma} \mathbf{n}\cdot\boldsymbol{\sigma}\, \mathrm{d}l = \int_{\partial\omega} \mathbf{n}\cdot\boldsymbol{\sigma}\, \mathrm{d}l = \boldsymbol{F}_{L} \,, \end{aligned} \tag{1.2.31}$$

where γ is an arbitrary domain completely surrounding ω, i.e. $\gamma \supset \omega$ as seen in Figure 1.4.

Taking the contour $\partial\gamma$ as far as possible from $\partial\omega$, one can consider a circle of radius $r \gg R$ in which case the dominant terms in the remote h-field $\boldsymbol{h}^{\infty}$ and the

remote total stress $\boldsymbol{\sigma}^\infty$ yield[10] from $(1.2.26)_1$ and (1.2.25) respectively the following expressions

$$\boldsymbol{h}^\infty = -\frac{I\sin\theta}{2\pi r}\boldsymbol{e}_x + \left[h_0 + \frac{I\cos\theta}{2\pi r}\right]\boldsymbol{e}_y\ , \quad \boldsymbol{\sigma}^\infty = \mu_0\left[\boldsymbol{h}^\infty\boldsymbol{h}^\infty - \frac{1}{2}(\boldsymbol{h}^\infty\cdot\boldsymbol{h}^\infty)\boldsymbol{I}\right]\ . \tag{1.2.32}$$

From (1.2.30), the force/length $\boldsymbol{F}_{_L}$ exerted on the conductor, comes with no surprise to be the textbook result of electromagnetics for the force on a conductor carrying a current I and subjected to a remote magnetic field of strength b_0 normal to the conductor

$$\begin{aligned}\boldsymbol{F}_{_L} &= \int_{\partial\gamma} \mathbf{n}\cdot\boldsymbol{\sigma}^\infty \,\mathrm{d}l \\ &= \mu_0\int_0^{2\pi}(\boldsymbol{e}_x\cos\theta + \boldsymbol{e}_y\sin\theta)\cdot\left[\boldsymbol{h}^\infty\boldsymbol{h}^\infty - \frac{1}{2}(\boldsymbol{h}^\infty\cdot\boldsymbol{h}^\infty)\boldsymbol{I}\right] r\mathrm{d}r\mathrm{d}\theta = -b_0 I\boldsymbol{e}_x\ .\end{aligned} \tag{1.2.33}$$

It is important to note that the above result is independent of the cross section of the conductor as well as of its magnetic properties, since the method of calculating the Lorentz force $\boldsymbol{F}_{_L}$ is based on the Maxwell stresses $\boldsymbol{\sigma}^\infty$ generated by the remote magnetic field $\boldsymbol{b}_0$ and the current I.

Two parallel conductors

The Lorentz force on each of the two conductors of radius R separated by a distance D is calculated from the contour integrals on the two corresponding domains $\gamma_1 \supset \omega_1$ and $\gamma_2 \supset \omega_2$ as shown in Figure 1.5. Each domain consists of half a disc of radius $r > D$ and $\gamma_1 \cap \gamma_2$ is the $[-r, r]$ interval of the y-axis.

[10] The magnetic field for $r \gg R$ is independent of the magnetic properties of the conductor and depends solely on the total current $I = \pi R^2$, thus justifying using the linear result in (1.2.26) to find the dominant terms.

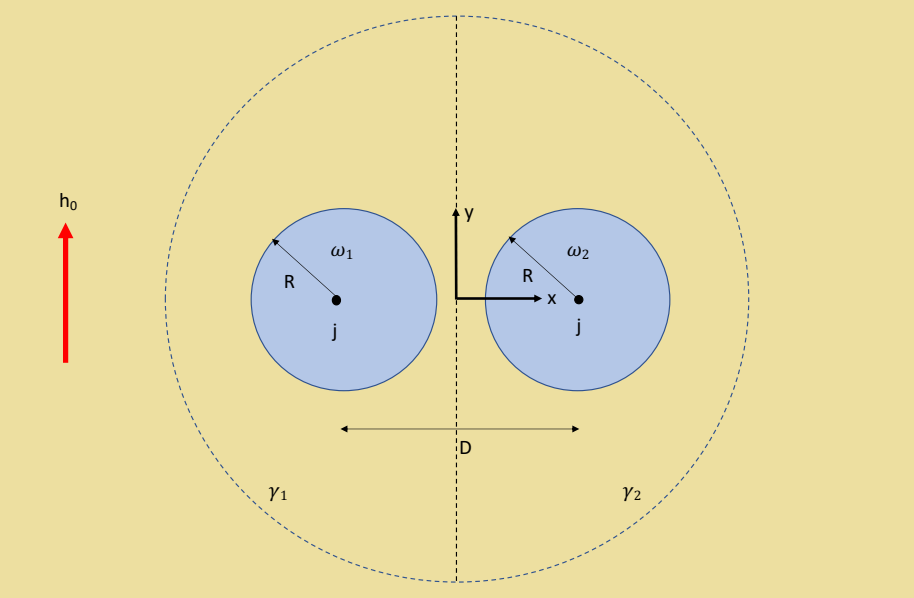

Figure 1.5: Calculating the Lorentz forces on two parallel conductors subjected to same or opposite direction currents of density j and a remote h-field of magnitude h_0 using contour integrals.

The h-field for $r \gg D$ in the case of currents of same $\boldsymbol{h}_S^\infty$ or opposite $\boldsymbol{h}_O^\infty$ direction, is given by

$$\boldsymbol{h}_S^\infty = -\frac{2I\sin\theta}{2\pi r}\boldsymbol{e}_x + \left[h_0 + \frac{2I\cos\theta}{2\pi r}\right]\boldsymbol{e}_y\ , \quad \boldsymbol{h}_O^\infty = h_0\boldsymbol{e}_y\ , \tag{1.2.34}$$

since in the first case (same direction currents designated by S) the influence of the electric currents on the magnetic field is additive and in the latter case (opposite direction currents designated by O) they cancel each other. The Maxwell stress $\boldsymbol{\sigma}^\infty$ at $r \gg D$ is given in terms of $\boldsymbol{h}^\infty$ by (1.2.32).

Calculating the contour integrals on $\partial\gamma_1$ and $\partial\gamma_2$ in clockwise direction[11], we obtain for the corresponding Lorentz forces $\boldsymbol{F}_L^{1,2}$

$$\boldsymbol{F}_{L,S}^{1,2} = \left[-b_0 I \pm \frac{1}{2\mu_0}\int_{-\infty}^{+\infty}[b_x^2(0,y) - b_y^2(0,y) + b_0^2]\mathrm{d}y\right]\boldsymbol{e}_x\ ,$$

$$\boldsymbol{F}_{L,O}^{1,2} = \left[\pm\frac{1}{2\mu_0}\int_{-\infty}^{+\infty}[b_x^2(0,y) - b_y^2(0,y) + b_0^2]\mathrm{d}y\right]\boldsymbol{e}_x\ . \tag{1.2.35}$$

Unlike the single conductor, we do expect in the two conductors case that the magnetic properties of the conductors will influence the Lorentz forces due to the change of the magnetic field $\boldsymbol{b}$ along the y-axis, as seen from (1.2.35).

[11] Due to symmetry considerations one can show that the $\boldsymbol{e}_x$ component of the Lorentz forces is zero.

Infinite array of parallel conductors

We consider next an infinite array of parallel cylindrical conductors of radius R equally spaced from each other at a distance D and subjected to a remote h-field $\boldsymbol{h}_0$ as shown in Figure 1.6. The conductors are subjected to uniform current densities $\boldsymbol{j}$, either all in the same direction or in alternating opposite directions.

An immediate result of periodicity is that for $D \gg R$ the Lorentz force in each conductor is $F_{_L} = \pm b_0 I \boldsymbol{e}_x$ (where the current $I = j\pi R^2$ and the $\pm$ sign depends on the current direction of the conductor at hand) since the magnetic field contribution at the center of any given conductor due to a conductor at distance $+nD$ is cancelled by its counterpart at distance $-nD$, where $n \in \mathbb{N}$, thus leaving the magnetic field there equal to the remote magnetic field $\boldsymbol{b}_0$.

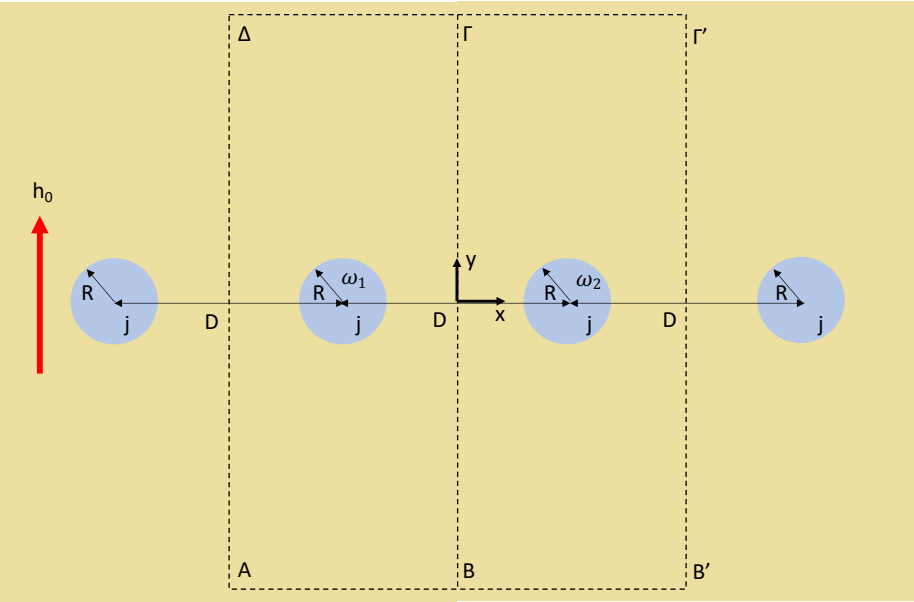

Figure 1.6: Calculating the Lorentz forces on parallel conductors subjected to same or alternating direction currents of density j and a remote h-field of magnitude h_0 in an infinite array using contour integrals.

A more refined result is obtained in the case of the periodic array with same direction currents. The Lorentz force on each conductor can be calculated from the contour integral along $AB\Gamma\Delta$ as seen in Figure 1.6,

$$F_{_L} = \int_A^B [-\mathbf{e}_y \cdot \boldsymbol{\sigma}^\infty]\, \mathrm{d}x + \int_B^\Gamma [\mathbf{e}_x \cdot \boldsymbol{\sigma}]\, \mathrm{d}y + \int_\Gamma^\Delta [\mathbf{e}_y \cdot \boldsymbol{\sigma}^\infty]\, \mathrm{d}x + \int_\Delta^A [-\mathbf{e}_x \cdot \boldsymbol{\sigma}]\, \mathrm{d}y \quad (1.2.36)$$

From periodicity the stress $\boldsymbol{\sigma}$ is the same on the $B\Gamma$ and $A\Delta$ segments of the contour but given the opposite direction of the normal there ($\boldsymbol{n} = \pm \mathbf{e}_x$) the sum of these

two integrals vanishes. For the h-field[12]on segments AB and $\Gamma\Delta$ as well as the stress there (recall (1.2.32)) we have

$$\boldsymbol{h}^{\infty} = \pm\frac{I}{2}\mathbf{e}_x + h_0\mathbf{e}_y \ , \quad \boldsymbol{\sigma}^{\infty} = \mu_0\left[\boldsymbol{h}^{\infty}\boldsymbol{h}^{\infty} - \frac{1}{2}(\boldsymbol{h}^{\infty}\cdot\boldsymbol{h}^{\infty})\boldsymbol{I}\right] \ , \tag{1.2.37}$$

and hence the nontrivial contribution from these segments to the Lorentz force gives $\boldsymbol{F}_{_L} = \pm b_0 I\mathbf{e}_x$ depending on the direction of the current I. It is interesting to note that the Lorentz force in an infinite, periodic array of conductors, all with currents in the same direction is independent of the conductors' magnetic properties, irrespectively of how close they are!

For the case of currents with alternating directions, a similar argument on the contour $AB\Gamma'\Delta'$ will give a zero total Lorentz force $\boldsymbol{F}_{_L} = \boldsymbol{F}^1_{_L} + \boldsymbol{F}^2_{_L} = 0$ since $\boldsymbol{h}^{\infty} = h_0\mathbf{e}_y$, where the superscripts refer to the *left* and *right* conductors in the $AB\Gamma'\Delta'$ contour. As previously discussed for $D \gg R$, $\boldsymbol{F}^1_{_L} = -\boldsymbol{F}^2_{_L} = \pm b_0 I\boldsymbol{e}_x$, but for closer spacing of the conductors, their magnetic properties will influence their Lorentz force.

1.3 Numerical (FEM) Implementation

We apply here the general theory developed in Section 1.2.1 and Section 1.2.2 to the boundary value problem of the ferromagnetic conductors subjected to a remote magnetic field and an electric current. The numerical solution is based on an FEM discretization of a 2D, quasistatic problem and solved by extremization of a simplified version of the Lagrangian (1.2.2) based on the energy density adopted in Section 1.2.2. Due to the small strains involved and the simplified expression for the total stress in (1.2.25), only the magnetic field $\mathbf{b}$ – and hence the magnetic potential a – needs to be calculated in order to determine the magnetic stress $\overset{m}{\boldsymbol{\sigma}}$ which is the basis for calculating the total force applied in each semiconductor, as discussed in Section 1.2.4. Had one been interested in calculating also the elastic stress $\overset{e}{\boldsymbol{\sigma}}$, the fully coupled problem would have to be solved to also determine the displacement field $\boldsymbol{u}$ (see Hanappier et al. (2022)).

Solution method is based on a 2D model (plane strain assumed, see Figure 1.1), where all field quantities are assumed independent of z. It involves no external body forces, no mechanical tractions nor current sheets and has negligible induced currents and acceleration terms, thus requiring only a spatial discretization of the corresponding quasistatic problem. Moreover, since we are not interested in calculating the displacement field $\boldsymbol{u}$, the current configuration (Eulerian) formulation of the problem is adopted with all field quantities functions of the current position vector $\boldsymbol{x}$.

[12]The $\pm$ sign corresponds to each different x-segment of the contour.

The Lagrangian of the system defined in (1.2.2) (kinetic minus potential energy: $\mathscr{L} = \mathscr{K} - \mathscr{P}$), in the absence of the kinetic energy ($\mathscr{K} = 0$) equals minus the potential energy ($\mathscr{L} = -\mathscr{P}$), which for the case of no external body forces no mechanical surface tractions nor current sheets becomes

$$\mathscr{P} = \int_{\mathbb{R}^2} W(\|\boldsymbol{b}\|)\, \mathrm{d}s - \int_{\omega} (\boldsymbol{j}\cdot\boldsymbol{a})\, \mathrm{d}s\ ; \quad W(\|\boldsymbol{b}\|) \equiv W_{mag}(\|\boldsymbol{b}\|) + \frac{1}{2\mu_0}\|\boldsymbol{b}\|^2\ , \quad \boldsymbol{b} = \boldsymbol{\nabla}\times a\ , \tag{1.3.1}$$

where $W(\|\boldsymbol{b}\|)$ is the system's total energy density. The conductor's magnetic energy density in only defined in the domain ω, i.e. $W_{mag}(\|\boldsymbol{b}(\boldsymbol{x})\|) \neq 0\ ; \forall\ \boldsymbol{x} \in \omega$ and $W_{mag}(\|\boldsymbol{b}(\boldsymbol{x})\|) = 0\ ; \forall\ \boldsymbol{x} \in \mathbb{R}^2\backslash\omega$.

Since a plane strain boundary value problem is considered, integration over the entire domain involves $\mathbb{R}^2$ and the cross-section of the stator domain has boundary $\partial\omega$. Moreover, the in-plane magnetic field ($\boldsymbol{b} = \boldsymbol{\nabla}\times\boldsymbol{a}$, see (1.2.12)) is derived from the magnetic vector potential $\boldsymbol{a} = a(x,y)\boldsymbol{e}_z$, requiring only one scalar field variable for its determination i.e. $\boldsymbol{b} = a_{,y}\boldsymbol{e}_x - a_{,x}\boldsymbol{e}_y$. Consequently the Coulomb gauge condition $\boldsymbol{\nabla}\cdot\boldsymbol{a}$ (see footnote 4) is automatically satisfied. As a result of Ampère's law (1.2.11) and the in-plane h-field, the externally applied currents can only be of the form $\boldsymbol{j} = j_z(x,y)\boldsymbol{e}_z$, thus automatically satisfying charge conservation $\boldsymbol{\nabla}\cdot\boldsymbol{j} = 0$. Thus, the solution of the magnetic boundary value problem, based on the FEM discretization of (1.3.1) requires only one scalar field variable $a(x,y)$[13].

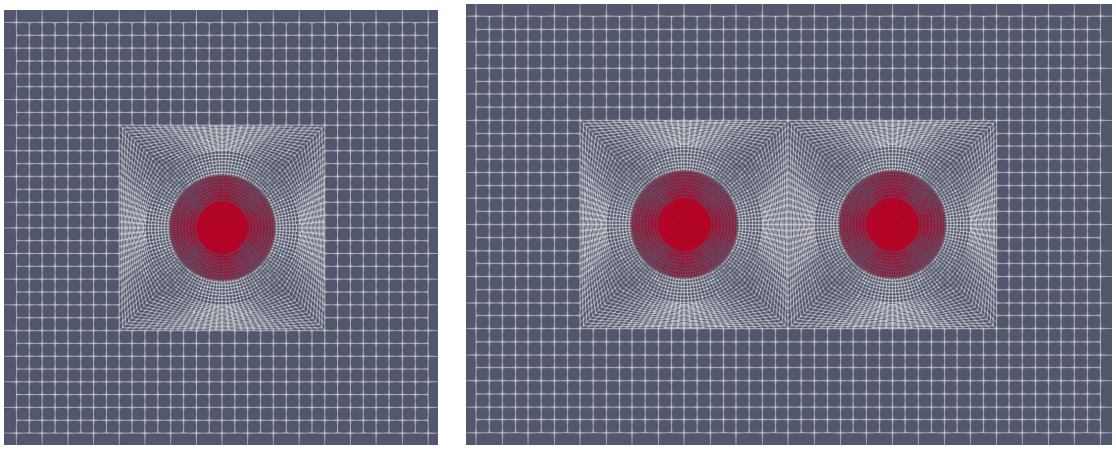

(a) Mesh for the magnetic potential a in ω and $\mathbb{R}\backslash\omega$.

(b) Mesh for the magnetic potential a in $\omega_1 \cup \omega_2$ and $\mathbb{R}\backslash(\omega_1 \cup \omega_2)$

Figure 1.7: Typical FEM meshes used for calculating the magnetic potential a inside and outside the conductor domain. In (a) for a single conductor of radius R and in (b) for two conductors of same radius R at a distance $D = 4R$.

[13]For added simplicity, the numerical code is based on the discretization of the perturbation field $\widehat{a}(x,y) \equiv a(x,y) - a_0(x,y)$ resulting from the presence of the conductor; in its absence $a(x,y) = a_0(x,y) = -xb_0$.

For the sake of simplicity and meshing flexibility, the elements chosen for the FEM spatial discretization are quadrilateral 2D elements with a second order polynomial interpolation and nine nodes, using a 3×3 Gauss numerical integration scheme. The corresponding UEL (user element) is provided to "*DealII*" in the final assembly of the global force vector and stiffness matrix of the problem. The accuracy of the numerical code is verified using the analytical solution for the single conductor with a linear magnetization law presented in Section 1.2.3. The boundary condition imposed on the computational domain is $\widehat{a}(x, y) = 0$. To ensure that this assumption does not affect the accuracy of the results, we use rectangular domains of minimum dimensions $120R \times 120R$, so that their boundaries are at least $60R$ away from the center of each conductor. Numerical simulations typically require $50,000$ d.o.f. meshes. Only the central section of the much larger computational domain is shown in Figure 1.7, to better depict the denser mesh inside and near the conductors.

1.4 Results

We start with a remark about the validity of the uniform current assumption that is typically adopted in the electrical engineering literature and hence in the ensuing numerical calculations. In order to satisfy the Maxwell-Gauss equations pertaining to the electric field resulting inside the conductor due to the electric current (in addition to the Maxwell-Ampère equations presented in Section 1.2), we make the simplifying assumption of a negligible conductor resistivity, resulting in a negligible electric field inside (and hence outside of) the conductor. In a simulation that accounts for ohmic dissipation in the conductor Hall effects Hall (1879) will have to be considered, resulting in non-uniform current densities inside a conductor.

In presenting the results we adopt a dimensionless form and hence we define the following reference quantities based on the conductor's material properties and geometry i.e. its radius R

$$\begin{aligned} &m_{ref} = m_s \ , \ b_{ref} = m_s \mu_0 \ , \ h_{ref} = \frac{m_s}{\chi_0} \ , \ j_{ref} = \frac{h_{ref}}{R} = \frac{m_s}{R\chi_0} \ , \\ &F_{ref} = b_{ref} j_{ref} \pi R^2 = \frac{m_s^2 \mu_0 \pi R}{\chi_0} \ . \end{aligned} \tag{1.4.1}$$

We have in mind a typical ferromagnetic wire of radius $1.5mm$ as the base case and hence all subsequent numerical calculations presented here use the values: $R = 1.5\times 10^{-3}\ m$, $\chi_0 = 2.5\times 10^3$, $m_s = 1.7\times 10^6\ Am^{-1}$ and $\mu_0 = 4\pi\times 10^{-7}\ NA^{-2}$. The reference values in the $MKSA$ system of units are: $h_{ref} = 0.68\ Am^{-1}$, $j_{ref} = 0.45\times 10^6\ Am^{-2}$ and $b_{ref} = 2.14\ T$.

A remark about the range of magnetic fields and electric currents used in the ensuing calculations is in order. As the most upscale laboratory magnets generate magnetic fields of the order of $1\ T$ to $2\ T$, we investigate magnetic fields up to

0.7 b_{ref}. To avoid excessive ohmic heating of the conductors and by assuming (to be on the conservative side) adiabatic heating, the current density is related to the temperature increase rate $\dot{\theta}$ (in $^{\circ}K\ sec^{-1}$) by

$$j = (\gamma \rho_0 c_p \dot{\theta})^{1/2} \approx 3.13 \times 10^6 (\dot{\theta})^{1/2}\ Am^{-2}\ , \tag{1.4.2}$$

where γ is the electric conductivity, c_p is the specific heat and ρ_0 is the mass density of the conductor and where we have also assumed typical values for a ferromagnetic material. We present calculations here for current densities up to 6.36 j_{ref}, which correspond to a temperature increase rate of about $0.83^{\circ}K\ sec^{-1}$.

1.4.1 Single Conductor Under Magnetic Field and Electric Current

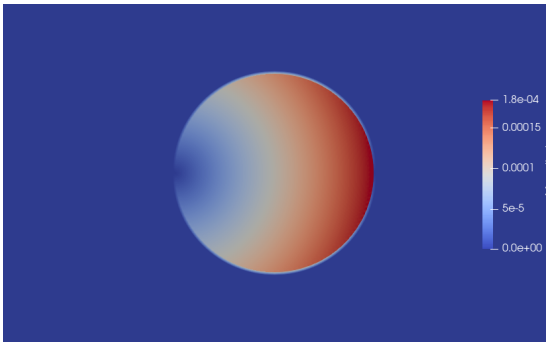

(a) $\|\boldsymbol{m}\|/m_s$ Near linear magnetic response.

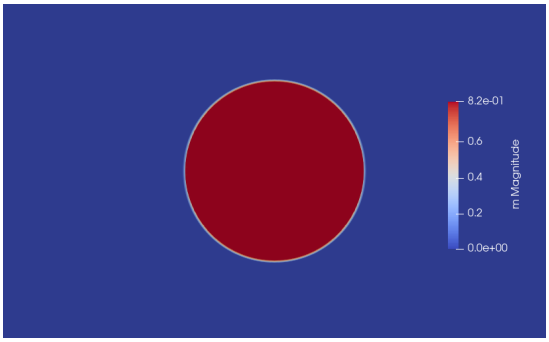

(b) $\|\boldsymbol{m}\|/m_s$ Near saturation magnetic response.

Figure 1.8: Contours of the magnetic field norm $\|\boldsymbol{m}\|/m_s$ for a conductor subjected to an electric current and a remote magnetic field. In (a) for low remote magnetic field $b_0 = 0.52 \times 10^{-4}\ b_{ref}$ and current $j = 2 \times 10^{-4}\ j_{ref}$ where the entire section is in the near-linear regime of magnetization. In (b) for high remote magnetic field $b_0 = 0.66\ b_{ref}$ and current $j = 5.25\ j_{ref}$, where the entire conductor is near the saturation regime of magnetization.

We start by presenting in Figure 1.8 the magnetic field for a single conductor with a circular section of radius R, subjected to a uniform current density $\boldsymbol{j} = j\boldsymbol{e}_z$ and a remote external magnetic field $\boldsymbol{b}_0 = b_0 \boldsymbol{e}_y$ (see geometry in Figure 1.3). More specifically, contours of the dimensionless magnetic field norm $\|\boldsymbol{m}\|/m_s$ are depicted in Figure 1.8a for near-linear magnetic response (low values of external magnetic field and current, respectively $b_0 = 0.52 \times 10^{-4}\ b_{ref}$ and $j = 2 \times 10^{-4}\ j_{ref}$) and in Figure 1.8b for near saturation magnetic response (high values of external magnetic field and current, respectively $b_0 = 0.66\ b_{ref}$ and $j = 5.25\ j_{ref}$).

For a rigid, isotropic ferromagnetic material of circular section in 2D or spherical shape in 3D subjected to an external magnetic field it is known (e.g. see Brown (1966)) that the h-field and hence the magnetization inside the conductor is uniform, independently of the magnetic constitutive law. It is the presence of the magnetic field gradient due to the applied current that introduces a gradient of the magnetization field inside the conductor, as seen for the special case of a linear magnetic response from (1.2.27).

For the near-linear magnetic regime, we observe in Figure 1.8a that the magnetization is minimized (near zero) at the left side, since the external and current-induced magnetic fields are in opposite directions in that location, and maximized on the right side when these same fields act in the same direction, as expected from (1.2.27). For the near saturation response we observe from Figure 1.8b that the entire domain has a nearly uniform magnetization of about $0.82m_s$) and the influence of the current on the magnetization is almost negligible. Numerical simulations with much higher currents $j \approx 10^2\ j_{ref}$ (not reported here) produce non-uniform magnetization fields with a strong gradient that increases with an increasing current.

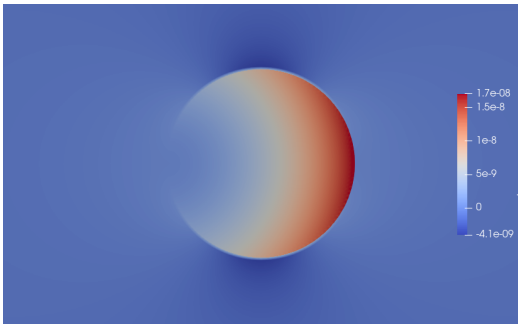

(a) $\overset{m}{\sigma}_{xx}/\mu_0 m_s^2$ Near linear response.

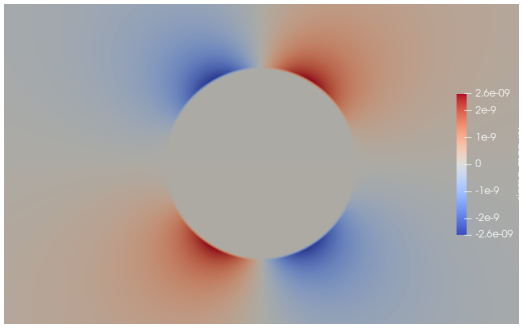

(b) $\overset{m}{\sigma}_{xy}/\mu_0 m_s^2$ Near linear response.

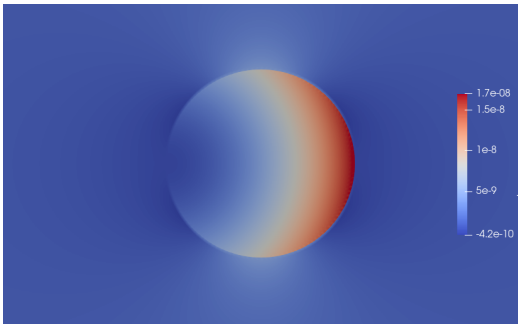

(c) $\overset{m}{\sigma}_{yy}/\mu_0 m_s^2$ Near linear response.

Figure 1.9: Contours for the dimensionless magnetic stress $\overset{m}{\boldsymbol{\sigma}}/\mu_0 m_s^2$ components for a conductor subjected to an electric current and a remote magnetic field. Low remote magnetic field $b_0 = 0.52 \times 10^{-4}\ b_{ref}$ and current $j = 2 \times 10^{-4}\ j_{ref}$ where the entire section is in the near-linear regime of magnetization.

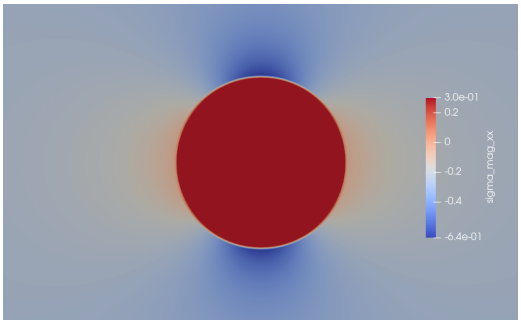

(a) $\overset{m}{\sigma}_{xx}/\mu_0 m_s^2$ Near saturation response.

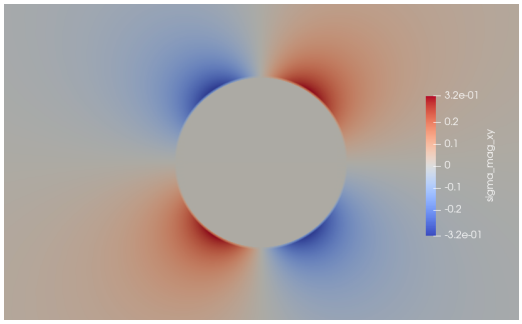

(b) $\overset{m}{\sigma}_{xy}/\mu_0 m_s^2$ Near saturation response.

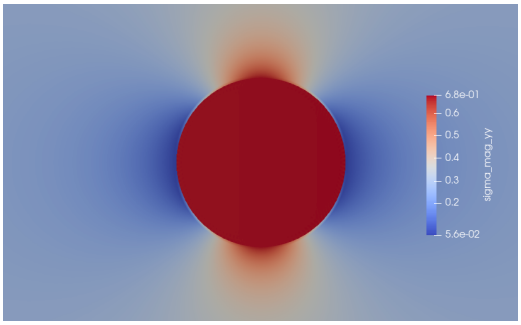

(c) $\overset{m}{\sigma}_{yy}/\mu_0 m_s^2$ Near saturation response.

Figure 1.10: Contours for the dimensionless magnetic stress $\overset{m}{\boldsymbol{\sigma}}/\mu_0 m_s^2$ components for a conductor subjected to an electric current and a remote magnetic field. For high remote magnetic field $b_0 = 0.66\ b_{ref}$ and current $j = 5.25\ j_{ref}$, where the entire conductor is near the saturation regime of magnetization.

Next we present the magnetic stress field components in Figure 1.9 for the same single conductor. More specifically, contours of the dimensionless magnetic stress field $\overset{m}{\boldsymbol{\sigma}}/\mu_0 m_s^2$ components are depicted in Figure 1.9a, Figure 1.9b, Figure 1.9c, for near-linear magnetic response (low values of external and current-induced h-fields, same as in Figure 1.8a) and in Figure 1.10a, Figure 1.10b, Figure 1.10c for near saturation magnetic response (high values of external and current-induced h-fields, same as in Figure 1.8b).

As expected from Figure 1.8 where the highest value of the magnetic field for the near-linear magnetic regime loading occurs on the right end of the conductor's cross section, the highest value of the normal components of the magnetic stress also occur in the same location, as depicted in Figure 1.9a and Figure 1.9c. For the high magnetic field and current, again as expected from the results in Figure 1.8, the normal components of the magnetic stress are uniform over the entire conductor: $\overset{m}{\sigma}_{xx}/\mu_0 m_s^2 = 0.30$ in Figure 1.10a and $\overset{m}{\sigma}_{yy}/\mu_0 m_s^2 = 0.68$ in Figure 1.10c.

Notice also that the dimensionless shear component of the magnetic stress is

significantly lower inside the conductor compared to its magnitude outside for both loadings: three orders of magnitude lower order in Figure 1.9b (3×10^{-12} vs 3×10^{-9}), and two orders of magnitude lower order in Figure 1.10b (3×10^{-3} vs 3×10^{-1}). The maximum normal magnetic stresses occur always inside the conductor. In contrast the maximum magnetic shear stress always occurs on the outside of the conductor's boundary and is the shear component of the Maxwell stress in vacuum. Notice also the rotated by $\pm\pi/4$ two symmetry axes of the shear stress fields as compared to the unique symmetry x-axis for the normal ones.

1.4.2 Two Conductors Under Magnetic Field and Same Direction Electric Currents

We continue with the investigation of the Lorentz forces on two parallel ferromagnetic conductors of circular section of radius R, subjected to parallel currents of the same, uniform current density $\boldsymbol{j} = j\boldsymbol{e}_z$ and a remote external magnetic field of magnitude $\boldsymbol{b}_0 = b_0\boldsymbol{e}_y$ (see geometry in Figure 1.5). The results are presented in Figure 1.11 and Figure 1.12 in dimensionless form, according to (1.4.1).

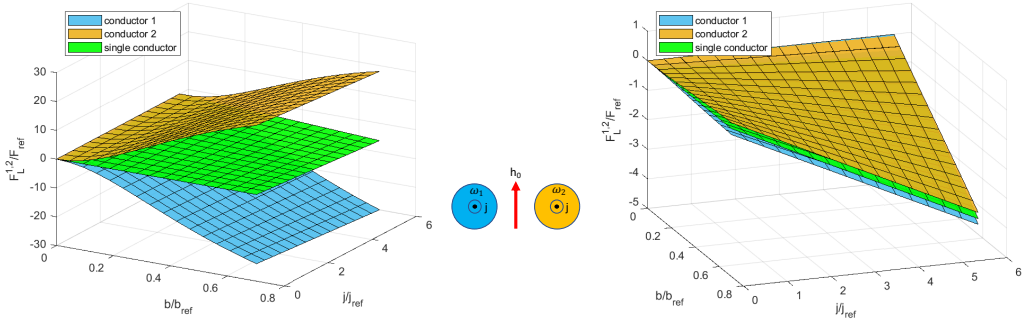

(a) $F_L^{1,2}/F_{ref}$ vs $(b_0/b_{ref}, j/j_{ref})$ for $D/R = 4.0$

(b) $F_L^{1,2}/F_{ref}$ vs $(b_0/b_{ref}, j/j_{ref})$ for $D/R = 20.0$

Figure 1.11: Dimensionless forces per unit length $F_L^{1,2}/F_{ref}$ as function of the remote magnetic field b_0/b_{ref} and the current density j/j_{ref} on two conductors with equal, same direction parallel currents $I = \pi jR^2$; in (a) at distance $D/R = 4$ and in (b) at distance $D/R = 20$. Lorentz force for the single conductor $-b_0 I/F_{ref}$ depicted in green for comparison.

Of interest is the influence of the conductor's magnetic properties on the Lorentz forces per unit length as function of their distance D. It is expected that for the closely spaced case ($D/R = 4$), the conductor's magnetic properties will be strongly influencing these forces, while for larger separation distances ($D/R = 20$) this influence will be considerably reduced, as these forces approach $\boldsymbol{F}_L^{1,2} = -b_0 I\boldsymbol{e}_x$ (plane

colored in green and depicted for comparison purposes in Figure 1.11). More specifically in Figure 1.11a we present the dimensionless forces per unit length $F_{L}^{1,2}/F_{ref}$ as function of the remote magnetic field b_0/b_{ref} and the current density j/j_{ref} for $D/R = 4$ and in Figure 1.11b for $D/R = 20$.

As expected from $(1.2.35)_1$ the forces on each conductor have different absolute values. For the closely spaced conductors $D/R = 4$ in Figure 1.11a, notice that in the absence of current ($j = 0$)[14] the Lorentz forces have opposite signs as expected for two adjacent magnetic dipoles with the same orientation; the forces increase in magnitude with increasing magnetic field b_0. As the electric currents increase, for a given external magnetic field, the Lorentz forces are only slightly affected, since the magnetic field is dominated by the magnetic properties of the conductor.

For the remotely spaced conductors $D/R = 20$ in Figure 1.11b notice that the Lorentz forces are an order of magnitude lower than their counterparts in Figure 1.11a. Although of different sign in the absence of currents (dipole repulsion), the Lorentz forces in the two conductors eventually share the same sign as the currents increase and converge to the single conductor limit $-b_0 I$, as one can observe in Figure 1.11b. It is also worth mentioning at this point that average between of two Lorentz forces is independent of the conductors magnetic properties, since from $(1.2.35)_1$ one has that $(F_{L}^{1} + F_{L}^{2})/2 = -b_0 I$.

We can thus conclude that for the closely spaced conductors in Figure 1.11a the Lorentz forces are dominated by the dipole repulsion effect due to the conductors' magnetic behavior, while for the remotely spaced conductors Figure 1.11b the Lorentz forces are practically unaffected by it.

[14] In the absence of an external magnetic field ($b_0 = 0$) the maximum value of the dimensionless Lorentz forces ($F_{L}^{1,2}/F_{ref} \approx \pm\mu_0 I^2/2\pi D F_{ref}$) are negligible – of the order of 10^{-3} – and hence not perceptible at the scale of the plots in Figure 1.11.

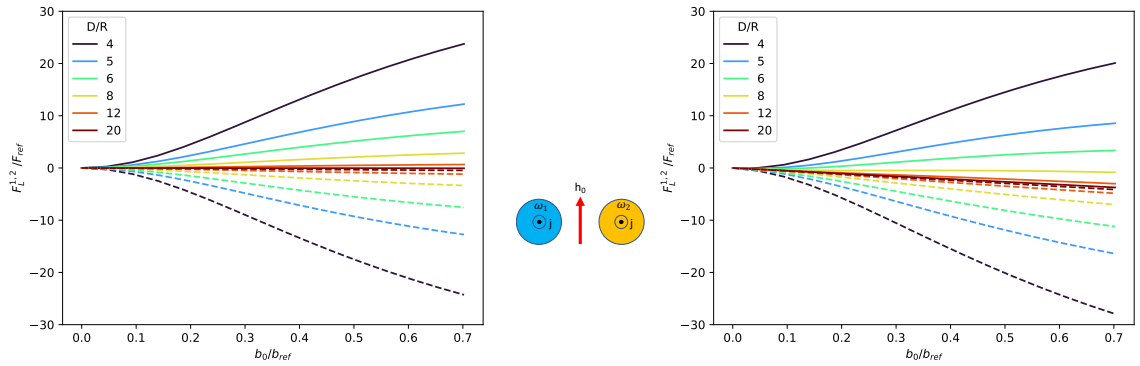

(a) $F_{L}^{1,2}/F_{ref}$ vs b_0/b_{ref} for $j/j_{ref} = 0.42$, $4 \leq D/R \leq 20$

(b) $F_{L}^{1,2}/F_{ref}$ vs b_0/b_{ref} for $j/j_{ref} = 6.36$, $4 \leq D/R \leq 20$

Figure 1.12: Influence of distance D/R on the dimensionless force per unit length $F_{L}^{1,2}/F_{ref}$ between two conductors with equal, same direction parallel currents $I = \pi j R^2$ as a function of the remote magnetic field b_0/b_{ref} at two different current densities; in (a) for $j/j_{ref} = 0.42$ and in (b) for $j/j_{ref} = 6.36$. Results for conductor 1 (left) are plotted in dashed lines while for conductor 2 (right) are plotted in solid lines (see Figure 1.5).

The influence of distance on the Lorentz forces per unit length for two identical parallel ferromagnetic conductors of circular section, subjected to currents of the same direction, as function of the applied remote external magnetic field b_0, and for different distances D/R, is presented in Figure 1.12. The results for conductor 1 (left) are plotted in dashed lines while for conductor 2 (right) are plotted in solid lines. More specifically Figure 1.12a corresponds to a low current density $j/j_{ref} = 0.42$ while Figure 1.12b corresponds to a high current density $j/j_{ref} = 6.36$.

By comparing Figure 1.12a to Figure 1.12b one can conclude that the ferromagnetic response of the conductors dominates the Lorentz forces, for the close distance and low current density case, while for the same distance an increase in the current density reduces these forces for conductor 1 and increases them for conductor 2. As the conductor distance increases, for a given external magnetic field both forces are significantly decreased, act in the same direction and converge to their common limit $F_{L}^{1} = F_{L}^{2} = -b_0 I$. The dominant factor influencing the Lorentz forces is the magnetic response of the conductor (hence the marked nonlinearity of the force-magnetic field curves for low values of D) and not the magnitude of the current, as evidenced by the results in Figure 1.12.

1.4.3 Two Conductors Under Magnetic Field and Opposite Direction Electric Currents

Next follows the investigation of the Lorentz forces on two parallel ferromagnetic conductors of circular section of radius R, subjected to parallel currents of the opposite direction, with a uniform current density and a remote external magnetic field of magnitude $\boldsymbol{b}_0 = b_0\boldsymbol{e}_y$, as depicted in Figure 1.5. Two possibilities exist: $\boldsymbol{j}_1 = j\boldsymbol{e}_z$, $\boldsymbol{j}_2 = -j\boldsymbol{e}_z$ (case i) and $\boldsymbol{j}_1 = -j\boldsymbol{e}_z$, $\boldsymbol{j}_2 = j\boldsymbol{e}_z$ (case ii). The results are presented in Figure 1.13 and Figure 1.14 in dimensionless form according to (1.4.1).

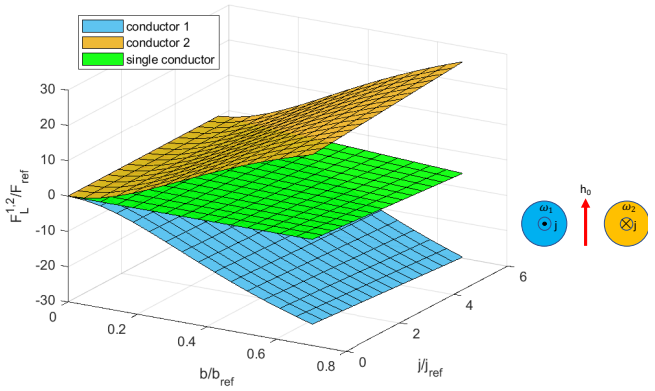

(a) $F_L^{1,2}/F_{ref}$ vs $(b_0/b_{ref}, j/j_{ref})$ for $D/R = 4.0$

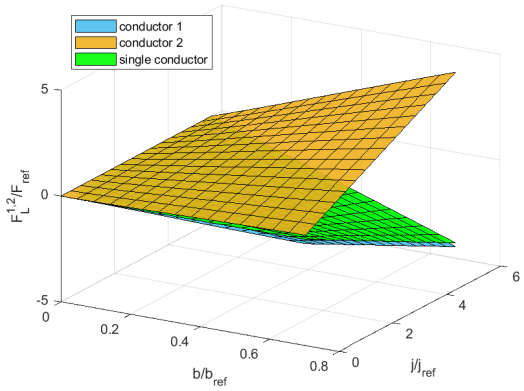

(b) $F_L^{1,2}/F_{ref}$ vs $(b_0/b_{ref}, j/j_{ref})$ for $D/R = 20.0$

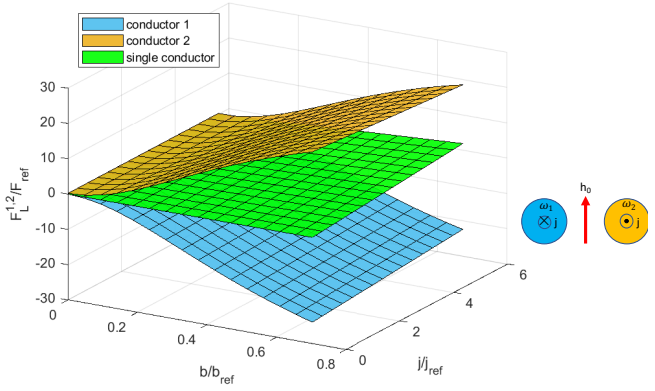

(c) $F_L^{1,2}/F_{ref}$ vs $(b_0/b_{ref}, j/j_{ref})$ for $D/R = 4.0$

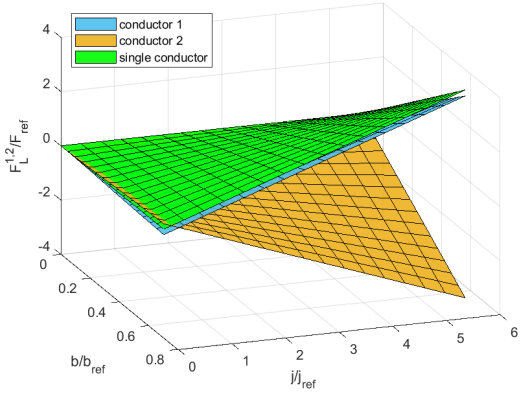

(d) $F_L^{1,2}/F_{ref}$ vs $(b_0/b_{ref}, j/j_{ref})$ for $D/R = 20.0$

Figure 1.13: Dimensionless forces per unit length $F_L^{1,2}/F_{ref}$ as function of the remote magnetic field b_0/b_{ref} and the current density j/j_{ref} on two conductors with equal, opposite direction parallel currents $I = \pi j R^2$ for $\boldsymbol{j}_1 = j\boldsymbol{e}_z$, $\boldsymbol{j}_2 = -j\boldsymbol{e}_z$ (case i, (a) and (b)) and $\boldsymbol{j}_1 = -j\boldsymbol{e}_z$, $\boldsymbol{j}_2 = j\boldsymbol{e}_z$ (case ii, (c) and (d)); in (a) and (c) at distance $D/R = 4$ and in (b) and (d) at distance $D/R = 20$. Lorentz force for the single conductor $-b_0 I/F_{ref}$ depicted in green for comparison.

Of interest again is the influence of magnetic properties on the Lorentz forces per unit length on each conductor as function of their distance D. More specifically in Figure 1.13a and Figure 1.13c we present the dimensionless forces per unit length $F_{L}^{1,2}/F_{ref}$ for cases (i) and (ii) respectively as function of the remote magnetic field: b_0/b_{ref} and the current density: j/j_{ref} for $D/R = 4$ and in Figure 1.13b and Figure 1.13d their counterparts for $D/R = 20$.

As expected from $(1.2.35)_2$ the forces on the two conductors always have opposite signs but the same absolute value. For the closely spaced conductors $D/R = 4$ in Figure 1.13a and Figure 1.13c, notice that in the absence of current ($j = 0$)[15] the Lorentz forces due to the interaction of two adjacent magnetic dipoles with the same orientation are the same as in Figure 1.11. As the electric currents increase, for a given external magnetic field, the Lorentz forces are only slightly affected since the magnetic field is dominated by the magnetic properties of the conductor.

For the remotely spaced conductors $D/R = 20$ in Figure 1.13b and Figure 1.13d the Lorentz forces are an order of magnitude smaller than their counterparts in Figure 1.13a and Figure 1.13c. Moreover these forces show very small sensitivity to the conductors' magnetic behavior, as one can observe in Figure 1.13b and Figure 1.13d. Moreover, in comparing the last two figures notice that the change of the current direction in each conductor results in a change of the sign of the Lorentz force.

We can thus conclude, like in the parallel current direction case, that for the closely spaced conductors in Figure 1.13a and Figure 1.13c the Lorentz forces are dominated by the dipole repulsion effect due to the conductors' magnetic behavior while for the remotely spaced conductors Figure 1.13b and Figure 1.13d the Lorentz forces are close to the single conductor limit $\pm b_0 I$ i.e. practically unaffected by magnetic properties.

[15]For no external magnetic field ($b_0 = 0$) see remark in footnote 14.

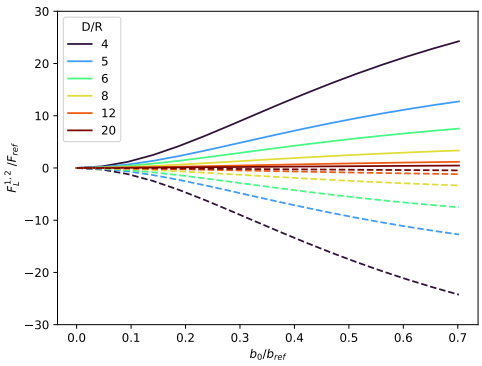

(a) $F_L^{1,2}/F_{ref}$ vs b_0/b_{ref} for $j/j_{ref} = 0.42$, $4 \leq D/R \leq 20$

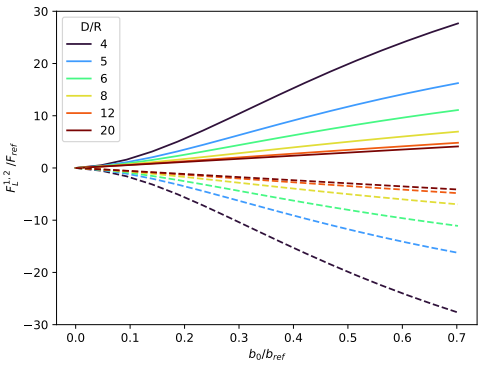

(b) $F_L^{1,2}/F_{ref}$ vs b_0/b_{ref} for $j/j_{ref} = 6.36$, $4 \leq D/R \leq 20$

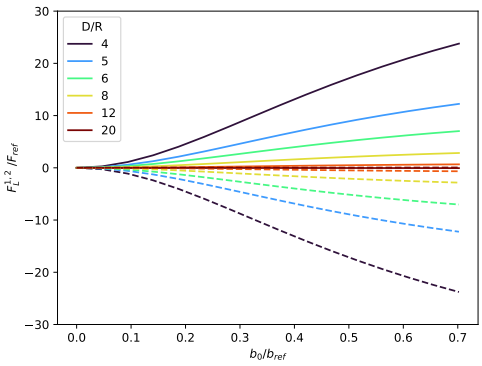

(c) $F_L^{1,2}/F_{ref}$ vs b_0/b_{ref} for $j/j_{ref} = 0.42$, $4 \leq D/R \leq 20$

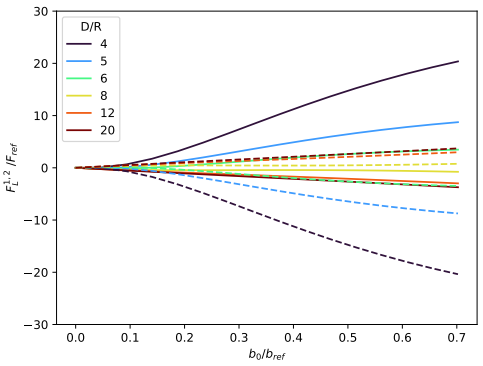

(d) $F_L^{1,2}/F_{ref}$ vs b_0/b_{ref} for $j/j_{ref} = 6.36$, $4 \leq D/R \leq 20$

Figure 1.14: Influence of distance D/R on the dimensionless force per unit length $F_L^{1,2}/F_{ref}$ between two conductors with equal, opposite direction parallel currents $I = \pi j R^2$ for $\boldsymbol{j}_1 = j\boldsymbol{e}_z$, $\boldsymbol{j}_2 = -j\boldsymbol{e}_z$ (case i, (a) and (b)) and $\boldsymbol{j}_1 = -j\boldsymbol{e}_z$, $\boldsymbol{j}_2 = j\boldsymbol{e}_z$ (case ii, (c) and (d)) as a function of the remote magnetic field b_0/b_{ref} at two different densities; in (a) and (c) for $j/j_{ref} = 0.42$ and in (b) and (d) for $j/j_{ref} = 6.36$. Results for conductor 1 (left) are plotted in dashed lines while for conductor 2 (right) are plotted in solid lines (see Figure 1.5).

The influence of distance on the Lorentz forces per unit length for two identical parallel ferromagnetic conductors of circular section, subjected to currents of the opposite direction, as function of the applied remote external magnetic field b_0, and for different distances D/R, is presented in Figure 1.14. The results for conductor 1 (left) are plotted in dashed lines while for conductor 2 (right) are plotted in solid lines. More specifically Figure 1.14a and Figure 1.14c for cases (i) and (ii) respectively correspond to a low current density $j/j_{ref} = 0.42$ while Figure 1.14b and Figure 1.14b for cases (i) and (ii) respectively correspond to a high current density $j/j_{ref} = 6.36$.

By comparing Figure 1.14a and Figure 1.14c to Figure 1.14b and Figure 1.14d one observes that the ferromagnetic response of the conductors dominates the Lorentz forces for the closely spaced case. Due to this dominance of the magnetic properties for the closely spaced conductors, by comparing Figure 1.14a to Figure 1.14c we observe that for the low current density, reversing of the current direction has no observable effect on the Lorentz forces. As the conductor distance increases the (always opposite direction) forces converge to the same absolute value (non ferromagnetic) limit $b_0 I$.

However the change of the current direction has a noticeable effect for the high current density, as one can observe by comparing Figure 1.14b to Figure 1.14d. According to Figure 1.14d, the absolute value of the forces are significantly lower for case (ii) where they eventually change sign as the distance between the conductors increases, while as seen for case (i) in Figure 1.14b the Lorentz forces in each conductor are always of the same sign.

1.4.4 Periodic Array of Conductors Under Magnetic Field and Alternating Directions Electric Currents

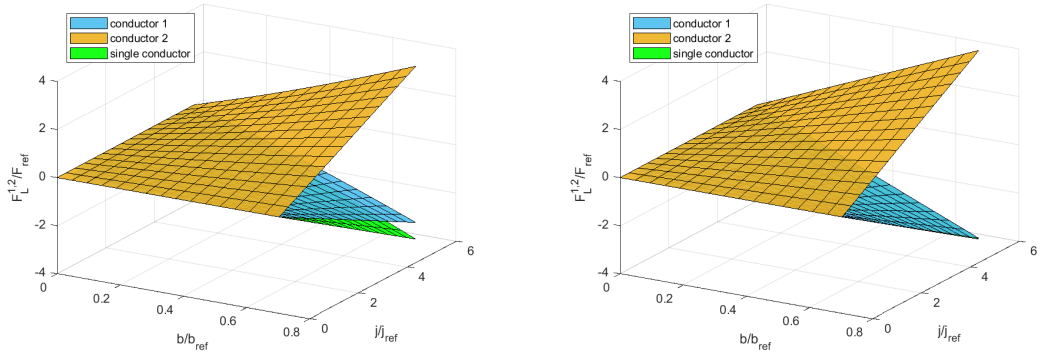

(a) $F_L^{1,2}/F_{ref}$ vs $(b_0/b_{ref}, j/j_{ref})$ for $D/R = 4.0$

(b) $F_L^{1,2}/F_{ref}$ vs $(b_0/b_{ref}, j/j_{ref})$ for $D/R = 20.0$

Figure 1.15: Dimensionless forces per unit length $F_L^{1,2}/F_{ref}$ as function of the remote magnetic field b_0/b_{ref} and current density j/j_{ref} in an infinite array of equally spaced conductors with alternating direction parallel currents $I = \pi j R^2$; in (a) at distance $D/R = 4$ and in (b) at distance $D/R = 20$. Lorentz force for the single conductor $-b_0 I/F_{ref}$ depicted in green for comparison.

We conclude with the investigation of the Lorentz forces on a parallel array of equally spaced ferromagnetic conductors of circular section of radius R, subjected to same magnitude currents in alternating directions, with a uniform current density $\boldsymbol{j} = \pm j \boldsymbol{e}_z$ and a remote external magnetic field of magnitude $\boldsymbol{b}_0 = b_0 \boldsymbol{e}_y$, as depicted in

Figure 1.6. The results are presented in Figure 1.18 and Figure 1.16 in dimensionless form according to (1.4.1).

Of interest once again is the influence of magnetic properties on the Lorentz forces per unit length on each conductor as function of their distance D. More specifically in Figure 1.18a we present the dimensionless forces per unit length $F_L^{1,2}/F_{ref}$ as function of the remote magnetic field: b_0/b_{ref} and the current density: j/j_{ref} for $D/R = 4$ and in Figure 1.18b for $D/R = 20$.

Unlike for the two conductors presented in Section 1.4.2 and Section 1.4.3, in the absence of electric currents ($j = 0$), symmetry dictates the Lorentz forces in each conductor to vanish for any value of the external magnetic field, as one can observe in Figure 1.18. In addition, the Lorentz forces for the two different conductor spacings are of the same order of magnitude. Moreover for given current density and magnetic field, the Lorentz forces are smaller for the more closely spaced conductors $D/R = 4$ than for their more remote counterpart $D/R = 20$, as one can see by comparing Figure 1.18a to Figure 1.18b. The presence of magnetization in the conductor has the counterintuitive effect of weakening the Lorentz forces. Moreover, these forces are almost linearly dependent on the magnetic field and current, as seen from the almost flat surfaces in Figure 1.18.

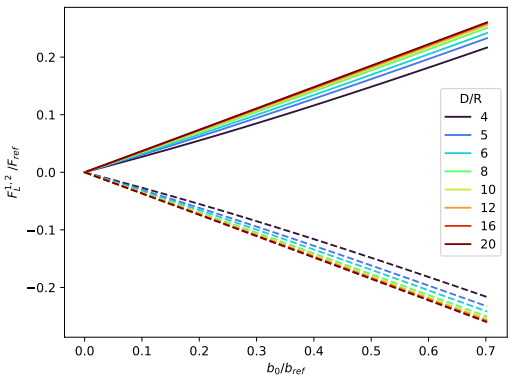

(a) $F_L^{1,2}/F_{ref}$ vs b_0/b_{ref} for $j/j_{ref} = 0.42$ and $4 \leq D/R \leq 20$

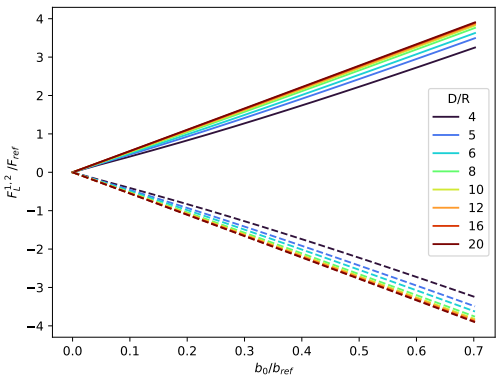

(b) $F_L^{1,2}/F_{ref}$ vs b_0/b_{ref} for $j/j_{ref} = 6.36$ and $4 \leq D/R \leq 20$

Figure 1.16: Influence of distance D/R on the dimensionless force $F_L^{1,2}/F_{ref}$ between two adjacent conductors in an infinite array with alternating direction parallel currents $I = \pi j R^2$ as a function of the remote magnetic field b_0/b_{ref} at two different current densities; in (a) for $j/j_{ref} = 0.42$ and in (b) for $j/j_{ref} = 6.36$. Results for conductor 1 (left) are plotted in dashed lines while for conductor 2 (right) are plotted in solid lines (see Figure 1.6).

The influence of distance on the Lorentz forces per unit length for on a parallel array of equally spaced ferromagnetic conductors of circular section of radius R,

subjected to same magnitude parallel currents in alternating directions, as function of the applied remote external magnetic field b_0, and for different distances D/R, is presented in Figure 1.16. The results for conductor 1 are plotted in dashed lines while for conductor 2 are plotted in solid lines. More specifically Figure 1.16a corresponds to a low current density $j/j_{ref} = 0.42$ while Figure 1.16b corresponds to a high current density $j/j_{ref} = 6.36$. The significant current density increase dictated the different scales for plotting the Lorentz forces in Figure 1.16a and Figure 1.16b.

By comparing Figure 1.12 and Figure 1.14 to Figure 1.16 one can draw two conclusions. The first is that the magnetic properties of the conductors have considerably less influence on the Lorentz forces in the periodic arrangement, as evidenced by the almost linear force vs magnetic field response which is rather insensitive to the distance between conductors: difference with the non-magnetic case ranging from 18% for $D/R = 4$ and rapidly decreasing to 3% for $D/R = 10$. The second conclusion is the counterintuitive result of an increasing force as the distance between conductors increases, a result of the repulsive dipole-dipole interaction magnetization-induced forces that decrease with increasing distance between conductors. Observe that Figure 1.12 and Figure 1.14 are plotted at a different scale than Figure 1.16, due the significant reduction in the Lorentz forces for the periodic conductor case.

1.4.5 2D periodic array of conductors Subjected to Magnetic Field and Alternating Direction Electric current

One simple extension to the previous work is to study what would happen if we were considering an array of wires periodic in the x and y direction as depicted in **??**. In this conficuration, we will concider that the current in the bottom left and top right wires is positive, and the one in the bottom right and top left wires id negative. Taking the opposite convention is equivalent and would simply gives the opposite forces. In this configuration an analysis simmilar to the ones carried out before gives that the sum of all four forces is null. In addition, by symmetry and periodicity, it is immediate that the forces in wires subjected to the same current will be identical. We will cal $F_L^1$the force over the bottom left and top right wires and F_L^2 the force over the bottom right and top left wires.

The results for the resultant forces in x are presented in Figure 1.18 and Figure 1.16 in dimensionless form according to (1.4.1). There are no resultant forces in the y direction.

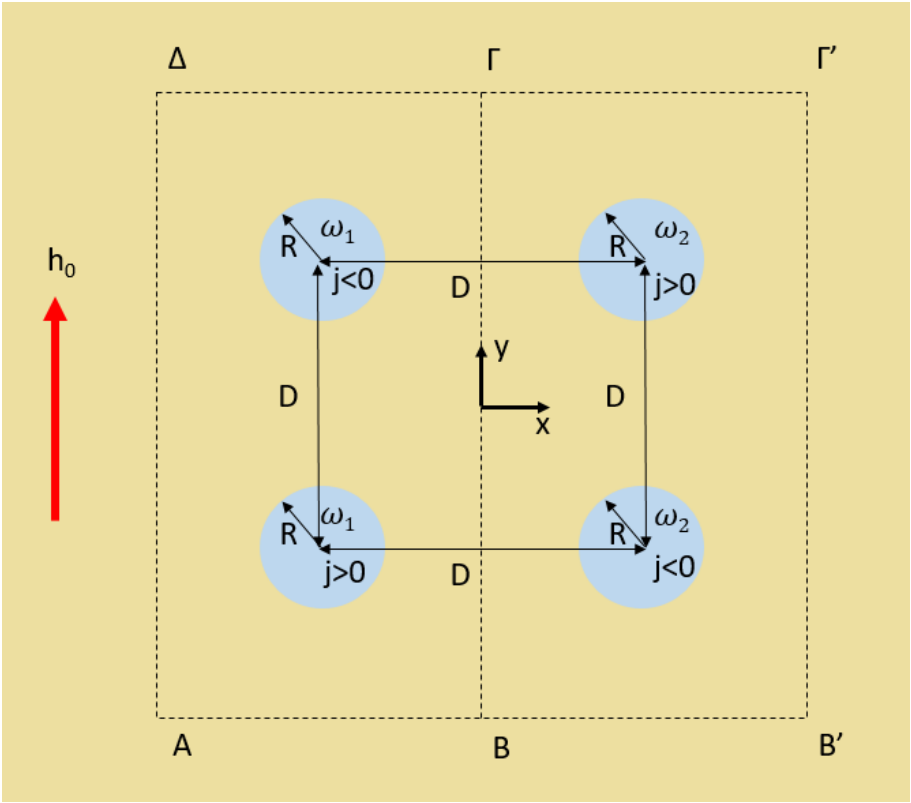

Figure 1.17: Calculating the Lorentz forces F_L on a a 2D array of conductor subjected to current of density j of alternating direction and a remote h-field of magnitude h_0 using contour integrals.

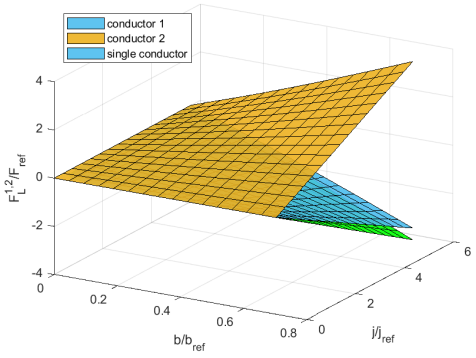

(a) $F_L^{1,2}/F_{ref}$ vs $(b_0/b_{ref}, j/j_{ref})$ for $D/R = 4.0$

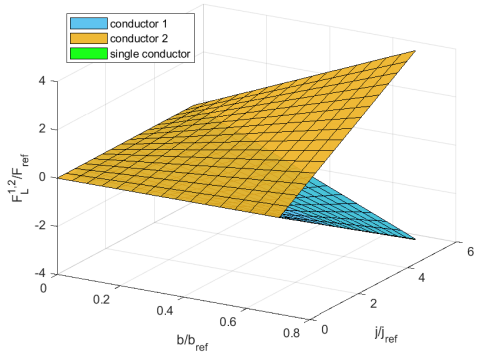

(b) $F_L^{1,2}/F_{ref}$ vs $(b_0/b_{ref}, j/j_{ref})$ for $D/R = 20.0$

Figure 1.18: Dimensionless forces per unit length $F_L^{1,2}/F_{ref}$ as function of the remote magnetic field b_0/b_{ref} and current density j/j_{ref} in an infinite array of equally spaced conductors with alternating direction parallel currents $I = \pi j R^2$; a) at distance $D/R = 4$ and b) at distance $D/R = 20$. Lorentz force for the single conductor $-b_0 I/F_{ref}$ depicted in green for comparison purposes.

Of interest once again is the influence of magnetic properties on the Lorentz forces per unit length on each conductor as function of their distance D. More specifically in Figure 1.18a we present the dimensionless forces per unit length $F_{L}^{1,2}/F_{ref}$ as function of the remote magnetic field: b_0/b_{ref} and the current density: j/j_{ref} for $D/R = 4$ and in Figure 1.18b for $D/R = 20$. The key take away of this caculation is that adding infinite layers has negligable impact on the resultant forces. The conclusions about the single periodic layer of conductors stays true.

1.5 Conclusion

Although the problem of Lorentz forces on electrical current carrying conductors subjected to a remote magnetic filed is a classical one, the impact of the conductors' magnetic properties on the forces between two or more (in a periodic array) parallel conductors subjected to a uniform external magnetic field and current density has not been the subject of investigations to the best of the authors' knowledge, thus motivating the present study.

As discussed in Section 1.2.4, the calculation of Lorentz forces requires solely the determination of the Maxwell stresses in vacuum, i.e. the magnetic field $\boldsymbol{b}$ outside the conductors. Consequently the continuum 2D numerical calculations (FEM) are considerably simplified for this multiphysics problem, since they involve only the scalar magnetic potential $a(x, y)$ (recall $\boldsymbol{a} = a(x, y)\boldsymbol{e}_z$).

The case of two closely spaced conductors $D/R = 4$ is particularly interesting, since the magnetic fields outside the conductors are strongly influenced by the magnetic constitutive law and the resulting magnetic dipole repulsion between the to conductors far outweighs the current-induced forces as one can see in Figure 1.12 and Figure 1.14. At large distances $D/R = 20$ the Lorentz forces reduce to the classical result of a single wire in a uniform magnetic field ($F_{L}^{1,2} = \pm b_0 I$). One can thus significantly enhance the Lorentz forces in two closely-spaced parallel conductors by using ferromagnetic materials.

The results for an infinite array of parallel, equally spaced conductors are rather surprising, if not counterintuitive. For currents in the same direction the conductors' magnetic properties have no influence on the Lorentz forces due to symmetry arguments. For the case of currents in alternating directions, the magnetic properties of the conductors only slightly reduce the Lorentz forces due to dipole interactions and these forces are essentially linearly dependent on both the magnetic field and applied current, as attested by the flat surfaces results in Figure 1.18 and the straight lines in Figure 1.16. More complicated, multilayer arrays of conductors can be analyzed in exactly the same manner as the single layer array considered here.

The results of this investigation pertain to unsupported conductors, since they are surrounded by vacuum, which in view of the linear momentum equation (1.2.20) will induce motion, as an acceleration term will result from the Lorentz forces. In case when the conductors are imbedded in a non-conducting elastomeric matrix,

mechanical tractions will appear on the boundaries of the conductors and the fully coupled mechanical-electromagnetic problem presented in Section 1.2 must be solved to concurrently obtain both the magnetic field $\boldsymbol{b}$ and the displacement field $\boldsymbol{u}$. From this equilibrium solution one could find the elastic stresses $\overset{e}{\boldsymbol{\sigma}}$ inside the conductors as in Hanappier et al. (2022) for small strains or Lefevre et al. (2020) for large strains.

Chapter 2

Analysis of a partially magnetizable current carrying mesh subjected to magnetic fields

The study of the mechanical behavior of honeycomb and more generally architected materials has seen strong interest, especially since their ever increasing use in the industry where their remarquable mechanical properties (stiffness to mass ratio in one direction for instance) are greatly appreciated. A review of recent advances can be found in Surjadi et al. (2019). However, such materials require great care when it comes to their mechanical stability, which is often their failure mode far before fracture. The theory behind those buckling analysis and its application to truss configurations can be found in Triantafyllidis and Schnaidt (1993). The buckling modes are often characterized by their pulsations (one per direction), i.e. the ratio of the buckling mode length and the cell length regarding each direction. Then the bifurcations are grouped in two categories. First, local bifurcations which correspond to a non 0 pulsation and that can be obtained through the Bloch theorem. Second, global modes that can be obtained either by studying bloch waves with pulsations $\omega_c \to 0$ or, as shown in Müller et al. (1993), by looking at the loss of rank one convexity of the homogenized modulus. In this chapter we will use the first option. More discussion about the second one will be provided in Chapter 3 Focusing on our geometry, square honeycombs, there are plenty of works including both experimental and analytical approaches. As this geometry has been identified as very efficient for shock absorption, a significant part of the literature studies the dynamic behavior both under out of plane loadings (see Xue and Hutchinson (2006)) and in plane loadings (see Tao et al. (2019)), but it is not the focus of this work. In the quasistatic case, the load cases studied in the literature include both in plane (Russell et al. (2008)) and out of plane (Côté et al. (2004)) compression. But as far as the author is aware, no work has been conducted considering the type of load generated by our electromagnetic forces: loads that apply only to part of the beams. Finally,

there are several works focusing on mixed structure such as Tao et al. (2019) with hierarchical structure and Côté et al. (2009) with square honeycomb composed of sandwich panels, but, once again only homogeneous loadings are considered. For the sake of completeness, we point out that two aspects of the study of the stability of architected materials often found in the literature won't be addressed in this chapter. First, The geometry will be considered perfect, without initial perturbation. An example of a study tackling this problem in the case of a ductile media with periodic micro-structures under finite strains can be found in Schraad and Triantafyllidis (1997). Second, the first bifurcation does not necessarily indicate a catastrophic failure. Understanding the behavior of the material after the initial loss of stability is called post-bifurcation analysis and can be achieved either by imperfection methods or by analytical group theory methods. An example of the latter, in the case of a two-dimensional infinite perfect periodic honeycomb can be found in Combescure et al. (2016). In our case, as we will show that the first instability requires a loading higher than what can be achieved experimentally, we won't study the behavior past the first loss of stability. The outline is the following: After describing the system and its parameters in Section 2.1, we compute the principal solution in Section 2.2. In Section 2.3 we show the method used to study the mechanical stability of the system, and the resulting results are provided in Section 2.4.

2.1 Problem description

In the previous chapter we obtained the resultant forces in several configurations. However the only configuration which created significant compressive forces is the array of periodic wires with alternating current directions. Indeed when considering two wires the dominant forces for reasonably close wires are repulsive, and in a periodic array of wires with parallel currents all the resultant forces share the same direction. As a consequence, this stability analysis will focus on the first configuration mentioned. The global problem is described in Figure 2.1. We will use $_v$ for quantities related to the vertical beams and $_h$ for quantities related to the horizontal ones. We consider an elastic magnetizable horizontal beam of radius r_h carrying a current $\pm I e_y$ with the sign alternating between each layer. The vertical beams are elastic, non magnetic, non conductive and their radius is r_v. These beams form squares of size $l_v \times l_h$. An exterior magnetic field b_0 along e_z is added. The Young's moduli of each beam are respectively E_v and E_h According to the previous section, we know that the resultant forces per unit of length q will be of equal magnitude but alternating direction between the horizontal layers ($q = \pm f,\ f \geq 0$). As we do not consider pre stress in the absence of magnetic loading and we let the global system compress axially freely, we get that the exterior forces applied to the system lead to no axial forces in the horizontal beams, a constant axial force $\lambda = f l_h$ in half the vertical beams, and no axial forces in the other half. As explained previously, when needing a specific configuration, we will consider the system composed of the metallic beam

studied in chapter 2 as horizontal beams, and plastic beams whose radius is half the radius of the horizontal beams. The length of the beam will vary between 1cm and 10 cm for experimental constraints.

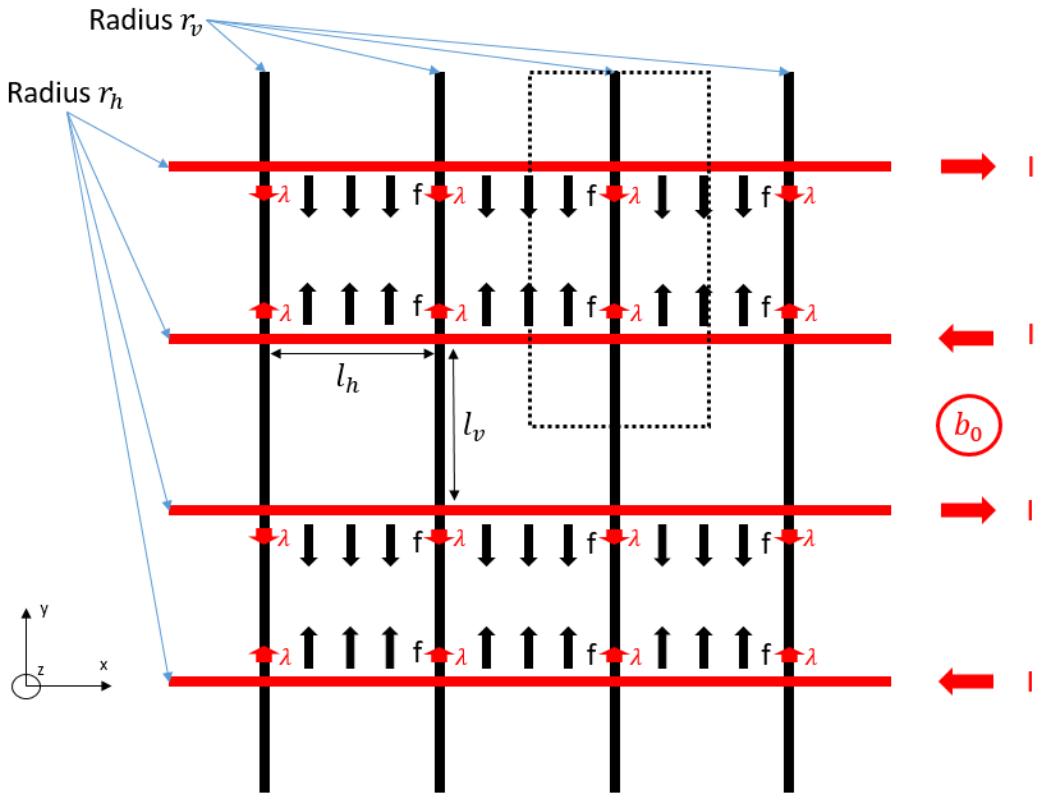

Figure 2.1: Schematic of an infinite mesh under an exterior magnetic field and currents. The red beams are magnetizable conductors carrying the current. The black ones are non conductive and non magnetizable.

2.1.1 Unit cell

In order to solve this infinite problem, we can study the unit cell shown in Figure 2.2. Its dimensions are $L_x = l_h$ and $L_y = 2l_v$. We are going to treat this problem as an elastic planar truss loaded by the magnetic forces obtained in the previous chapter. This truss is composed of 7 different beams named based on their edge point. For instance we call (28) the beam linking point 2 and point 8. As shown in Figure 2.2, there are 3 types of beam:

- 4 horizontal beams (37,76,28,85) of length $l_h/2$, radius r_h, elasticity modulus E_h and subject to no axial force and a tangential force per unit of length $\pm f$.

- 2 vertical beams (18,74) of length $l_v/2$, radius r_v, elasticity modulus we will call E_v and subject to no axial force and no tangential forces.

- one vertical beam (87) of length $l_v/2$, radius r_v, elasticity modulus we will call E_v and subject to an axial force λ and no tangential forces

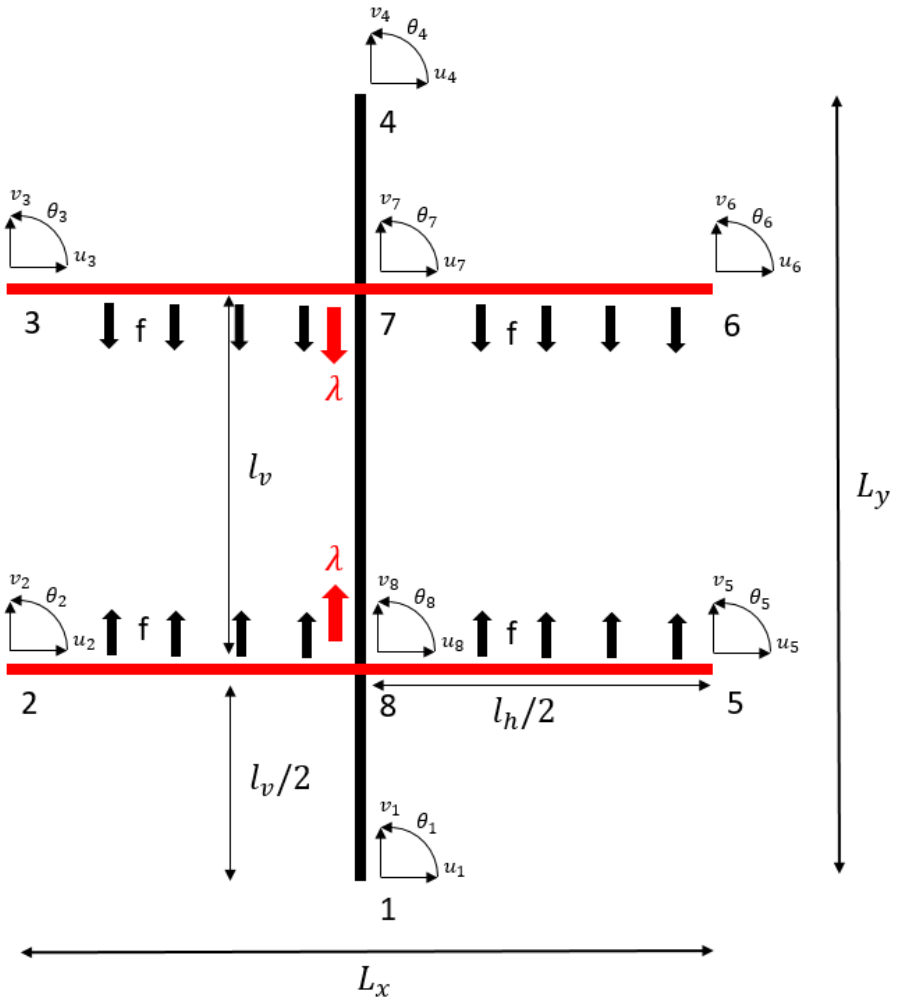

Figure 2.2: Schematic of the unit cell with the numbering of the points, the d.o.f and the geometrical parameters

This problem is fully described by the position and orientation at the edge of each beams. Thus it can be described by 24 d.o.f : x displacement, y displacement and rotation angle at each of the 8 points. The global d.o.f vector is $[U] = [u_1, v_1, \theta_1, ..., u_8, v_8, \theta_8]^T$

2.2 Principal solution

The principal solution of this problem is very straightforward : there is an axial compression in the beam (78) and deflections in the horizontal beams (37,76,28,85). We consider the point 1 fixed at coordinates (0,0) (ie $u_1 = v_1 = 0$) to get rid of the rigid body movement. It comes immediately from balance of forces and moments and from the equations for a a 2D beam that :

- $\theta_1 = 0$
- As the moments from the beams (28) and (85) balances out, and there is no axial stress in (18), $u_8 = v_8 = \theta_8$=0
- As the moments from the beams (3) and (6) balances out, and the axial stress in the beam (18) is λ, $v_7 = -\lambda l_v/(E_v A_v)$ and $u_7 = \theta_7$=0
- As there is no axial load in (74), $v_4 = v_7 = -\lambda l_v/(E_v A_v)$ and $u_4 = \theta_4$=0
- u_2, v_2, θ_2 are obtained by solving the beams equations with the boundary conditions obtained for the points 7 and 8

The equations for a beam of length L, of axial stiffness EA and bending stiffness EI under an axial force λ and a tangential force per unit of length q are the following.

$$\frac{d(EA\epsilon(x))}{dx} = 0 \Leftrightarrow \epsilon(x) = \frac{du}{dx}(x) + \frac{1}{2}(\frac{dv}{dx}(x))^2 = \frac{-\lambda}{EA} \tag{2.2.1}$$

$$EI\frac{d^4v}{dx^4}(x) - \frac{d}{dx}[EA\epsilon(x)\frac{dv}{dx}(x)] = q \Leftrightarrow EI\frac{d^4v}{dx^4}(x) + \lambda\frac{d^2v}{dx^2}(x) = q \tag{2.2.2}$$

In the horizontal beam, as we do not lock horizontal displacement, there is no axial load. Thus the relations becomes

$$\begin{cases} \frac{du}{dx}(x) + \frac{1}{2}(\frac{dv}{dx}(x))^2 = 0 \\ EI\frac{d^4v}{dx^4}(x) = q \end{cases} \tag{2.2.3}$$

The boundary conditions for the horizontal beams considered are

$$\begin{cases} u(0) = 0 \\ v(0) = v(L) \\ \theta(0) = \theta(0) = 0 \end{cases}$$

It leads to

$$u(x) = -\frac{1}{2}\int_0^x (\frac{dv}{dx}(s))^2 ds; \qquad v(x) = \frac{q}{24EI}(L^2x^2 - 2Lx^3 + x^4) + v(0) \tag{2.2.4}$$

By using boundary conditions, we obtain the following results for the main path :

$$
\begin{array}{lll}
u_1 = 0 & v_1 = 0 & \theta_1 = 0 \\
u_2 = \dfrac{l_h^9 f^2}{1451520 E_h I_h}; & v_2 = \dfrac{l_h^4 f}{384 E_h I_h}; & \theta_2 = 0 \\
u_3 = \dfrac{l_h^9 f^2}{1451520 E_h I_h}; & v_3 = -\dfrac{l_h^4 f}{384 E_h I_h} - \dfrac{f l_h l_v}{E_v A_v}; & \theta_3 = 0 \\
u_4 = 0; & v_4 = -\dfrac{f l_h l_v}{E_v A_v} & \theta_4 = 0 \\
u_5 = -\dfrac{l_h^9 f^2}{1451520 E_h I_h}; & v_5 = \dfrac{l_h^4 f}{384 E_h I_h}; & \theta_5 = 0 \\
u_6 = -\dfrac{l_h^9 f^2}{1451520 E_h I_h}; & v_6 = -\dfrac{l_h^4 f}{384 E_h I_h} - \dfrac{f l_h l_v}{E_v A_v}; & \theta_6 = 0 \\
u_7 = 0; & v_7 = -\dfrac{f l_h l_v}{E_v A_v} & \theta_7 = 0 \\
u_8 = 0 & v_8 = 0 & \theta_8 = 0
\end{array}
$$

In the considered case of steel beams of radius 1,5mm, and the maximum magnetic forces considered in the previous chapter ($b_0 = 0.7 b_{ref}, j = 6.36 j_{ref}, ie\ \ b_0 = 1.5T, I = 20A, f = 30N/m$), and even for a a beam length of 10 cm, the deflection is under 10^{-5} m. Similarly, the horizontal changes are very small, below 10^{-12} m. Considering a plastic Young's modulus of E_v=2 GPa, and a radius for the plastic wires of $r_v = 0,75mm$, and large cells of $l_h = l_v = 10$ cm, the vertical displacement is still under 10^{-4} m Those results stand as long as the system stays mechanically stable. As the displacement in the horizontal beam is very small, we are going to neglect it when computing the stability of the system.

2.3 Stability analysis

In order to study the stability of this cell, we need to get the sign of determinant of the global stiffness matrix about the principal solution depending on the loading λ ie $[K](\lambda) = [\frac{\partial^2 \mathscr{E}}{\partial [U] \partial [U]}|_0](\lambda)$. As there is no prestress, the global stiffness matrix is positive definite when $\lambda = 0$. The critical load λ_c is the lowest value of the load λ where the global stiffness loses its positive definiteness, as the load increases from zero.

$$Det[K(\lambda_c)] = 0\ , \quad \forall \lambda \in [0, \lambda_c[\ Det[K(\lambda)] > 0\ ; \tag{2.3.1}$$

As usual when dealing with truss, we will find the global stiffness matrix [K] by assembling the stiffness matrix of all the beams such that [K] [U] = [F] with [F] the global load vector.

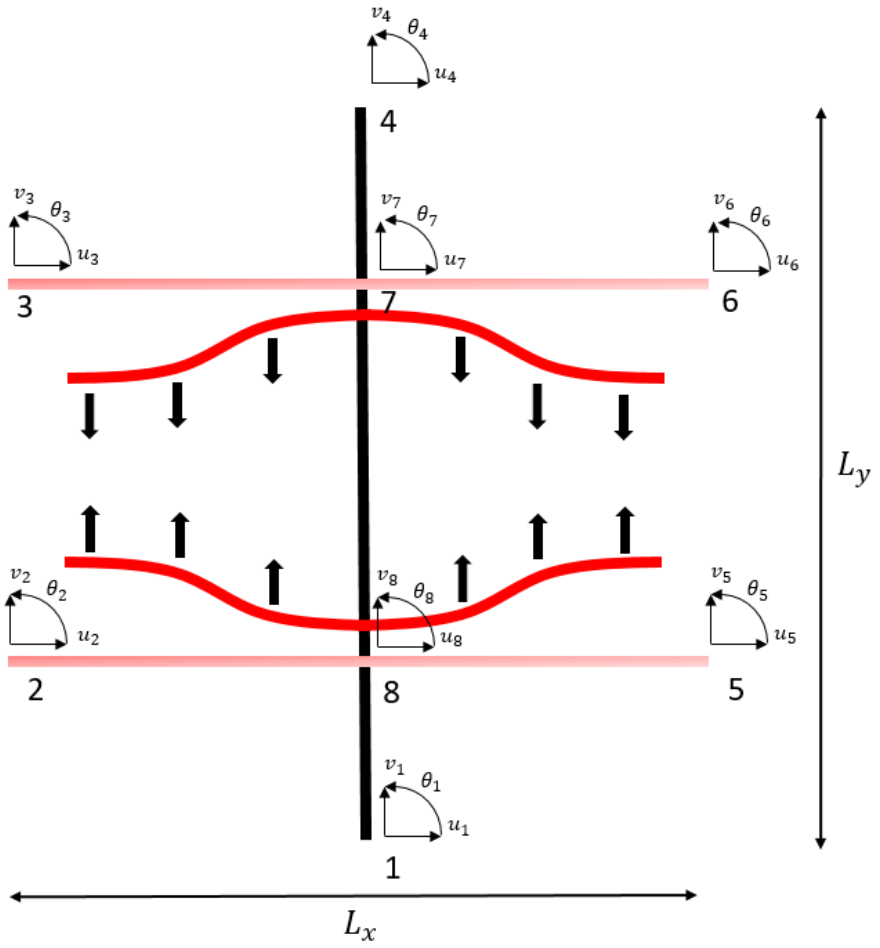

Figure 2.3: Principal solution for the unit cell under the considered load. The faded red beams indicate the reference configuration

2.3.1 Single beam

For the sake of completeness, we derive the general solution of a single elastic beam of length l aligned in the global x direction, of radius r, of constant axial stiffness $EA = E\pi r^2$ and of constant bending stiffness $EI = E\frac{\pi r^4}{4}$ as depicted in Figure 2.4. This beam will be under an axial load λ and no tangential forces. To be fully accurate, we should take into account the impact of the deflection due to the force f in the horizontal beams, but as they have to be magnetizable conductors, and considering the mechanical properties of common metallic materials, those deflection will be very small in amplitude. We will neglect this effect. We call [u] the vector of d.o.f of this beam such that $[u] = [u_1, v_1, \theta_1, u_2, v_2, \theta_2]^T$ Using a variational approach to solve the stability problem, we need to express the second derivative of the energy about the principal solution and in terms of our d.o.f [u] and the loading λ. The energy of a

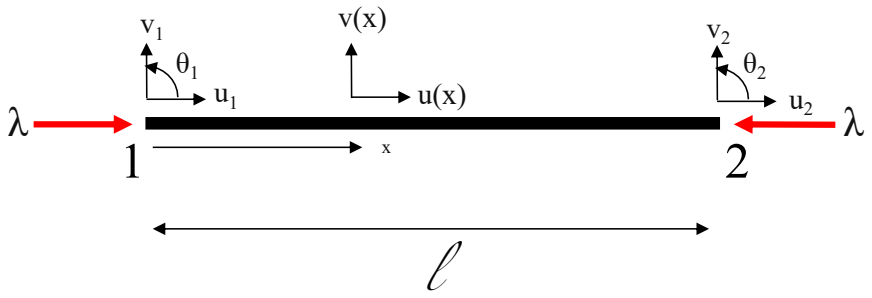

Figure 2.4: Schematic of an axially loaded beam and its d.o.f

2D beam with axial and normal displacement u(x) and v(x) as shown in Figure 2.4 is given by :

$$\begin{aligned} &\mathscr{E} = \frac{1}{2}\int_0^l (EA(\epsilon(x))^2 + EI(k_y(x))^2)dx, \\ &\text{with } \epsilon(x) = \frac{du}{dx}(x) + \frac{1}{2}\Big(\frac{dv}{dx}(x)\Big)^2 \text{ and } k_y(x) = -\frac{d^2v}{dx^2}(x) \end{aligned} \tag{2.3.2}$$

To be able to assemble the different matrices, we need to express this energy as a function of our d.o.f [u]. This is achieved by solving the following boundary value problem:

$$\begin{cases} \mathscr{E}_{,u}\delta u = 0 \\ \mathscr{E}_{,v}\delta v = 0 \\ u(0) = u_1,\ v(0) = v_1,\ \theta(0) = \theta_1 \\ u(l) = u_2,\ v(l) = v_2,\ \theta(l) = \theta_2 \end{cases} \tag{2.3.3}$$

The two euler lagrange equations leads to

$$\mathscr{E}_{,u}\delta u = 0 \Rightarrow \frac{d(EA\epsilon(x))}{dx} = 0 \Leftrightarrow \epsilon(x) = \frac{du}{dx}(x) + \frac{1}{2}(\frac{dv}{dx}(x))^2 = \frac{-\lambda}{EA} \tag{2.3.4}$$

$$\mathscr{E}_{,v}\delta v = 0 \Rightarrow EI\frac{d^4v}{dx^4}(x) - \frac{d}{dx}[EA\epsilon(x)\frac{dv}{dx}(x)] = 0 \Leftrightarrow EI\frac{d^4v}{dx^4}(x) + \lambda\frac{d^2v}{dx^2}(x) = 0 \tag{2.3.5}$$

Assuming a compressive load ($\lambda \geq 0$), and using $\mu = \sqrt{\frac{\lambda}{EI}}$, we get the following solutions :

$$u(x) = C_0 - \frac{\lambda x}{EA} - \frac{1}{2}\int_0^x (\frac{dv}{dx}(s))^2 ds; \quad v(x) = C_1 sin(\mu x) + C_2 cos(\mu x) + C_3\mu x + C_4$$

(2.3.6)

By plugging Equation 2.3.6 in Equation 2.3.2, we obtain the following expression for the energy :

$$\mathscr{E} = \frac{\mu^3 EI}{2}\int_0^{\mu l}(C_1 sin(s)+C_2 cos(s))^2 ds+\frac{EA}{2l}\left(u_2-u_1+\frac{\mu}{2}\int_0^{\mu l}(C_1 cos(s)-C_2 sin(s)+C_3)^2 ds\right)^2 \tag{2.3.7}$$

It comes as no surprise that C_0 and C_4 do not appear in this energy as they correspond to rigid body displacement of the beam. The constant C_1, C_2, C_3 can be expressed in terms of $v_1, v_2, \theta_1, \theta_2$ using the boundary conditions in Equation 2.3.3. Those boundary conditions can be expressed as :

$$\begin{cases} u_1 = C_0 \ , & u_2 = C_0 - \dfrac{\lambda l}{EA} - \dfrac{\mu}{2}\displaystyle\int_0^{\mu l}(C_1\cos y - C_2 \sin y + C_3)^2\, dy \ , \\ v_1 = C_2 + C_4 \ , & v_2 = C_1 \sin(\mu l) + C_2\cos(\mu l) + C_3(\mu l) + C_4 \ , \\ \theta_1 = \mu(C_1 + C_3) \ , & \theta_2 = \mu(C_1\cos(\mu l) - C_2\sin(\mu l) + C_3) \ . \end{cases} \tag{2.3.8}$$

which leads to the following formulas

$$\begin{cases} C1 = \dfrac{(\theta_1-\theta_2)\cos(l\mu)+\mu(v_1-v_2)\sin(l\mu)-\theta_1+\theta_2}{2\mu(\cos(l\mu)-1)} \\ C2 = \dfrac{\cos^2\left(\frac{l\mu}{2}\right)\csc(l\mu)(-\mu(v_1-v_2)\cot(l\mu)+\mu(v_1-v_2)\csc(l\mu)+\theta_1-\theta_2)}{\mu} \\ C3 = -\dfrac{-(\theta_1+\theta_2)\cos(l\mu)+\mu(v_1-v_2)\sin(l\mu)+\theta_1+\theta_2}{2\mu(\cos(l\mu)-1)} \end{cases} \tag{2.3.9}$$

The principal solution is obtained when $C_1 = C_2 = C_3 = 0$ which correspond to $u_2 - u_1 = -\frac{\lambda l}{EA}, v_2 - v_1 = \theta_1 = \theta_2 = 0$ To study the stability we will need the second derivative of the energy about the principal solution.

$$[k] = \begin{bmatrix} k_{11} & k_{12} \\ k_{21} & k_{22} \end{bmatrix} = \begin{bmatrix} \dfrac{\partial^2\mathscr{E}}{\partial[u_1]\partial[u_1]}\Big|_0 & \dfrac{\partial^2\mathscr{E}}{\partial[u_1]\partial[u_2]}\Big|_0 \\ \dfrac{\partial^2\mathscr{E}}{\partial[u_2]\partial[u_1]}\Big|_0 & \dfrac{\partial^2\mathscr{E}}{\partial[u_2]\partial[u_2]}\Big|_0 \end{bmatrix}$$

where $|_0$ means an evaluation about the principal solution. We use $[u_1] = [u_1, v_1, \theta_1]^T$ and $[u_2] = [u_2, v_2, \theta_2]^T$ After some lengthy algebra, we obtain that

$$[k]_{11} = \begin{bmatrix} \frac{EA}{l}\,, & 0\,, & 0 \\ 0\,, & \frac{12EI}{l^3}\Phi_1\,, & \frac{6EI}{l^2}\Phi_2 \\ 0\,, & \frac{6EI}{l^2}\Phi_2\,, & \frac{4EI}{l}\Phi_3 \end{bmatrix}, \qquad [k]_{12} = \begin{bmatrix} -\frac{EA}{l}\,, & 0\,, & 0 \\ 0\,, & -\frac{12EI}{l^3}\Phi_1\,, & \frac{6EI}{l^2}\Phi_2 \\ 0\,, & -\frac{6EI}{l^2}\Phi_2\,, & \frac{2EI}{l}\Phi_4 \end{bmatrix},$$

$$[k]_{21} = \begin{bmatrix} -\frac{EA}{l}\,, & 0\,, & 0 \\ 0\,, & -\frac{12EI}{l^3}\Phi_1\,, & -\frac{6EI}{l^2}\Phi_2 \\ 0\,, & \frac{6EI}{l^2}\Phi_2\,, & \frac{2EI}{l}\Phi_4 \end{bmatrix}, \quad [k]_{22} = \begin{bmatrix} \frac{EA}{l}\,, & 0\,, & 0 \\ 0\,, & \frac{12EI}{l^3}\Phi_1\,, & -\frac{6EI}{l^2}\Phi_2 \\ 0\,, & -\frac{6EI}{l^2}\Phi_2\,, & \frac{4EI}{l}\Phi_3 \end{bmatrix}, \tag{2.3.10}$$

Where Φ_i are the influence functions depending only on $\zeta = l\sqrt{\lambda/EI}$ given by the following expression :

$$\begin{aligned} \Phi_1(\zeta) &= \frac{\zeta^3}{12}\frac{\sin\zeta}{2(1-\cos\zeta)-\zeta\sin\zeta}\,, \quad \Phi_2(\zeta) = \frac{\zeta^2}{6}\frac{1-\cos\zeta}{2(1-\cos\zeta)-\zeta\sin\zeta}\,, \\ \Phi_3(\zeta) &= \frac{\zeta}{4}\frac{\sin\zeta-\zeta\cos\zeta}{2(1-\cos\zeta)-\zeta\sin\zeta}\,, \quad \Phi_4(\zeta) = \frac{\zeta}{2}\frac{\zeta-\sin\zeta}{2(1-\cos\zeta)-\zeta\sin\zeta}\,, \end{aligned} \tag{2.3.11}$$

2.3.2 Assembling of the global matrix

Using the stiffness matrix of a single beam, we can assemble the global matrix of the unit cell shown in Figure 2.2. Let's consider a beam linking the points i and j and having a direction forming an angle ψ with the x axis. First we define a rotation matrix:

$$[Q] = \begin{bmatrix} cos(\psi) & -sin(\psi) & 0 \\ sin(\psi) & cos(\psi) & 0 \\ 0 & 0 & 1 \end{bmatrix}$$

We decompose $[U] = [u_1, v_1, \theta_1, ..., u_8, v_8, \theta_8]^T$ with sub-matrices $[U_i] = [u_i, v_i, \theta_i]^T$, and similarly we decompose the global stiffness matrix $[K] = [[K_{i,j}]]$ where $[K_{i,j}]$ is

a 3×3 matrix. Then the only non 0 sub-matrices of [K] linked to this (ij) beam are the following :

$$\begin{aligned} &[K_{ii}] = [Q].[k_{11}].[Q]^T, \quad [K_{ij}] = [Q].[k_{12}].[Q]^T, \\ &[K_{ij}] = [Q].[k_{21}].[Q]^T, \quad [K_{jj}] = [Q].[k_{22}].[Q]^T, \end{aligned} \tag{2.3.12}$$

Applying this method to all d.o.f, we provide the non 0 sub-matrices of the upper right half of [K]. The sub matrices of the lower left half can be obtained by symmetry.

$$[K_{11}] = \begin{bmatrix} \frac{96E_vI_v}{l_v^3} & 0 & -\frac{24E_vI_v}{l_v^2} \\ 0 & \frac{2E_vA_v}{l_v} & 0 \\ -\frac{24E_vI_v}{l_v^2} & 0 & \frac{8E_vI_v}{l_v} \end{bmatrix}, \quad [K_{18}] = \begin{bmatrix} -\frac{96E_vI_v}{l_v^3} & 0 & -\frac{24E_vI_v}{l_v^2} \\ 0 & -\frac{2E_vA_v}{l_v} & 0 \\ \frac{24E_vI_v}{l_v^2} & 0 & \frac{4E_vI_v}{l_v} \end{bmatrix}$$

$$[K_{22}] = \begin{bmatrix} \frac{2E_hA_h}{l_h} & 0 & 0 \\ 0 & \frac{96E_hI_h}{l_h^3} & \frac{24E_hI_h}{l_h^2} \\ 0 & \frac{24E_hI_h}{l_h^2} & \frac{8E_hI_h}{l_h} \end{bmatrix}, \quad [K_{28}] = \begin{bmatrix} -\frac{2E_hA_h}{l_h} & 0 & 0 \\ 0 & -\frac{96E_hI_h}{l_h^3} & \frac{24E_hI_h}{l_h^2} \\ 0 & -\frac{24E_hI_h}{l_h^2} & \frac{4E_hI_h}{l_h} \end{bmatrix}$$

$$[K_{33}] = \begin{bmatrix} \frac{2E_hA_h}{l_h} & 0 & 0 \\ 0 & \frac{96E_hI_h}{l_h^3} & \frac{24E_hI_h}{l_h^2} \\ 0 & \frac{24E_hI_h}{l_h^2} & \frac{8E_hI_h}{l_h} \end{bmatrix}, \quad [K_{37}] = \begin{bmatrix} -\frac{2E_hA_h}{l_h} & 0 & 0 \\ 0 & -\frac{96E_hI_h}{l_h^3} & \frac{24E_hI_h}{l_h^2} \\ 0 & -\frac{24E_hI_h}{l_h^2} & \frac{4E_hI_h}{l_h} \end{bmatrix}$$

$$[K_{44}] = \begin{bmatrix} \frac{96E_vI_v}{l_v^3} & 0 & \frac{24E_vI_v}{l_v^2} \\ 0 & \frac{2E_vA_v}{l_v} & 0 \\ \frac{24E_vI_v}{l_v^2} & 0 & \frac{8E_vI_v}{l_v} \end{bmatrix}, \quad [K_{47}] = \begin{bmatrix} -\frac{96E_vI_v}{l_v^3} & 0 & \frac{24E_vI_v}{l_v^2} \\ 0 & -\frac{2E_vA_v}{l_v} & 0 \\ -\frac{24E_vI_v}{l_v^2} & 0 & \frac{4E_vI_v}{l_v} \end{bmatrix}$$

$$[K_{55}] = \begin{bmatrix} \frac{2E_hA_h}{l_h} & 0 & 0 \\ 0 & \frac{96E_hI_h}{l_h^3} & -\frac{24E_hI_h}{l_h^2} \\ 0 & -\frac{24E_hI_h}{l_h^2} & \frac{8E_hI_h}{l_h} \end{bmatrix}, \quad [K_{58}] = \begin{bmatrix} -\frac{2E_hA_h}{l_h} & 0 & 0 \\ 0 & -\frac{96E_hI_h}{l_h^3} & -\frac{24E_hI_h}{l_h^2} \\ 0 & \frac{24E_hI_h}{l_h^2} & \frac{4E_hI_h}{l_h} \end{bmatrix}$$

$$[K_{66}] = \begin{bmatrix} \frac{2E_hA_h}{l_h} & 0 & 0 \\ 0 & \frac{96E_hI_h}{l_h^3} & -\frac{24E_hI_h}{l_h^2} \\ 0 & -\frac{24E_hI_h}{l_h^2} & \frac{8E_hI_h}{l_h} \end{bmatrix}, \quad [K_{67}] = \begin{bmatrix} -\frac{2E_hA_h}{l_h} & 0 & 0 \\ 0 & -\frac{96E_hI_h}{l_h^3} & -\frac{24E_hI_h}{l_h^2} \\ 0 & \frac{24E_hI_h}{l_h^2} & \frac{4E_hI_h}{l_h} \end{bmatrix}$$

$$[K_{77}] = \begin{bmatrix} \frac{4E_hA_h}{l_h} + \frac{12E_vI_v\Phi_1(\zeta)}{l_v^3} + \frac{96E_vI_v}{l_v^3} & 0 & \frac{6E_vI_v\Phi_2(\zeta)}{l_v^2} - \frac{24E_vI_v}{l_v^2} \\ 0 & \frac{3E_vA_v}{h} + \frac{192E_hI_h}{l^3} & 0 \\ \frac{6E_vI_v\Phi_2(\zeta)}{l_v^2} - \frac{24E_vI_v}{l_v^2} & 0 & \frac{16E_hI_h}{l_h} + \frac{4E_vI_v\Phi_3(\zeta)}{l_v} + \frac{8E_vI_v}{l_v} \end{bmatrix}$$

$$[K_{78}] = \begin{bmatrix} -\frac{12E_vI_v\Phi_1(\zeta)}{l_v^3} & 0 & \frac{6E_vI_v\Phi_2(\zeta)}{l_v^2} \\ 0 & -\frac{E_vA_v}{l_v} & 0 \\ -\frac{6E_vI_v\Phi_2(\zeta)}{l_v^2} & 0 & \frac{2E_vI_v\Phi_4(\zeta)}{l_v} \end{bmatrix}$$

$$[K_{88}] = \begin{bmatrix} \frac{4E_hA_h}{l_h} + \frac{12E_vI_v\Phi_1(\zeta)}{l_v^3} + \frac{96E_vI_v}{l_v^3} & 0 & \frac{24E_vI_v}{l_v^2} - \frac{6E_vI_v\Phi_2(\zeta)}{l_v^2} \\ 0 & \frac{3E_vA_v}{l_v} + \frac{192E_hI_h}{l^3} & 0 \\ \frac{24E_vI_v}{hl_v^2} - \frac{6E_vI_v\Phi_2(\zeta)}{l_v^2} & 0 & \frac{16E_hI_h}{l_h} + \frac{4E_vI_v\Phi_3(\zeta)}{l_v} + \frac{8E_vI_v}{l_v} \end{bmatrix}$$

2.3.3 Boundary conditions

To study the stability of the full system, one may at first think of using periodic boundary conditions on the unit cell, witch would give the following constraints over the d.o.f :

$$\begin{cases} u_1 = u_4,\ v_1 = v_4,\ \theta_1 = \theta_4, \\ u_2 = u_5,\ v_2 = v_5,\ \theta_2 = \theta_5, \\ u_3 = u_6,\ v_3 = v_6,\ \theta_3 = \theta_6, \end{cases} \tag{2.3.13}$$

However this method would fail to detect potential instability modes whose wavelength does not divide the unit cell size. And thus it risks overestimating the critical load. To study the stability of a periodic system for general wavelength the classical approach is to use Bloch wave analysis as described in Triantafyllidis and Schnaidt (1993) for planar truss model. We provide a brief explanation of the method. It can be shown that for a periodic system with unit cell dimension $L_x \times L_y$, the first bifurcating mode $u|_1$ can be expressed as $u|_1(x,y) = e^{i(\omega_x x + \omega_y y)}\tilde{u}(x,y)$ where $\tilde{u}$ is periodic over the unit cell (ie $\forall p, q \in Z, \tilde{u}(x + pL_x, y + qL_y) = \tilde{u}(x,y)$) and where w_x and w_y are the pulsation of the bifurcation mode in the x and y direction. For our case, Bloch boundary conditions lead to the following constraints

$$\begin{cases} u_1 = e^{i\omega_y L_y} u_4, \ \theta_1 = e^{i\omega_y L_y}\theta_4, \\ v_2 = e^{i\omega_x L_x} v_5, \ \theta_2 = e^{i\omega_x L_x}\theta_5, \\ v_3 = e^{i\omega_x L_x} v_6, \ \theta_3 = e^{i\omega_x L_x}\theta_6, \end{cases} \tag{2.3.14}$$

The previous constraints relations can be rewritten as $[u_c] = [A][u_u]$, where u_c and u_u respectively correspond to the constrained and unconstrained d.o.f We define the matrix $P = \begin{bmatrix} [I_d] \\ [A] \end{bmatrix}$. Thus, we get that $[u] = \begin{bmatrix} [u_u] \\ [u_c] \end{bmatrix} = \begin{bmatrix} [I_d] \\ [A] \end{bmatrix} [u_u] = [P][u_u]$ Then, subdividing the stiffness matrix according to whether or not the d.o.f is constraint (and reordering if needs be), we can write it as

$$[K] = \begin{bmatrix} [K_{uu}] & [K_{uc}] \\ [K_{cu}] & [K_{cc}] \end{bmatrix}$$

Finally, solving $[K][U] = [F]$ under the constraints [P] is equivalent to solving the unconstrained system $[\hat{K}][u_u] = [P]^\dagger[K][P][u_u] = [P]^\dagger[F]$. Using all those relations we obtain a stiffness matrix of size 15×15, depending on the geometry of the system, the bending stiffness of each material, the pulsations ω_x and ω_y and the magnetic loading. In order to find the critical load and the critical buckling mode, we now want to scan for all $\omega_x \in [0, \pi/l_h/2]$ and $\omega_y \in [0, \pi/l_v/4]$ the lowest value of λ that make the reduced stiffness matrix to lose a rank. We do so numerically by selecting a small enough pulsation step and for each couple of ω_x and ω_y we progressively increase the determinant of the stiffness matrix for increasing values of λ.

2.4 Results

2.4.1 Simplified cases

In order to check our full results, we want to get the axial critical loads that would be obtained in a simpler but similar system. The full results have to provide a critical load that is lower than the ones obtained with stricter boundary conditions, and

Geometric configuration and first buckling mode (dashed)						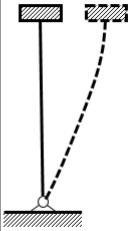
K value	0.5	≈ 0.699	1	1	2	2
$\zeta_c = \frac{\pi}{K}$	2π	≈ 4.4935	π	π	$\frac{\pi}{2}$	$\frac{\pi}{2}$
End condition key	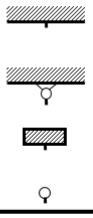	Rotation fixed and translation fixed Rotation free and translation fixed Rotation fixed and translation free Rotation free and translation free				

Figure 2.5: K and ζ_c values for various boundary conditions and related buckling modes for slender beams

higher than the ones obtained with looser boundary conditions. We first looked at what would be the critical load if we were only considering the (78) beam. The very common result of the slender beam under axial loading of length L and bending stiffness EI is that the critical axial load is $\lambda_{cr} = \frac{\pi^2 EI}{L^2 K^2}$, where K is a factor depending on the boundary conditions. It corresponds to $\zeta_c = \pi/K$. The most common values are given in Figure 2.5 and can be obtained purely analytically. We are not providing the derivation of those results, but the method simply is demonstrated in one slightly more complex case. We consider a single beam locked in translation with two fixed springs at the boundary i.e., a proportional relation between the moment and the angle at each extremity. The value of those springs is based on the rotation resistance due to the beams of the unit cell other than (78). Using the notation used when studying the single beam, the boundary conditions can be written as

$$\begin{cases} v(0) = v(L) = 0, \\ k\frac{\delta v}{\delta x}'(0) = -M(0) = EI\frac{\delta^2 v}{\delta x^2}(0), \\ k\frac{\delta v}{\delta x}'(L) = M(L) = -EI\frac{\delta^2 v}{\delta x^2}(L) \end{cases} \tag{2.4.1}$$

As we consider slender beams, the full problem in Equation 2.3.4 in Equation 2.3.5 reduces to

$$EI\frac{d^4 v}{dx^4}(x) + \lambda\frac{d^2 v}{dx^2}(x) = 0 \tag{2.4.2}$$

Still assuming a compressive load ($\lambda \geq 0$), and using $\mu = \sqrt{\frac{\lambda}{EI}}$, we get the following solutions :

$$v(x) = C_1 sin(\mu x) + C_2 cos(\mu x) + C_3 \mu x + C_4 \tag{2.4.3}$$

Solving the stability problem using boundary conditions Equation 2.4.2 we obtain the following values and conditions for C_i

$$\begin{cases} C_4 = -C_1 \\ C_3 = \dfrac{-C_2 \sin[\zeta] - C_1 \cos[\zeta] + C_1}{L}; \\ C_1 = C_2 \dfrac{\sin[\zeta] - \zeta}{\frac{\zeta^2 EI}{kL} + 1 - \cos[\zeta]}; \\ C_2(EI\zeta L \cos[\zeta/2] + K \sin[\zeta/2])(-K\zeta \cos[(\zeta)/2] + (2K + EI\zeta^2/L) \sin[(\zeta)/2]) = 0 \end{cases} \tag{2.4.4}$$

As a consequence, the first non trivial solution is obtained that the critical load is obtained by finding the lowest value of ζ such that

$$(EI\zeta L \cos[\zeta/2] + K \sin[\zeta/2])(-K\zeta \cos[(\zeta)/2] + (2K + EI\zeta^2/L) \sin[(\zeta)/2]) = 0 \tag{2.4.5}$$

As a sanity check, we check that for $k = 0$ and $k \to$ inf we get the results corresponding to Figure 2.5. If $k = 0$, the relation becomes $Sin[\zeta] = 0$ which is true for $\zeta = \pi$ or equivalently $K = 1$ as expected. If $k \to \infty$, the relation becomes :

$$\begin{aligned} &(2 \sin[\zeta/2]^2 - \zeta \sin[\zeta/2] \cos[\zeta/2]) = 0 \\ &\sin[\zeta/2] = 0 \ or \ \sin[\zeta/2] = \zeta/2 \cos[\zeta/2] \\ &\zeta = 2\pi \ or \ \zeta \approx 9 \end{aligned}$$

Thus the critical load is $\zeta_c = 2\pi$ which corresponds to $K = 1/2$ as expected. Using the notation of the unit cell, the relation becomes

$$\zeta(2k^2 l_v^2 - 2kl_v(\zeta^2 E_v I_v + kl_v) \cos[\zeta] + \zeta(\zeta^2 E_v I_v^2 + kl_v(2E_v I_v - kl_v)) \sin[\zeta]) = 0 \tag{2.4.6}$$

The value of those spring $k = \frac{M}{\theta}$ being obtained thanks to the initial global stiffness matrix and is $k = \frac{16E_h I_h}{l_h} + \frac{4E_v I_v \Phi_3(\zeta)}{l_v} + \frac{8E_v I_v}{l_v}$. As it cannot be solved analytically, we will illustrate it with the usual test case (1.5 mm radius metal horizontal beam, 0.75mm radius vertical plastic beam, 5cm $\times$ 5 cm cell). We obtain a critical load extremely close to $\zeta_c = 2\pi$, which correspond to $\lambda_c = (\frac{\zeta_c}{L})^2 EI$ or $K = 1/2$. It is expected as the horizontal beam is far stiffer than the vertical one, so the results are very close to the case where the horizontal beam is rigid. As the difference in bending stiffness is extreme, we are very close to the $K \to \infty$ case. Thus the size of the cell has very little impact on the result (at least for l_h, $l_v \in \{1cm, 10cm\}$.

It must be pointed out that this limited impact is due the fact that we are using ζ that is adimensionned. Given the definition of $\zeta = l_v\sqrt{(\lambda/(EI))}$, l_v will have a very significant impact on the critical axial load λ_c). Obviously the critical axial force changes with the geometry. A more general study of that effect can be found in Wang et al. (2014). All those results are obtained focusing on the beam (78). To get closer to the periodic cell we should take into account the other vertical beams. In this situation they would act as a doubling of the bending stiffness of the central beam, leading to a multiplication of the critical load ζ_c by $\sqrt{2}$ Finally, as an even more precise estimation, we can consider the full periodic system ($\omega_x = \omega_y = 0$). In this configuration, solving the reduced stiffness matrix, we obtain the lowest eigenvalues depending on ζ shown in Figure 2.6 for the same test case. As there are rigid body modes, we eliminate them by fixing $u_7 = v_7 = 0$. Similarly to the spring case, the geometry has little impact on the critical $\zeta_c = 4.41$. The critical mode has the following shape :

$$[u_1, 0, -\theta_1, u_2, 0, \theta_2, 0, 0, \theta_3, u_1, 0, -\theta_1, u_2, 0, \theta_2, 0, 0, \theta_3, 0, 0, \theta_7, u_8, 0, \theta_8]$$

All u_i, v_i, θ_i are taken positive. This mode is depicted in Figure 2.7. Fixing a point different from 7 will lead to the same eigenmode short of a horizontal and vertical translation. By neglecting the smallest terms of the eigenmode, we get that the solution is is very close to :

$$[u_1, 0, -\theta_1, 2u_1, 0, 0, 0, 0, 0, u_1, 0, -\theta_1, 2u_1, 0, 0, 0, 0, 0, 0, 0, 0, 2u_1, 0, 0]$$

It corresponds to the third case in Figure 2.5. Once again, as the bending stiffness of the horizontal beams dwarf the one of the vertical one, the results obtained are very close to those we would obtain if horizontal beam were infinity rigid, ie would be similar to the third case shown in Figure 2.5, but with double the axial stiffness. It would lead to a value of $\zeta_c = \sqrt{2}\pi = 4.44$. With our very rigid but not infinitely rigid beams, we get a critical load slightly inferior. Similarly to the previous case, as long as we keep the same order of magnitude in the length, l_v and l_h will have little impact on ζ_c.

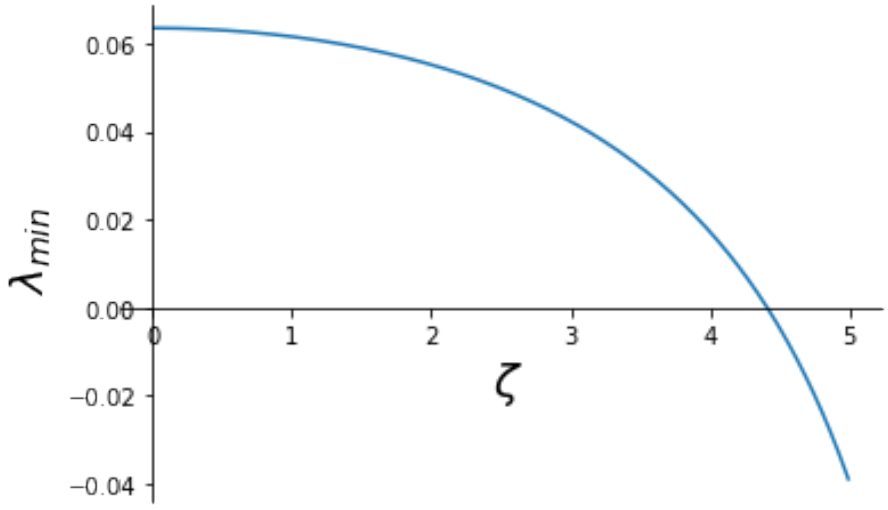

Figure 2.6: lowest eigenvalue (except rigid body) of the reduced stiffness matrix under periodic boundary conditions depending on the loading ζ

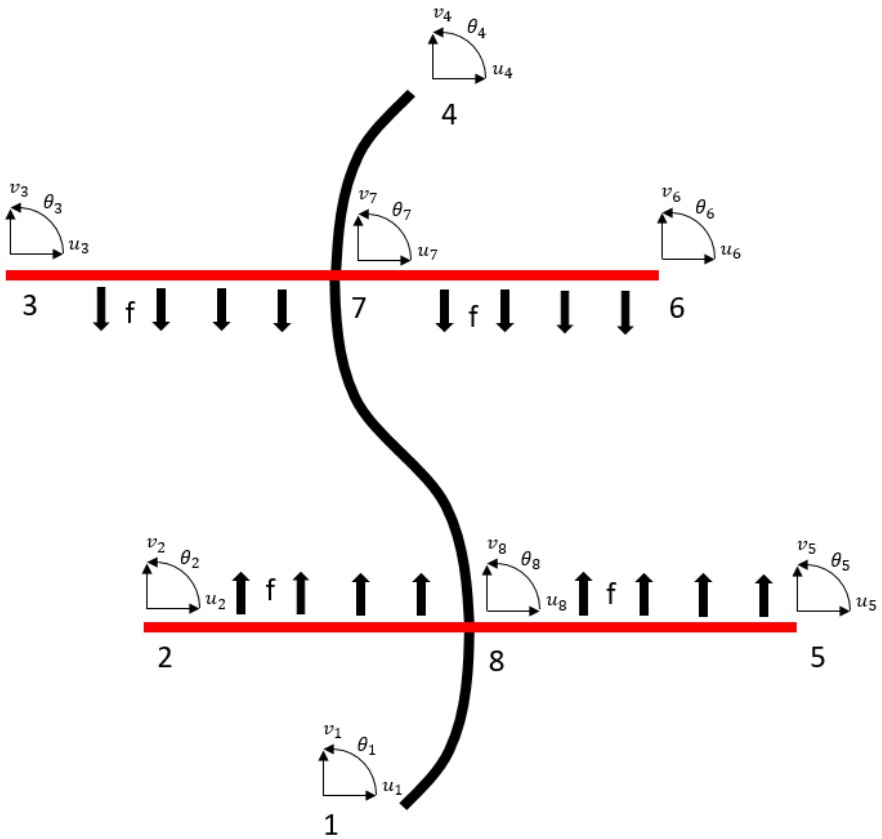

Figure 2.7: schematic of the critical mode for periodic boundary conditions

2.4.2 Complete case : Bloch analysis

We now consider the full problem with Bloch boundary conditions for the previously mentioned geometry : $l_v, l_h \in \{1cm, 10cm\}$, $r_h = 1.5mm$, $r_v = 0.75mm$, $E_h =$ 210GPa and $E_v =$ 2GPa. For a given ω_x and ω_y, the lowest value of ζ that leads to a significantly negative eigenvalue is called ζ_m. We computed the value of ζ_m for various $\omega_x \in [0, 2\pi/L_x]$ and $\omega_y \in [0, 2\pi/L_y]$. The lowest value of ζ_m is the critical load ζ_c The determinant of K$(\lambda, \omega_x, \omega_y)$ is symmetric in ω_x and ω_y, i.e. $det(K(\lambda, \omega_x, \omega_y)) = det(K(\lambda, -\omega_x, \omega_y)) = det(K(\lambda, \omega_x, -\omega_y)) = det(K(\lambda, -\omega_x, -\omega_y))$. Thus, we can reduce the range of pulsation to test to $\omega_x \in [0, \pi/L_x]$ and $\omega_y \in [0, \pi/L_y]$. This symmetry is shown in Figure 2.8 in the $l_v = l_h = 3cm$ case. In the following discussion, we will only plot one quarter of of the full plot. We use the reduced pulsations $\omega_x l_x$ and $\omega_y l_y$. Those results tend to indicate that the lowest modes are located for very low values of ω_x. To get a clear picture of what happens at low ω_x, we provide in Figure 2.9 the same plot but zoomed in term of ω_x as for any superior value of ω_x superior to those shown, the results will be higher and thus more stable. First, we observe that when ω_x and ω_y get close to 0, we obtain the

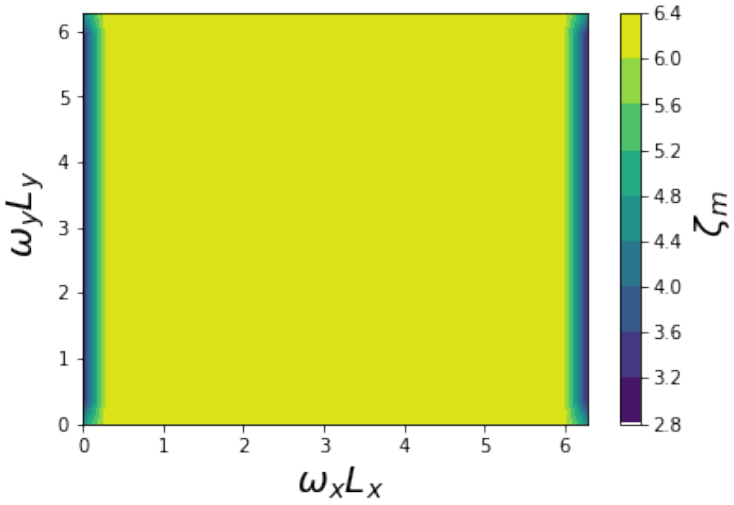

Figure 2.8: $\zeta_m(\omega_x, \omega_y)$ using bloch boundary conditions for $l_v = l_h = 3cm$, $r_h =$ $1.5mm$, $r_v = 0.75mm$, $E_h =$ 210GPa and $E_v =$ 2GPa. The full range of pulsation are $\omega_{x,red} = \omega_x L_x \in [0, 2\pi]$ and $\omega_{y,red} = \omega_y L_y \in [0, 2\pi]$

periodic results as expected. The most unstable mode ($\zeta_c = 3.12$) is achieved for $\omega_x = 0$ and $\omega_y = \pi/L_y$. The results are especially dependent on ω_x, which is due to the very high relative stiffness of the horizontal beam : imposing deformation in them is very costly in terms of energy. Once ω_x is significant, we lowest mode requires to keep at 0 the displacement and rotation for the horizontal beams which leads to the first case depicted in Figure 2.5, where rotation and translation at the ends of the central beam (78) are fixed at 0 and thus the first critical mode is obtained at

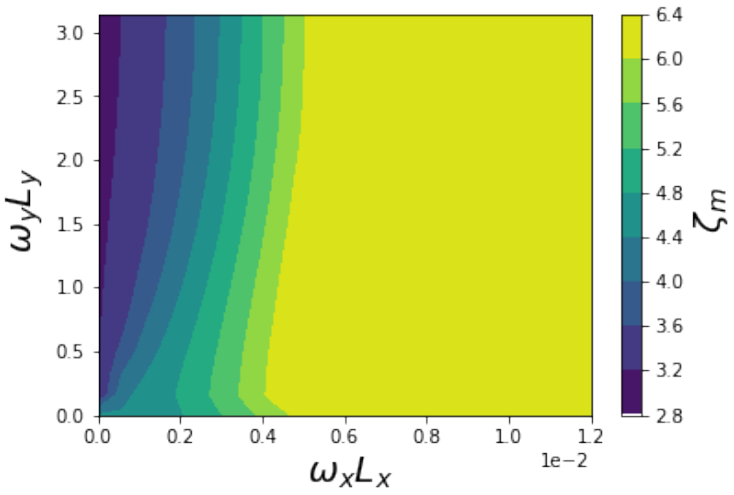

Figure 2.9: $\zeta_m(\omega_x, \omega_y)$ using bloch boundary conditions for $l_v = l_h = 3cm$, $r_h = 1.5mm$, $r_v = 0.75mm$, $E_h = 210$GPa and $E_v = 2$GPa. The full range of pulsation are$\omega_{x,red} = \omega_x L_x \in [0, 0.012]$ and $\omega_{y,red} = \omega_y L_y \in [0, \pi]$

$\zeta_m = 2\pi$. Contrary to ω_x, the system is less sensitive to a small variation in ω_y. Similar analysis for other values of l_v and l_h have been carried out and are shown in Figure 2.10. The main takeaway is that the minimal and maximal values of ζ_m stay very close to the previous case, once again as the difference in bending stiffness is massive, small variations of it will have little impact on the resulting critical mode. The main difference is observed on the impact of low ω_x, geometries that reduce the impact of the horizontal beam's bending stiffness are a bit more tolerant to ω_x in term of adimentionned pulsation $\omega_{x,red} = \omega_x L_x$, but less tolerant in terms of absolute ω_x.

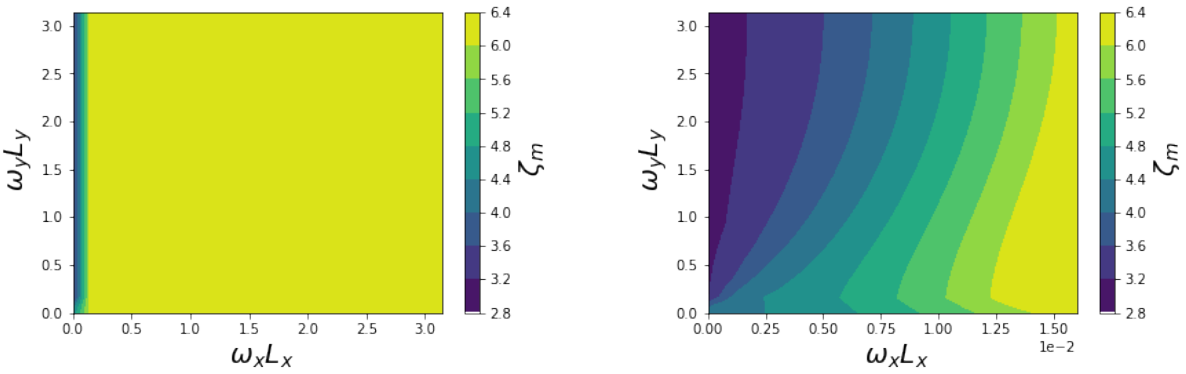

(a) $l_v = 1cm$ vs $l_h = 1cm$, $\omega_{x,red} = \omega_x L_x \in [0, \pi]$ and $\omega_{y,red} = \omega_y L_y \in [0, \pi]$

(b) $l_v = 1cm$ vs $l_h = 1cm$, $\omega_{x,red} = \omega_x L_x \in [0, 0.016]$ and $\omega_{y,red} = \omega_y L_y \in [0, \pi]$

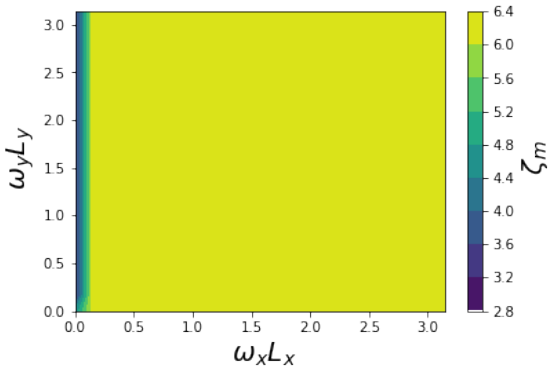

(c) $l_v = 10cm$ vs $l_h = 1cm$, $\omega_{x,red} = \omega_x L_x \in [0, \pi]$ and $\omega_{y,red} = \omega_y L_y \in [0, \pi]$

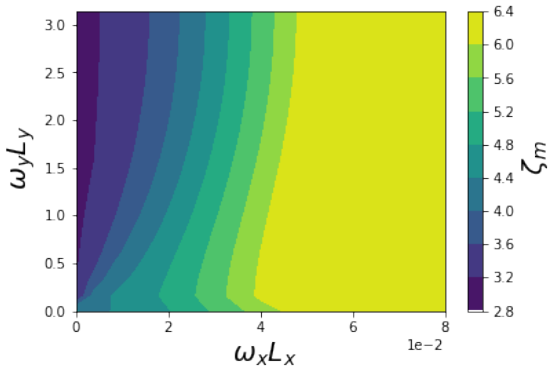

(d) $l_v = 10cm$ vs $l_h = 1cm$, $\omega_{x,red} = \omega_x L_x \in [0, 0.08]$ and $\omega_{y,red} = \omega_y L_y \in [0, \pi]$

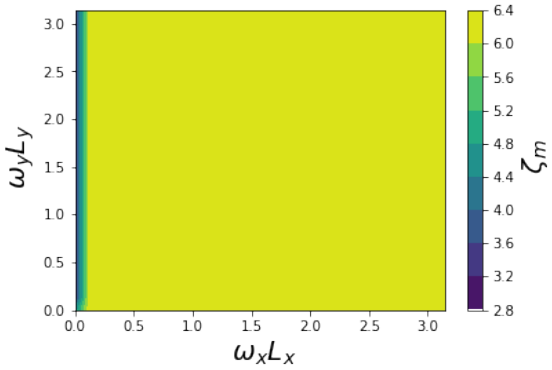

(e) $l_v = 1cm$ vs $l_h = 10cm$, $\omega_{x,red} = \omega_x L_x \in [0, \pi]$ and $\omega_{y,red} = \omega_y L_y \in [0, \pi]$

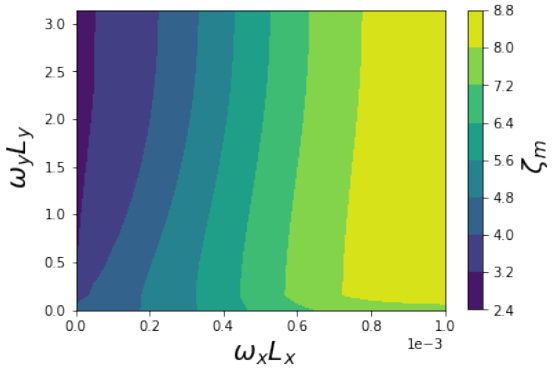

(f) $l_v = 1cm$ vs $l_h = 10cm$, $\omega_{x,red} = \omega_x L_x \in [0, 0.001]$ and $\omega_{y,red} = \omega_y L_y \in [0, \pi]$

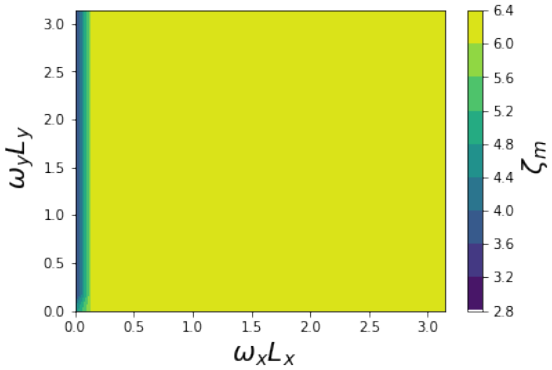

(g) $l_v = 10cm$ vs $l_h = 10cm$, $\omega_{x,red} = \omega_x L_x \in [0, \pi]$ and $\omega_{y,red} = \omega_y L_y \in [0, \pi]$

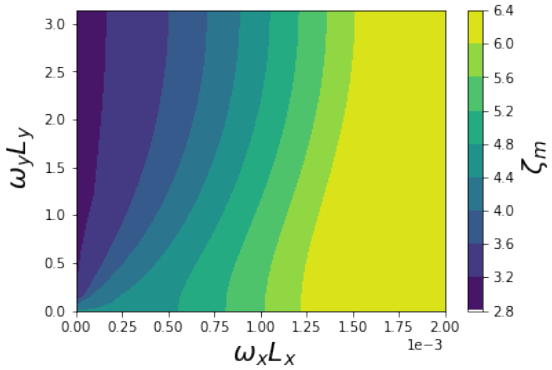

(h) $l_v = 10cm$ vs $l_h = 10cm$, $\omega_{x,red} = \omega_x L_x \in [0, 0.002]$ and $\omega_{y,red} = \omega_y L_y \in [0, \pi]$

Figure 2.10: critical load ζ for various values of l_h and l_v and $r_h = 1.5mm$, $r_v = 0.75mm$, $E_h = 210$GPa and $E_v = 2$GPa.

The value of the critical load stays very close to the global minimum for a significant range of ω_y. The critical mode will vary depending on geometry and pulsation, but we can generalise some properties. All critical modes keep deformation in the rigid beams minimal with significant horizontal displacement. However the relative displacement of those horizontal beams varies depending on ω_y. The vertical beams are under large rotation. We obtain modes similar to the periodic mode depicted in Figure 2.7 but the relaxation of the vertical periodic boundary condition lowers ζ_c and the horizontal displacement of the horizontal beams no longer are opposite relative to the centre of the vertical beams. It can be easily understood in the $w1 = 0$ case, the periodic case imposes that the loading in one beam buckles two equivalent vertical beams with the same displacement, which is equivalent to one single beam with double the bending stiffness. However if the displacement of the beams (18) and (74) can be different, there is no extra stiffness and we get back to a single beam, which according to Figure 2.5 has a critical load of $\zeta_c = \pi$. We get a slightly lower value ($\zeta_c = 3.12$) as our horizontal beams are not perfectly rigid. This value is not impacted by geometry as long as the horizontal bending stiffness stays very high compared to the vertical one. The eigenmode for $\omega_x = 0$ and $\omega_y = \pi/L_y$ is displayed in Figure 2.11

2.4.3 Beams of identical stiffness

It is important to highlight that previously discussed behavior is heavily influenced by the assumption that horizontal beams are significantly stiffer that the vertical ones. To show the extent of this influence, we provide in Figure 2.12 the results for bloch stability, but considering this time that the vertical beam have the same stiffness as the horizontal ones. Under that hypothesis, the values of ζ_c varies greatly, from as low as 1.414 when considering $l_h = 1cm$ and $l_v = 10cm$ to as high as 3.091 when considering $l_h = 10cm$ and $l_v = 1cm$. The dependency in ω_y is also greatly affected $\omega_y = \pi/L_y$ no longer being the critical mode in several cases. However $\omega_x \neq 0$ is still strongly penalysed.

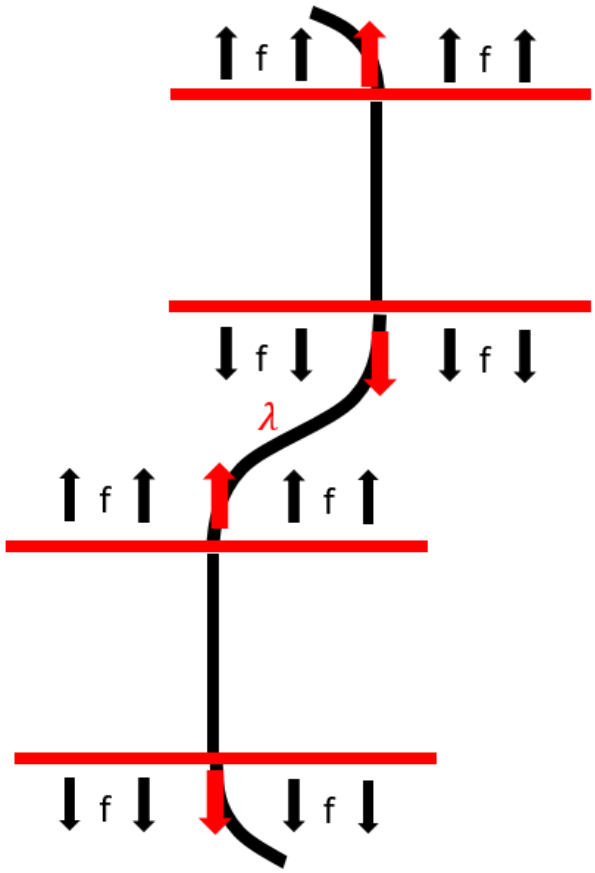

Figure 2.11: schematic of the critical mode for bloch boundary conditions, $\omega_x = 0$ and $\omega_y = \pi/L_y$

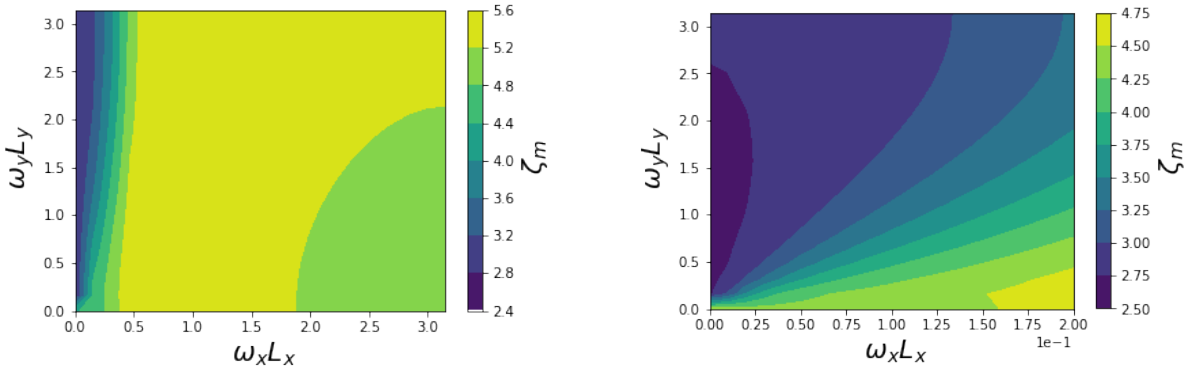

(a) $l_v = 1cm$ vs $l_h = 1cm$, $\omega_{x,red} = \omega_x L_x \in [0, \pi]$ and $\omega_{y,red} = \omega_y L_y \in [0, \pi]$

(b) $l_v = 1cm$ vs $l_h = 1cm$, $\omega_{x,red} = \omega_x L_x \in [0, 0.2]$ and $\omega_{y,red} = \omega_y L_y \in [0, \pi]$

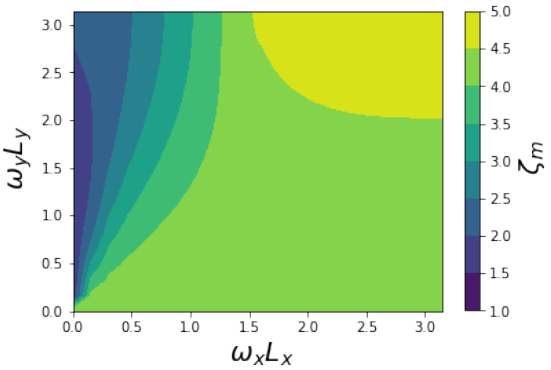

(c) $l_v = 10cm$ vs $l_h = 1cm$, $\omega_{x,red} = \omega_x L_x \in [0, \pi]$ and $\omega_{y,red} = \omega_y L_y \in [0, \pi]$

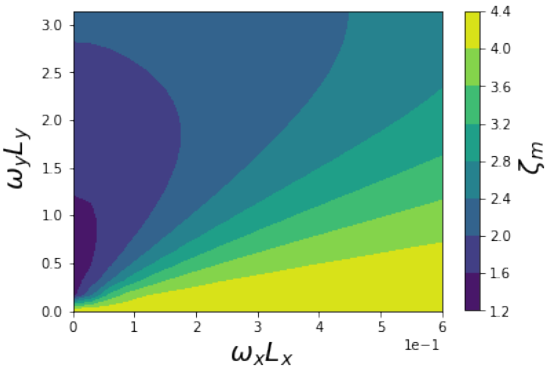

(d) $l_v = 10cm$ vs $l_h = 1cm$, $\omega_{x,red} = \omega_x L_x \in [0, 0.6]$ and $\omega_{y,red} = \omega_y L_y \in [0, \pi]$

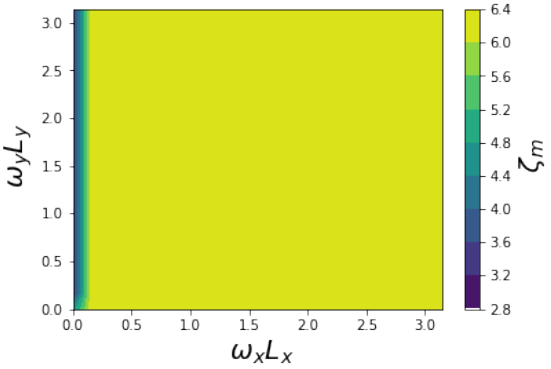

(e) $l_v = 1cm$ vs $l_h = 10cm$, $\omega_{x,red} = \omega_x L_x \in [0, \pi]$ and $\omega_{y,red} = \omega_y L_y \in [0, \pi]$

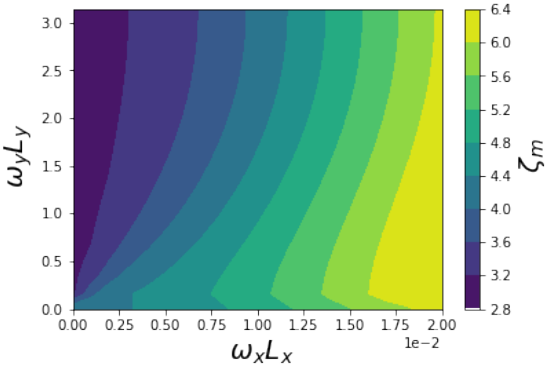

(f) $l_v = 1cm$ vs $l_h = 10cm$, $\omega_{x,red} = \omega_x L_x \in [0, 0.02]$ and $\omega_{y,red} = \omega_y L_y \in [0, \pi]$

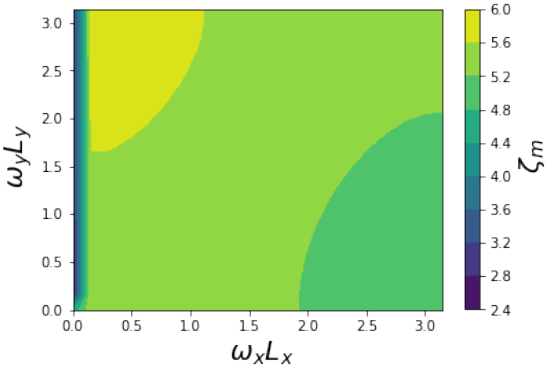

(g) $l_v = 10cm$ vs $l_h = 10cm$, $\omega_{x,red} = \omega_x L_x \in [0, \pi]$ and $\omega_{y,red} = \omega_y L_y \in [0, \pi]$

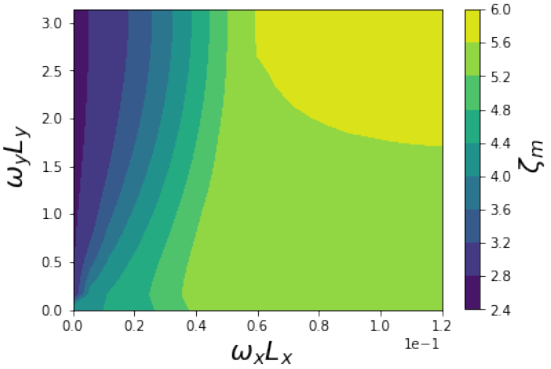

(h) $l_v = 10cm$ vs $l_h = 10cm$, $\omega_{x,red} = \omega_x L_x \in [0, 0.12]$ and $\omega_{y,red} = \omega_y L_y \in [0, \pi]$

Figure 2.12: critical load ζ for various values of l_h and l_v and $r_h = r_v = 1.5mm$ and $E_h = E_v = 210\text{GPa}$

2.4.4 Required electromagnetic loading

Considering the case of weaker vertical beams, the lowest modes for the five geometries are reported in Table 2.1 with a precision of 10^{-3}. From them, material parameters and geometry, we compute the related axial forces, the force per unit of length in the conductors, and current required to achieve this force considering a magnetic field of 0.7T that our experimental setup can achieve. The main takeaway

test case	1	2	3	4	5
l_h (cm)	3	1	1	10	10
l_v (cm)	3	1	10	1	10
ζ_c	3,142	3,142	3,142	3,139	3,143
$\lambda_c(N)$	5,452	4,907 10^1	4,907 10^{-1}	4,897E+01	4,91010^{-1}
$f_c(N/m)$	1,817 10^2	4,907 10^3	4,907 10^1	4,897 10^2	4,910
$I_c(A)$	2,596 10^2	7,009 10^3	7,009 10^1	6,996 10^2	7,014
$\dot{\theta}$ (K/s)	1,377 10^2	1,004 10^5	1,004 10^1	9,999 10^2	1,005 10^{-1}

Table 2.1: Summary of critical load for various geometry and their related magnetic requirement

of those results is that it is not possible to make an experiment with our setup. The thermal and current limitation impose large cells, but the size of the zone in which we achieve a constant magnetic field is only 8*8 cm. As the generation of force is dependant on the "infiniteness" of the array, to obtain experimental results we would have a significant number of cells, which is incompatible with the other constraints

2.5 Conclusion

In this chapter we studied the mechanical behaviour of an infinite mesh of wires loaded vertically by the wires considered in the previous chapter. Using common methods, we determine that the deformations for the principal solution are small even when considering using plastic instead of metal for the vertical beams. The onset of buckling has been determined using Bloch theorem, and these results are consistent with those obtained with simplified models. The required values of critical electromagnetic load are not achievable in the experimental setup we considered. We made this analysis assuming that the buckling would have no long range compression (as usual using Bloch theorem). The interested reader could find ways to look for these types of modes in Elliott et al. (2006).

Chapter 3

2D layered composite with current sheets

In this Chapter we consider a different geometry, a 2D composite made of magnetizable conductive fibers and a non conductive matrix under an external magnetic field, currents, and mechanical loadings. This study tries to achieve two different objectives. First, we want to use the coupled model derived in Chapter 1 in a different context to see if we can obtain an interesting behaviour in a composite that is very stable to non axial loadings. The fiber reinforced composite under axial mechanical load has already been treated which will enable us to compare the results. Second, we planned to use this simple case to qualify a FE code that would enable us to study more complex geometries such as hexagonal honeycombs. That is why we are going to make some assumptions detailed latter enabling us to solve analytically this system. The FE code is currently being worked on, and applying this code to more complex geometries is left as a future expansion. The coupled magneto-mechanical theory has already been established in Chapter 1 along the required bibliography and we won't repeat it here. The fundamental ideas about stability analysis have been provided in Chapter 2, but we are going to precise them with results specific to this geometry. We focus on axial mechanical load, as this is the most used, the most unstable, and thus the most studied configuration. Literature separates two major categories of instabilities when it comes to such composite : microscopic instabilities (buckling of the fiber) and macroscopic buckling (loss of ellipticity of the homogenized incremental moduli). Several works such as Budiansky and Fleck (1993), Kyriakides et al. (1995), Vogler et al. (2001) found that buckling instability acted as an onset of instability and evolved into localized macroscopic deformation pattern (kinkband). While very interesting, we won't study that evolution and simply look at the onset of both instabilities separately. Similarly, we won't consider the impact of imperfection on the system. The interested reader could find some element about their impact in the purely mechanical case in Budiansky and Fleck (1993). To study the microscopic instabilities we will use the same tools presented in Chapter 2 i.e.

Bloch theorem. Several papers, such as Santisi d'Avila et al. (2016),Triantafyllidis and Maker (1985),and Geymonat et al. (1993) implement the Bloch theorem to study the local modes of 2D axially compressed composite. In this chapter we will adapt their work to the fully coupled magneto-mechanical case. When it comes to the global mode, as explained in Chapter 2, it has been shown that the long wavelength ($\omega \to 0$) corresponds to the homogenised loss of ellipticity. As homogenisation is popular when studying composite, and contrary to Chapter 2, we will use the homogenised moduli instead of small ω to study the global buckling. The presentation is organized as follows: The geometry studied is detailed in Section 3.1. Then, in Section 3.2 we applied the general equations derived in Chapter 1 to this particular case. It leads to the principal solution discussed in Section 3.3. Then the methods used to study the stability of the system are presented in Section 3.4. Finally, we present the results in Section 3.5. First we compare our purely mechanical results to those obtained from Triantafyllidis and Maker (1985), then we look at the impact of purely magnetic loading and prove that those loadings are not strong enough to create instability under reasonable conditions. Finally, we provide results with both magnetic and mechanical loadings. Before the conclusion, some explanations are provided about the planned FE expansion.

3.1 Problem description

The problem under consideration is shown in Figure 3.1. It is composed of alternating layers of soft non conductive non magnetizable matrix and strong current carrying magnetizable fibers stacked in the y direction. The constitutive laws for both mechanics and magnetization are non linear and will be detailed later. The system has translation invariances in the $\mathbf{e}_1$ and $\mathbf{e}_3$ directions and the currents in the wires are in the $\pm\mathbf{e}_1$ direction, with alternating sign between each fibers. We consider a plane strain hypothesis and thus a 2D problem in the $\mathbf{e}_1$ and $\mathbf{e}_2$ directions. Because of the translation symmetry in the $\mathbf{e}_1$ direction, except for the stability analysis, it is a 1D problem. The entire system is under an exterior magnetic field $\mathbf{b}_{ext} = b_{ext}\mathbf{e}_3$ (current configuration). As all magnetic quantities will be purely in $\mathbf{e}_3$, we will use the bold letters ($\mathbf{B}, \mathbf{b}, \mathbf{H}$, ...) for the vectors and the normal ones (B,b,H, ...) for the $\mathbf{e}_3$ component. The mechanical boundary conditions are an imposed strain in the horizontal direction λ_1 for all layers, and a vertical total stress σ_{ext22}. As seen in the Chapter 1, we expect the current to have a homogenous repartition in the conductor. However, as the analytical solving of the stability problem relies on having constant coefficients in each layers, we are going to adapt the setting. We are going to consider that the fiber is itself a composite of two current carrying layers of thickness 0 at the boundaries of the fiber, and a magnetizable material between them. Experimentally, it could be accomplished by separating the sub layers with non conductive glue. The end result is that the current is now modelled by current sheets between the matrix and the fiber of value $\boldsymbol{K} = \pm\kappa\boldsymbol{e}_3$. Using that model, we reduce the problem to a 2D

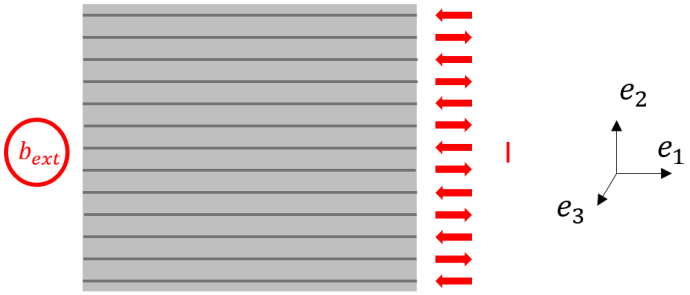

Figure 3.1: Schematic of the composite under consideration. The fibers are represented in dark grey, the matrix in light grey. The electromagnetic loading is composed of an external magnetic field b_{ext} and currents I

unit cell shown in Figure 3.2. The unit cell is composed of 4 layers:

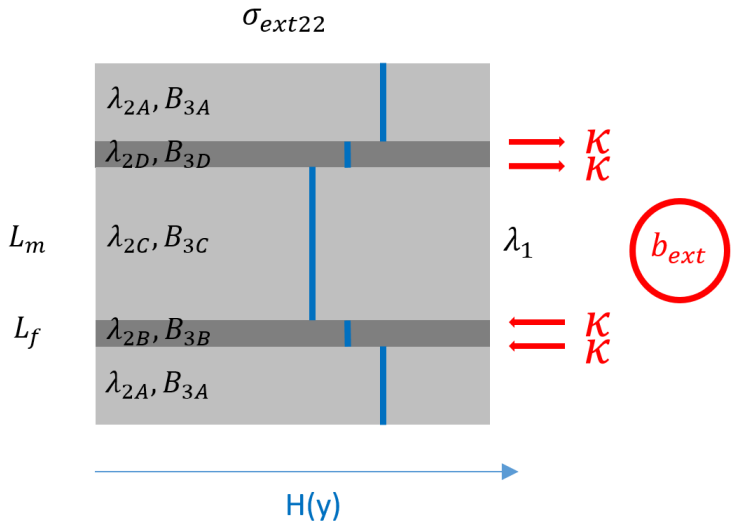

Figure 3.2: Schematic of the composite unit cell under consideration. The fibers are represented in dark grey, the matrix in light grey. The electromagnetic loading is composed of an external magnetic field b_{ext} and surface currents κ. The h-field in reference configuration is plotted in blue.

- layers A and C : soft non magnetizable non conductive material, the out of plane magnetic fields in reference configuration B_{3A} and B_{3C} and vertical strains λ_{2A} λ_{2C} are different if the current is non zero. Their thicknesses are $L_A = L_C =$

L_m. Their mechanical properties, detailed later, are named G_m and ν_m. The horizontal strains are λ_1. Their H fields in the reference configuration are H_A and H_C.

- layer B and D : magnetizable current carrying material, the out of plane magnetic fields B_{3B} and B_{3CD} and strains λ_{2B} λ_{2D} are identical. Their thicknesses are $H_B = H_D = H_f$. Their mechanical properties, detailed later, are named G_f and ν_f. The horizontal strains are λ_1. Their H fields in the reference configuration are H_B and H_D. Interface conditions will impose that $H_B = H_D$

3.2 Theory

3.2.1 Variational principle

We largely reuse the work done in Chapter 1, but we provide here the simplified version of those expressions using the fact that the displacements are in plane and the magnetic fields are out of plane and thus displacements are orthogonal to magnetic fields. Using the expression of the lagrangian density in Equation 1.2.1, the total lagrangian in Equation 1.2.2 and the potential energy Equation 1.3.1 provided in Chapter 1, we obtain the expression provided in Equation 3.2.1 for the potential energy in reference configuration P. W is the system total energy density and S the surface of the unit cell and ∂S the boundaries between layers. $\boldsymbol{J}$ is the current density vector and $\boldsymbol{K}$ is the surface current vector.

$$\begin{aligned} P &= \int_S W(\boldsymbol{A}, \boldsymbol{F}) dS - \int_{\partial S} \boldsymbol{K} \cdot \boldsymbol{A} dl \\ &= \int_S \Big[- \boldsymbol{A} \cdot \boldsymbol{J} + \frac{1}{2\xi} (\nabla \cdot \boldsymbol{A})^2 + \frac{J_1}{2\mu_0 I_2^{\frac{1}{2}}} + \rho_0 \psi_{el}(I_1, I_2) + \rho_0 \psi_m(J_1^*) \Big] dS - \int_{\partial S} \boldsymbol{K} \cdot \boldsymbol{A} dl \end{aligned} \tag{3.2.1}$$

We use the usual mechanical quantities, the 2D deformation gradient $\mathbf{F} = \mathbf{Id} + \nabla \mathbf{u}$ and the right Cauchy green tensor $\mathbf{C} = \mathbf{F}^T \cdot \mathbf{F}$. The magnetic potential is defined as $\mathbf{B} = \nabla \times \mathbf{A}$ The invariants used are :

$$\begin{cases} I_1 = tr(\mathbf{C}) \\ I_2 = \dfrac{1}{2}(tr(\mathbf{C})^2 - tr(\mathbf{C})) = det(C) \\ J_1 = B^2, \text{(we will also use } J_1^* = \dfrac{J_1}{I_2} \text{for convenience as explained later)} \end{cases}$$

However, contrary to Chapter 1, we have to take into account that the magnetic loading is imposed in current configuration. The simplest way to handle that is to split the magnetic field $\mathbf{B} = \tilde{\mathbf{B}} + det(\mathbf{F}) \mathbf{F}^{-1} \cdot \mathbf{b}_0$ between the magnetic perturbation

$\tilde{B}$ due to the effect of the materials (deformation, magnetization) and a magnetic loading term $det(\mathbf{F})\mathbf{F}^{-1}\cdot\mathbf{b}_0$ that takes into account the loading in current configuration. b_0 is the value of the magnetic field in the absence of material effect, so only considering b_{ext} and κ. Thus b_0 is constant in each layer, but not across layers. As the magnetic quantities and the mechanical ones are orthogonal, $\mathbf{F}^{-1}\cdot\boldsymbol{b_0} = \boldsymbol{b_0}$. The variables of the problem are the in plane displacement $\mathbf{u} = u_1\mathbf{e}_1 + u_2\mathbf{e}_2$ and the out of plane magnetisation perturbation in reference configuration $\tilde{\mathbf{B}}$. The magnetic potentials are defined as $\tilde{\mathbf{B}} = \nabla\times\tilde{\mathbf{A}}$, and $\mathbf{B} = \nabla\times\mathbf{A}$. As $\mathbf{A} = \mathbf{a}\cdot\mathbf{F}$ the magnetic potential in reference configuration is written as $\mathbf{A} = \tilde{\mathbf{A}} + \mathbf{a}_0\cdot\mathbf{F}$ Using the perturbed magnetic quantities, Equation 3.2.1 becomes Equation 3.2.2

$$
\begin{aligned}
P &= \int_S W(\tilde{\boldsymbol{A}}, \boldsymbol{F})dS - \int_{\partial S} \boldsymbol{K}\cdot\tilde{\boldsymbol{A}}dl - \int_{\partial S} \boldsymbol{K}\cdot(\boldsymbol{a_0}\cdot\boldsymbol{F})dl \\
&= \int_S \Big[-\boldsymbol{a_0}\cdot\boldsymbol{F}\cdot\boldsymbol{J}\underbrace{-\tilde{\boldsymbol{A}}\cdot\boldsymbol{J}}_{W_1} + \underbrace{\frac{1}{2\xi}(\nabla\cdot\tilde{\boldsymbol{A}})^2}_{W_2} + \underbrace{\frac{J_1}{2\mu_0 I_2^{\frac{1}{2}}}}_{W_3} + \underbrace{\rho_0\psi_{el}(I_1, I_2)}_{W_4} + \underbrace{\rho_0\psi_m(J_1^*)}_{W_5} \Big] dS \\
&- \int_{\partial S} \boldsymbol{K}\cdot\tilde{\boldsymbol{A}}dl - \int_{\partial S} \boldsymbol{K}\cdot(\boldsymbol{a_0}\cdot\boldsymbol{F})dl
\end{aligned}
\tag{3.2.2}
$$

About the two terms containing a_0, they have no dependence in $\tilde{A}$ so they won't appear in $P_{,\delta\tilde{\boldsymbol{A}}}$. As κ and J are constant, as the system is invariant by translation in the e_1 direction and as in this configuration and with coulomb gauge a_0 is purely in the e_1 direction, integration by part and straightforward algebra gives that when considering $P_{,\delta\tilde{u}}$, these terms become 0. For clarity, we split the remaining terms as shown in Equation 3.2.2 : W_1 is the current term, W_2 is a penalisation to impose coulomb gauge ($\nabla.\boldsymbol{A} = 0$), W_3 the maxwell energy in the vacuum, W_4 the elastic energy and W_5 the magnetisation energy of the material. W_1 is only relevant for the main solution and has no direct impact on stability. In addition we replaced current density by current sheet, so this term is 0. W_2 would be important when we solve in $\tilde{\boldsymbol{A}}$, but considering the orientations of the currents and magnetic fields, it is easier to solve directly in $\tilde{\boldsymbol{B}}$ as it has only one non 0 component. We set those terms to 0 in the following calculation. The complete expressions for each energy derivative is provided in Appendix A

3.2.2 Governing equation and interface conditions

In a similar manner to Chapter 1, we obtain the Governing equation and interface conditions by taking the first derivatives of Equation 3.2.2. The euler lagrange equa-

tion are :

$$
\begin{aligned}
P_{,\delta\tilde{A}} &= \int_S \Big[-\nabla\times\boldsymbol{H}\cdot\delta\tilde{A}\Big] dS + \int_{\partial S} (\boldsymbol{K} - \boldsymbol{N}\times[\![\boldsymbol{H}]\!])\cdot\boldsymbol{\delta}\tilde{\boldsymbol{A}} dl \\
P_{,\delta\boldsymbol{u}} &= \int_S \Big[(\nabla\cdot\boldsymbol{\Pi})\delta\boldsymbol{u}\Big] dS - \int_{\partial S} \Big(\boldsymbol{N}\cdot\Big[\!\Big[\Big(\frac{\partial W_i}{\partial \boldsymbol{F}}\Big)^T\Big]\!\Big]\Big)\cdot\delta\boldsymbol{u} dl
\end{aligned}
\tag{3.2.3}
$$

values for reference configuration h-field $\boldsymbol{H}$ and reference configuration stress $\boldsymbol{\Pi}$ by taking the first derivatives of Equation 3.2.2. Those values are provided in Equation 3.2.4, with the details of the derivative of each term being provided in Appendix A.

$$
\begin{aligned}
\boldsymbol{H} &= \sum_{i=3}^{5} \rho_0 \frac{\partial W_i}{\partial \tilde{\boldsymbol{B}}} = \frac{\tilde{\boldsymbol{B}} + det(\boldsymbol{F})b_0}{\mu_0 det(\mathbf{F})} + \rho_0 \frac{\partial \psi_m}{\partial \tilde{\boldsymbol{B}}} \\
\boldsymbol{\Pi} &= \Big(\sum_{i=3}^{5} \rho_0 \frac{\partial W_i}{\partial \boldsymbol{F}}\Big)^T
\end{aligned}
\tag{3.2.4}
$$

As the current density and mechanical body forces are 0, the governing equations are :

$$
\begin{aligned}
&\nabla\times\boldsymbol{H} = 0 \\
&\nabla\cdot\boldsymbol{B} = 0 \\
&\nabla\cdot\boldsymbol{\Pi} = 0
\end{aligned}
\tag{3.2.5}
$$

The interface conditions are :

$$
\begin{aligned}
&\boldsymbol{n}\times[\![\boldsymbol{H}]\!] = \boldsymbol{K} \\
&\boldsymbol{n}\cdot[\![\boldsymbol{B}]\!] = 0 \\
&\boldsymbol{n}\cdot[\![\boldsymbol{\Pi}]\!] = \boldsymbol{T} = 0
\end{aligned}
\tag{3.2.6}
$$

For $\alpha \in \{A, B, C, D\}$, $\mathbf{b}_{0\alpha}$ are the magnetic field in the absence of material effect. Thus we obtain immediately that :

$$
\begin{aligned}
&\mathbf{b}_{0B} = \mathbf{b}_{0D} = b_{ext}\mathbf{e}_3 \\
&\mathbf{b}_{0A} = (b_{ext} + \mu_0\kappa)\mathbf{e}_3 \\
&\mathbf{b}_{0D} = (b_{ext} - \mu_0\kappa)\mathbf{e}_3
\end{aligned}
\tag{3.2.7}
$$

Constitutive relations We will use the same constitutive relations as Chapter 1 with the same magnetic parameters ($\chi = 2.5\times10^3$ and $ms = 1.7\times10^6 Am^{-1}$). The expressions for the energy in reference configuration have been provided in Equation 1.2.23 and Equation 1.2.9. The magnetisation law depends on b^2 which corresponds to $J_1/I_2 = J_1^*$. That is why ψ_m is a function of J_1^* in W_5. We will use various parameters for the mechanical constitutive laws ranging from weak foam to steel.

3.3 Principal solution

First let's focus on the principal solution, that is by design constant in each layers. For a given λ_1, external magnetic field b_{ext} and surface current κ the eight unknowns are λ_{2A},λ_{2B},λ_{2C},λ_{2D},$\tilde{B_A}$,$\tilde{B_B}$,$\tilde{B_C}$,$\tilde{B_D}$. Those values are obtained by using the interface conditions Equation 3.2.6 which leads to:

$$\begin{aligned} &[\![H]\!] = \kappa \\ &[\![\Pi_{22}]\!] = 0 \end{aligned} \tag{3.3.1}$$

Where the expression of $\boldsymbol{H}$ and $\boldsymbol{\Pi}$ are given in Equation 3.2.4 Ir corresponds to 6 equations, as the interface conditions between layer A and layer D is a linear combination of the other interface conditions :

$$\begin{aligned} &H_B - H_A = \kappa \\ &H_C - H_B = \kappa \\ &H_D - H_B = -\kappa \\ &\Pi_{22B} - \Pi_{22A} = 0 \\ &\Pi_{22C} - \Pi_{22B} = 0 \\ &\Pi_{22D} - \Pi_{22C} = 0 \end{aligned} \tag{3.3.2}$$

We need two additional equations. One comes from the far field loading $\sigma_{22} = b_{ext}^2/(2\mu_0)$ (in current configuration) that correspond to maxwell stress in the vacuum considering the average of b_0, i.e. b_{ext}. In reference configuration we have $\Pi_{22} = J(\boldsymbol{F}^{-1}.\boldsymbol{\sigma})_{22} = \lambda_1\sigma_{22}$ (when considering the principal solution, we have that $\boldsymbol{F} = \lambda_1 e_1 e_1 + \lambda_2 e_2 e_2$). The second comes from magnetism. As the average current in the unit cell is 0, and as the divergence of the magnetic field is null, we have that the average of the perturbation (current configuration) of the magnetic field is 0, which leads to $\int_S b dS = \int_S b_0 dS$. A similar argument is used in Danas (2017). Even if the variable we are solving for are the $\tilde{B}_\alpha$, we will use B_α when it is possible to simplify notation. The system expressed with the layers values is :

$$H_B - H_A = \frac{B_B}{\mu_0\lambda_1\lambda_{2B}} + \frac{2B_B}{\lambda_1^2\lambda_{2B}^2}\frac{\partial\psi_m}{\partial J_1^*}\left(\frac{B_B^2}{\lambda_1^2\lambda_{2B}^2}\right) - \frac{B_A}{\mu_0\lambda_1\lambda_{2A}} - \frac{2B_A}{\lambda_1^2\lambda_{2A}^2}\frac{\partial\psi_m}{\partial J_1^*}\left(\frac{B_A^2}{\lambda_1^2\lambda_{2A}^2}\right) = \kappa$$

$$H_C - H_B = \frac{B_C}{\mu_0\lambda_1\lambda_{2C}} + \frac{2B_C}{\lambda_1^2\lambda_{2C}^2}\frac{\partial\psi_m}{\partial J_1^*}\Big(\frac{B_C^2}{\lambda_1^2\lambda_{2C}^2}\Big) - \frac{B_B}{\mu_0\lambda_1\lambda_{2B}} - \frac{2B_B}{\lambda_1^2\lambda_{2B}^2}\frac{\partial\psi_m}{\partial J_1^*}\Big(\frac{B_B^2}{\lambda_1^2\lambda_{2B}^2}\Big) = \kappa$$

$$H_D - H_C = \frac{B_D}{\mu_0\lambda_1\lambda_{2D}} + \frac{2B_D}{\lambda_1^2\lambda_{2D}^2}\frac{\partial\psi_m}{\partial J_1^*}\Big(\frac{B_D^2}{\lambda_1^2\lambda_{2D}^2}\Big) - \frac{B_C}{\mu_0\lambda_1\lambda_{2C}} - \frac{2B_C}{\lambda_1^2\lambda_{2C}^2}\frac{\partial\psi_m}{\partial J_1^*}\Big(\frac{B_C^2}{\lambda_1^2\lambda_{2C}^2}\Big) = -\kappa$$

$$\int_S b dS = \sum_{\alpha=A}^{D} b_\alpha \frac{L_\alpha}{\lambda_1\lambda_{2\alpha}} = \int_S b_0 dS = b_{ext}\sum_{\alpha=A}^{D}\frac{L_\alpha}{\lambda_1\lambda_{2\alpha}} \text{(the integral are in current configuration)}$$

$$\begin{aligned}
\Pi_{22A} &= \sum_3^5 \frac{\partial W_i}{\partial F_{22}}(\lambda_1, \lambda_{2A}, \tilde{B}_A, b_{0A}) = \lambda_1\frac{b_{ext}^2}{2\mu_0}\\
\Pi_{22B} &= \sum_3^5 \frac{\partial W_i}{\partial F_{22}}(\lambda_1, \lambda_{2B}, \tilde{B}_B, b_{0B}) = \lambda_1\frac{b_{ext}^2}{2\mu_0}\\
\Pi_{22C} &= \sum_3^5 \frac{\partial W_i}{\partial F_{22}}(\lambda_1, \lambda_{2C}, \tilde{B}_C, b_{0C}) = \lambda_1\frac{b_{ext}^2}{2\mu_0}\\
\Pi_{22D} &= \sum_3^5 \frac{\partial W_i}{\partial F_{22}}(\lambda_1, \lambda_{2D}, \tilde{B}_D, b_{0D}) = \lambda_1\frac{b_{ext}^2}{2\mu_0}
\end{aligned} \tag{3.3.3}$$

Where, as shown in Appendix A, and considering a principal solution having a shape $\boldsymbol{F} = \lambda_1\mathbf{e}_1\mathbf{e}_1 + \lambda_2\mathbf{e}_2\mathbf{e}_2$, we get this expression :

$$\begin{aligned}
\frac{\partial W_3}{\partial F_{22}}(\lambda_1, \lambda_{2\alpha}, \tilde{B}_\alpha, b_{0\alpha}) &= \frac{B_\alpha}{\mu_0\lambda_{2\alpha}}\Big(b_{0\alpha} - \frac{B_\alpha}{2\lambda_{2\alpha}\lambda_1}\Big)\\
\frac{\partial W_4}{\partial F_{22}}(\lambda_1, \lambda_{2\alpha}, \tilde{B}_\alpha, b_{0\alpha}) &= G_\alpha\Big(\lambda_{2\alpha} - \frac{1}{\lambda_{2\alpha}}\Big) + \frac{\nu_\alpha}{(1-2\nu_\alpha)}G_\alpha(\lambda_1^2\lambda_{2\alpha} - \lambda_1)\\
\frac{\partial W_5}{\partial F_{22}}(\lambda_1, \lambda_{2\alpha}, \tilde{B}_\alpha, b_{0\alpha}) &= 2\Big(\frac{B}{\lambda_1\lambda_{2\alpha}^2}b_{0\alpha} - \frac{B^2}{\lambda_1^2\lambda_{2\alpha}^3}\Big)\frac{\partial\psi_m}{\partial J_1^*}\Big(\frac{B^2}{\lambda_1^2\lambda_{2\alpha}^2}\Big)
\end{aligned} \tag{3.3.4}$$

The fully coupled problem has to be solved numerically, and this is what we do for all the rest of the chapter. But we provide here the simplified equations for the

small strain case to get a rough idea of the result. Such approximation would be reasonable when λ_1 is close to 1 and the materials are close to incompressibility. Considering Equation 3.3.3 with $\lambda_1 = 1$ and only the lowest order of λ_2, we get for small deformation and arbitrary magnetic field the following simplified system :

$$\begin{aligned}
&\frac{B_B}{\mu_0} + 2B_B\frac{\partial\psi_m}{\partial J_1^*}(B_B^2) - \frac{B_A}{\mu_0} + 2B_A\frac{\partial\psi_m}{\partial J_1^*}(B_A^2) = \kappa \\
&\frac{B_C}{\mu_0} + 2B_C\frac{\partial\psi_m}{\partial J_1^*}(B_C^2) - \frac{B_B}{\mu_0} + 2B_B\frac{\partial\psi_m}{\partial J_1^*}(B_B^2) = \kappa \\
&\frac{B_D}{\mu_0} + 2B_D\frac{\partial\psi_m}{\partial J_1^*}(B_D^2) - \frac{B_C}{\mu_0} + 2B_C\frac{\partial\psi_m}{\partial J_1^*}(B_C^2) = -\kappa \\
&\sum_{\alpha=A}^{D} B_\alpha H_\alpha = b_{ext}\sum_{\alpha=A}^{D} H_\alpha
\end{aligned} \tag{3.3.5}$$

$$\frac{B_A}{\mu_0}\left(b_{0A} - \frac{B_A}{2}\right) + 2G_A(\lambda_{2A} - 1) + \frac{\nu_A}{(1-2\nu_A)}G_A(\lambda_{2A} - 1) + 2B_A(b_{0A} - B_A) = \frac{b_{ext}^2}{2\mu_0}$$

$$\frac{B_B}{\mu_0}\left(b_{0B} - \frac{B_B}{2}\right) + 2G_B(\lambda_{2B} - 1) + \frac{\nu_B}{(1-2\nu_B)}G_B(\lambda_{2B} - 1) + 2B_A(b_{0B} - B_B) = \frac{b_{ext}^2}{2\mu_0}$$

$$\frac{B_C}{\mu_0}(b_{0C} - \frac{B_C}{2}\Big) + 2G_C(\lambda_{2C} - 1) + \frac{\nu_C}{(1-2\nu_C)}G_C(\lambda_{2C} - 1) + 2B_A(b_{0C} - B_C) = \frac{b_{ext}^2}{2\mu_0}$$

$$\frac{B_D}{\mu_0}\left(b_{0D} - \frac{B_D}{2}\right) + 2G_D(\lambda_{2D} - 1) + \frac{\nu_D}{(1-2\nu_D)}G_D(\lambda_{2D} - 1) + 2B_A(b_{0D} - B_D) = \frac{b_{ext}^2}{2\mu_0}$$

Under the small strain assumption, the magnetic equations can be solved separately, decoupling the magnetic and mechanical parts even if the latter still depends on the magnetic solution. However, given the non linear law for magnetisation, solving the problem purely analytically is still very difficult. As previously stated,we now only consider the fully coupled system under finite strain. To illustrate this principal solution, we provide numerical results in one specific case. We consider a steel fiber (E_f = 210 GPa, ν_f = 0.3), a weaker plastic or foam matrix (E_m = 20 MPa and ν_m = 0.4) and a volume fraction of fiber of 10%. For b_{ext}=1T, we provide in Figure 3.3 the values of $\epsilon_{2\alpha} = \lambda_{2\alpha} - 1$ and $b_{2\alpha}$ for various values of current. Similarly, we provide in Figure 3.4 the values of $\epsilon_{2\alpha}$ and $b_{2\alpha}$ for κ = 250000A/m and various values of external magnetic field. The values considered for κ are very high because it is necessary to display significant effect, but those values would lead to thermal

issues as explained in Equation 1.4.2. For a fiber thickness of 1 mm, a maximum value of current density of $10^6 A/m^2$ (as imposed in Chapter 1) would correspond to a maximum value for the current sheet of $10^3 A/m$. The main takeaway is that reasonable values of current will lead to little effects.

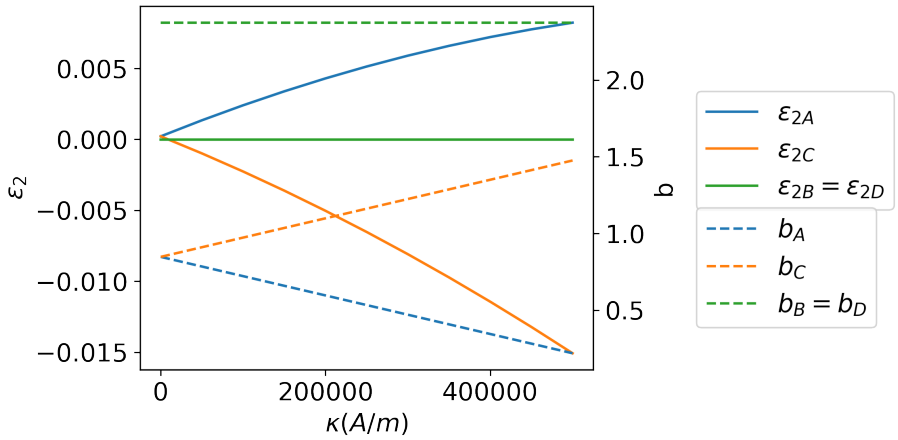

Figure 3.3: Principal solution considering 10% of steel fiber ($E_f = 210$ GPa, $\nu_f = 0.3$) and 90% od plastic matrix ($E_m = 20$ MPa and $\nu_m = 0.4$) for b_{ext}=1T

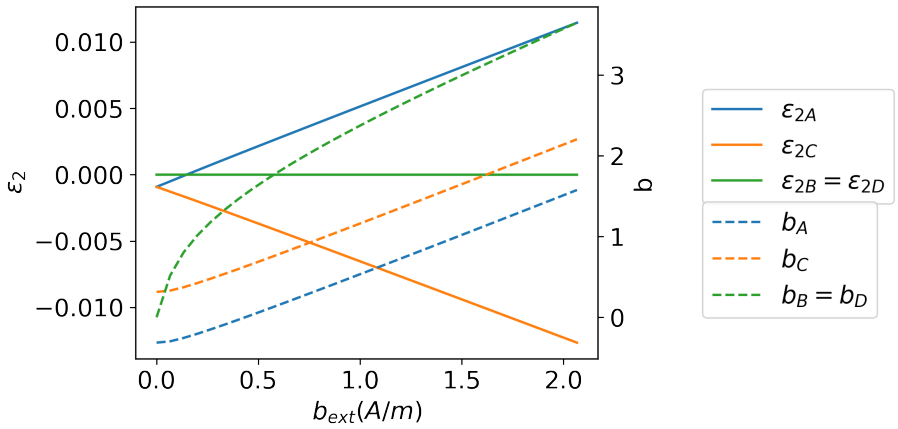

Figure 3.4: Principal solution considering 10% of steel fiber ($E_f = 210$ GPa, $\nu_f = 0.3$) and 90% od plastic matrix ($E_m = 20$ MPa and $\nu_m = 0.4$) for κ=25000A/m

3.4 Stability analysis

3.4.1 Problem simplification

As discussed in Chapter 2, studying the stability of the problem corresponds to looking for non-trivial solutions to the system Equation 3.4.1. Here and subsequently, Latin indexes range from 1 to 2. Einstein's summation convention is implied over repeated indexes unless indicated explicitly.

$$\begin{aligned}
&\left[\left.\frac{\partial^2 P}{\partial F_{ij}\partial F_{kl}}\right|_0(\lambda_1,\kappa,b_{ext})\Delta u_{k,l}+\left.\frac{\partial^2 P}{\partial F_{ij}\partial \tilde{A}_{kl}}\right|_0(\lambda_1,\kappa,b_{ext})\Delta\tilde{A}_{k,l}\right]\delta u_{i,j}=0 \quad \forall i\\
&\left[\left.\frac{\partial^2 P}{\partial \tilde{A}_{ij}\partial F_{kl}}\right|_0(\lambda_1,\kappa,b_{ext})\Delta u_{k,l}+\left.\frac{\partial^2 P}{\partial \tilde{A}_{ij}\partial \tilde{A}_{kl}}\right|_0(\lambda_1,\kappa,b_{ext})\Delta\tilde{A}_{k,l}\right]\delta\tilde{A}_{i,j}=0 \quad \forall i
\end{aligned} \tag{3.4.1}$$

For the sake of clarity, we will now omit the $|_0(\lambda_1,\kappa,b_{ext})$ in the following derivations. As in our problem the magnetic fields are purely in the e_3 direction, we can simplify the problem by not using the magnetic potential but the magnetic field $\tilde{B}=\epsilon_{ij}\tilde{A_{i,j}}$ and $\frac{\partial^2 P}{\partial\tilde{A}_{ij}\partial\tilde{A}_{kl}}=\frac{\partial^2 P}{\partial\tilde{B}\partial\tilde{B}}\epsilon_{ij}\epsilon_{kl}$, $\frac{\partial^2 P}{\partial\tilde{A}_{i,j}\partial F_{kl}}=\frac{\partial^2 P}{\partial\tilde{B}\partial F_{kl}}\epsilon_{ij}$ and $\frac{\partial^2 P}{\partial F_{kl}\partial\tilde{A}_{i,j}}=\frac{\partial^2 P}{\partial F_{kl}\partial\tilde{B}}\epsilon_{ij}$. Then we obtain :

$$\begin{aligned}
&\left[\frac{\partial^2 P}{\partial F_{ij}\partial F_{kl}}\Delta u_{k,l}+\frac{\partial^2 P}{\partial F_{ij}\partial\tilde{B}}\Delta\tilde{B}\right]\delta u_{i,j}=0 \quad \forall i\\
&\left[\frac{\partial^2 P}{\partial\tilde{B}\partial F_{kl}}\Delta u_{k,l}+\frac{\partial^2 P}{\partial\tilde{B}\partial\tilde{B}}\Delta\tilde{B}\right]\delta\tilde{B}=0
\end{aligned} \tag{3.4.2}$$

As the problem has a translation symmetry in X_1, we use a Fourier transform in X_1 that decomposes the solution as a periodic solution in X_1 and a function of only X_2 :

$$\begin{aligned}
\Delta u_i &= exp(i\omega_1 X_1)U_i(X_2)\\
\Delta\tilde{B} &= exp(i\omega_1 X_1)U_3(X_2)
\end{aligned} \tag{3.4.3}$$

Without loss of generality, we consider U_3 real. In general U_i are complex numbers. To further clarify expressions, we will use the following notations

$$\begin{aligned}
L_{uuijkl} &= \frac{\partial^2 P}{\partial F_{ij}\partial F_{kl}}\\
L_{buij} = L_{ubij} &= \frac{\partial^2 P}{\partial F_{ij}\partial\tilde{B}} = \frac{\partial^2 P}{\partial\tilde{B}\partial F_{ij}}\\
L_{bb} &= \frac{\partial^2 P}{\partial\tilde{B}\partial\tilde{B}}
\end{aligned} \tag{3.4.4}$$

First we deal with the specific case where L_{bb}=0. According to Appendix A, it means that $\sum_3^5 4\frac{\partial^2 W_p}{\partial J_1^2}B + 2\frac{\partial W_p}{\partial J_1} = \rho_0 \frac{\partial^2 \phi_m}{\partial J_1^{*2}} \frac{1}{I_2^2} B + 2\rho_0 \frac{\partial \phi_m}{\partial J_1^*} \frac{1}{I_2} + 2\frac{1}{2\mu_0} I_2^{-\frac{1}{2}} = 0$ Using our magnetisation law, we obtain numerically that in theory, for some very specific values of loading parameters, it could indeed be 0. However, in the vast majority of cases we can consider $L_{bb} \neq 0$, and this is what we do in the following. It could lead to some numerical instabilities if we try to solve the system too close from such loading parameters, so in the code we check the value of L_{bb}, but in practice the problem never arises. We now assume that$L_{bb} \neq 0$. Then, using the new notations and integrating by part the first line, we get that :

$$\begin{aligned} &\left[L_{uuijkl}\Delta u_{k,l} + L_{ubij}\Delta\tilde{B}\right]_{,j} = 0 \qquad \forall i \\ &L_{bukl}\Delta u_{k,l} + L_{bb}\Delta\tilde{B} = 0 \end{aligned} \tag{3.4.5}$$

Then, using the periodic decomposition on the second line

$$\begin{aligned} &\left[L_{uuijkl}\Delta u_{k,l} + L_{ubij}\Delta\tilde{B}\right]_{,j} = 0 \qquad \forall i \\ &L_{bu11}i\omega_1 U_1(X_2) + L_{bu12}U_{1,2}(X_2) + L_{bu21}i\omega_1 U_2(X_2) + L_{bu22}U_{2,2}(X_2) + L_{bb}U_3(X_2) = 0 \end{aligned} \tag{3.4.6}$$

Using the Fourier decomposition provided in Equation 3.4.3

$$\begin{aligned} &\left[L_{uuijkl}\Delta u_{k,l} + L_{ubij}\Delta\tilde{B}\right]_{,j} = 0 \qquad \forall i \\ &U_3(X_2) = -\left[L_{bu11}i\omega_1 U_1(X_2) + L_{bu12}U_{1,2}(X_2) + L_{bu21}i\omega_1 U_2(X_2) + L_{bu22}U_{2,2}(X_2)\right]/L_{bb} \end{aligned} \tag{3.4.7}$$

Plugging in the value of $U_3(X_2)$ in the first equations and using the periodic decomposition

$$\begin{aligned} &-\omega_1^2\left[L_{uui1k1}U_k - L_{ubi1}[L_{buk1}U_k]/L_{bb}\right] \\ &+i\omega_1[L_{uui1k2}U_{k,2} - L_{ubi1}L_{buk2}U_{k,2}/L_{bb} + L_{uui2k1}U_{k,2} - L_{ubi2}L_{buk1}U_{k,2}/L_{bb}] \\ &+L_{uui2k2}U_{k,22} - L_{ubi2}[L_{buk2}U_{k,22}]/L_{bb} = 0 \qquad \forall i \\ &U_3 = -[L_{bui1}i\omega_1 U_i + L_{bui2}U_{i,2}]/L_{bb} \end{aligned} \tag{3.4.8}$$

As $L_{ub} = L_{bu}$

$$\begin{aligned} &-\omega_1^2[L_{uui1k1} - \frac{L_{ubi1}L_{buk1}}{L_{bb}}]U_k + i\omega_1[L_{uui1k2} + L_{uui2k1} - 2\frac{L_{ubi1}L_{buk2}}{L_{bb}}]U_{k,2} \\ &+[L_{uui2k2} - \frac{L_{ubi2}L_{buk2}}{L_{bb}}]U_{k,22} = 0 \qquad \forall i \\ &U_3 = -[L_{bui1}\omega_1 U_i + L_{bui2}U_{i,2}]/L_{bb} \end{aligned} \tag{3.4.9}$$

Finally, using $\hat{L}_{uuijkl} = L_{uuijkl} - \dfrac{L_{ubij}L_{bukl}}{L_{bb}}$, we obtain that :

$$-\omega_1^2 \hat{L}_{uui1k1} U_k + i\omega_1 [\hat{L}_{uui1k2} U_{k,2} + \hat{L}_{uui2k1} U_{k,2}] + \hat{L}_{uui2k2} U_{k,22} = 0 \qquad \forall i \quad (3.4.10)$$

We now consider the boundary conditions : First of all, the mechanical continuity of the materials imposes that $[|\Delta u_i|] = 0$. The initial integration by part of the equations leads to :

$$\begin{aligned} &[\![L_{uui2kl} \Delta u_{k,l} + L_{ubi2} \Delta \tilde{B}]\!] = 0 \qquad \forall i \\ &[\![L_{bukl} \Delta u_{k,l} + L_{bb} \Delta \tilde{B}]\!] = 0 \qquad \forall i \end{aligned} \quad (3.4.11)$$

As $\Delta \tilde{B} = -L_{bukl}/L_{bb} \Delta u_{k,l}$ on both sides, the second jump condition is automatically respected and the first relation becomes $[|L_{uui2kl} \Delta u_{k,l} - L_{ubi2} L_{bukl}/L_{bb} \Delta u_{k,l}|] = 0 \forall i$, which corresponds to $[|\hat{L}_{uui2kl} \Delta u_{k,l}|] = 0 \forall i$ To summarize, the boundary condition to respect are

$$\begin{aligned} &[\![\Delta u_i]\!] = 0 \qquad \forall i \\ &[\![\hat{L}_{uui2kl} \Delta u_{k,l}]\!] = 0 \qquad \forall i \end{aligned} \quad (3.4.12)$$

3.4.2 Analytical solution to the stability problem

As we have reduced the problem to an equivalent mechanical problem, we can use the method found in Santisi d'Avila et al. (2016) or Triantafyllidis and Maker (1985) to solve the analytical problem. The method was used in those articles with only 2 different layers, an adaptation of the method for 4 different layers is described here. The interested reader could find a more comprehensive discussion in the previously cited articles. The various buckling modes considered are illustrated in Figure 3.5.

Local modes

We first focus on local modes. Using the Fourier decomposition, the problem to solve is

$$\begin{cases} \omega_1^2 \hat{L}_{uui1k1} U_k - i\omega_1 [\hat{L}_{uui1k2} U_{k,2} + \hat{L}_{uui2k1} U_{k,2}] - \hat{L}_{uui2k2} U_{k,22} = 0 \quad \forall i \\ [\![U_i]\!] = 0 \quad \forall i \\ [\![i\omega \hat{L}_{uui2k1} U_k + \hat{L}_{uui2k2} U_{k,2}]\!] = 0 \qquad \forall i \end{cases} \quad (3.4.13)$$

Using Bloch analysis as described in Chapter 2, the Bloch boundary condition is $U_k(L) = e^{i\omega_2 L} U_k(0)$ with $\omega_2 L \in [0, 2\pi[$ and $H = 2L_f + 2L_m$. L being the vertical of the unit cell. For each layer $\alpha \in \{A, B, C, D\}$, solving Equation 3.4.13 leads to the solution :

$$U_k(X_2) \;=\; \sum_{j=1}^{4} \overset{\alpha\,(j)}{\mathbf{C}_k} \exp\left(i\omega_1 \overset{\alpha}{\mathbf{Z}}_{(j)} X_2 \right) \;;\quad X_2 \in [\textstyle\sum_{\beta=A}^{\alpha-1} L_\beta, \sum_{\beta=A}^{\alpha} L_\beta] \;, \quad (3.4.14)$$

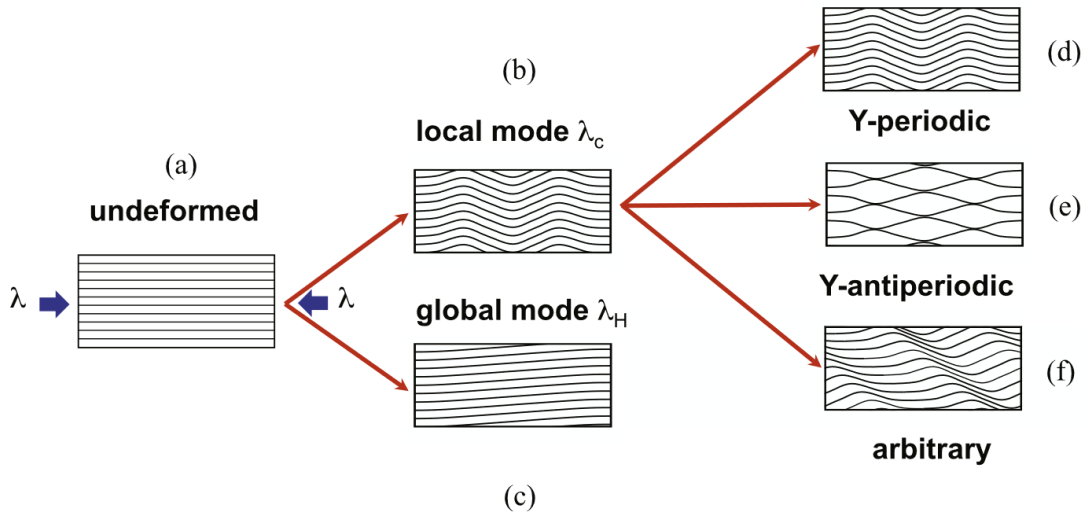

Figure 3.5: Different types of bifurcation modes in axially compressed layered media. Taken from Santisi d'Avila et al. (2016)

The values of $\overset{\alpha}{\mathbf{C}}$ and $\overset{\alpha}{\mathbf{Z}}$ are obtained from the matrix $\overset{\alpha}{\mathbf{M}}(Z) = \overset{\alpha}{\hat{L}}_{i2k2} Z^2 + (\overset{\alpha}{\hat{L}}_{i2k1} + \overset{\alpha}{\hat{L}}_{i1k2}) Z + \overset{\alpha}{\hat{L}}_{i1k1}$. $\overset{\alpha}{\hat{L}}$ is $\hat{L}$ across the layer α, $\overset{\alpha}{\mathbf{Z}}_j$ are the four roots of the determinant of $\overset{\alpha}{\mathbf{M}}$, and $\overset{\alpha}{\mathbf{C}}_j$ is the eigenvector of $\overset{\alpha}{\mathbf{M}}$ associated to $\overset{\alpha}{\mathbf{Z}}_j$. We define $\overset{\alpha}{D}$ as $\overset{\alpha}{D}_j = \overset{\alpha}{C}_{j2} / \overset{\alpha}{C}_{j1}$ with $\overset{\alpha}{C}_{ji}$ the i-th component of the eigenvector $\overset{\alpha}{\mathbf{C}}_j$ We now have to take into account the boundary conditions. As shown in Santisi d'Avila et al. (2016) it can be done using the following method. For each layer we build the three matrix $\overset{\alpha}{\mathbf{Z}}$, $\overset{\alpha}{\mathbf{V}}$ and $\overset{\alpha}{\mathbf{K}}$

according to Equation 3.4.15 :

$$\begin{aligned}
&\overset{\alpha}{\mathbf{V}}_{1j} = 1 \\
&\overset{\alpha}{\mathbf{V}}_{2j} = \overset{\alpha}{D}_{(j)} \\
&\overset{\alpha}{\mathbf{V}}_{3j} = \hat{L}_{1212}\overset{\alpha}{Z}_{(j)} + \hat{L}_{1221}\overset{\alpha}{D}_{(j)} \\
&\overset{\alpha}{\mathbf{V}}_{4j} = \hat{L}_{2211} + \hat{L}_{2222}\overset{\alpha}{Z}_{(j)}\overset{\alpha}{D}_{(j)} \\
&\overset{\alpha}{\mathbf{Z}}_{ij} = \delta_{ij} Z_{(j)} \\
&\overset{\alpha}{\mathbf{K}} = \overset{\alpha}{\mathbf{V}} \exp(i\omega_1 \overset{\alpha}{\mathbf{Z}} \overset{\alpha}{H}) \overset{\alpha}{\mathbf{V}}^{-1}
\end{aligned} \tag{3.4.15}$$

And then,we define the $\mathbf{K}$ matrix by $\mathbf{K} = \overset{D\ C\ B\ A}{\mathbf{K}\mathbf{K}\mathbf{K}\mathbf{K}}$ The stability problem taking into account boundary conditions becomes :

$$det[\mathbf{K}(\lambda_1, b_{ext}, \kappa, \omega_1 L) - exp(i\omega_2 L)\mathbf{I}] = 0 \tag{3.4.16}$$

Finally, to study the stability of the system, we have to look at the two (real) invariants I_1^K and I_2^K define in Equation 3.4.17. It should be noted that those invariants,like $\mathbf{K}$, depends on ω_1, the loadings and the problem parameters, but no longer on ω_2

$$I_1^K \equiv \operatorname{tr} \mathbf{K}\ ,\ I_2^K \equiv \frac{1}{2}\left[(\operatorname{tr}\mathbf{K})^2 - \operatorname{tr}\mathbf{K}^2\right] \tag{3.4.17}$$

The critical local load is reached when one of the conditions in Equation 3.4.18 is reached. The condition reached also provides the value of ω_2 for the buckling mode.

$$\begin{aligned}
&2I_1^K - I_2^K - 2 = 0, && (\omega_2 H)_c = 0, \\
&2I_1^K + I_2^K + 2 = 0, && (\omega_2 H)_c = \pi, \\
&\frac{1}{4}(I_1^K)^2 - I_2^K + 2 = 0 \quad \text{and} |I_1^K| \leq 4 \quad , && (\omega_2 H)_c = \cos^{-1}(I_1^K/4).
\end{aligned} \tag{3.4.18}$$

Long wavelength (global) bifurcation

We now consider global modes ($\omega_1 \to 0$, but $\omega_1 \neq 0$). According to Santisi d'Avila et al. (2016), the stability criteria can be obtain equivalently either by considering

the asymptotic expansion of the local case, or by looking at the loss of rank one convexity of the homogenized incremental moduli L^H. For the sake of completeness the expression for both method are presented here, but when it comes to the results provided later, we only used the homogenized incremental moduli. It is important to point out that the relations given in Santisi d'Avila et al. (2016) stays true only because the main solution is still orthoptic ($\hat{L}_{1211}|_0 = \hat{L}_{1222}|_0 = \hat{L}_{2111}|_0 = \hat{L}_{2122}|_0 = 0$ and corresponding principal symmetries). *Asymptotic expansion* We define the matrix G by doing the asymptotic expansion of K with respect to $\omega_1 H$. Using $\langle\rangle$ as the average of a quantity weighed by volume fraction, Equation 3.4.16 becomes :

$$\det\left[\mathbf{G}(\lambda) - (\omega_2/\omega_1)\,\mathbf{I}\right] = 0\ ;$$

$$G_{11}(\lambda) = G_{22}(\lambda) = G_{33}(\lambda) = G_{44}(\lambda) = 0,$$

$$G_{12}(\lambda) = -\langle \hat{L}_{1221}(\hat{L}_{1212})^{-1}\rangle, \quad G_{21}(\lambda) = -\langle \hat{L}_{1122}(\hat{L}_{2222})^{-1}\rangle,$$

$$G_{13}(\lambda) = \langle (\hat{L}_{1212})^{-1}\rangle, \quad G_{31}(\lambda) = -\langle \hat{L}_{1111} - (\hat{L}_{1122})^2(\hat{L}_{2222})^{-1}\rangle, \tag{3.4.19}$$

$$G_{24}(\lambda) = -\langle (\hat{L}_{2222})^{-1}\rangle, \quad G_{42}(\lambda) = \langle \hat{L}_{2121} - (\hat{L}_{1221})^2(\hat{L}_{1212})^{-1}\rangle,$$

$$G_{34}(\lambda) = \langle \hat{L}_{1122}(\hat{L}_{2222})^{-1}\rangle, \quad G_{43}(\lambda) = \langle \hat{L}_{1221}(\hat{L}_{1212})^{-1}\rangle,$$

$$G_{14}(\lambda) = G_{41}(\lambda) = G_{23}(\lambda) = G_{32}(\lambda) = 0.$$

Then, the invariants becomes:

$$\begin{aligned} I_2^G(\lambda) &= -(G_{12}G_{21} + G_{13}G_{31} + G_{24}G_{42} + G_{34}G_{43})\ , \\ I_4^G(\lambda) &= (G_{12}G_{43} - G_{13}G_{42})(G_{21}G_{34} - G_{31}G_{24})\ . \end{aligned} \tag{3.4.20}$$

And the stability criteria become

$$\begin{aligned} &I_4^G = 0, && (\omega_2/\omega_1)_c = 0, \\ &\frac{1}{4}(I_2^G)^2 - I_4^G = 0, && (\omega_2/\omega_1)_c = \left[-(I_2^G/2)\right]^{1/2}. \end{aligned} \tag{3.4.21}$$

Homogenized incremental moduli The homogenized incremental moduli is

$$\begin{aligned}
\hat{L}^H_{1111}(\lambda) &= \langle \hat{L}_{1111} - (L_{1122})^2 (L_{2222})^{-1} \rangle + \langle L_{1122}(L_{2222})^{-1} \rangle^2 \langle (L_{2222})^{-1} \rangle^{-1}, \\
\hat{L}^H_{1122}(\lambda) &= \langle \hat{L}_{1122}(L_{2222})^{-1} \rangle \langle (L_{2222})^{-1} \rangle = \hat{L}^H_{2211}(\lambda), \\
\hat{L}^H_{2222}(\lambda) &= \langle (\hat{L}_{2222})^{-1} \rangle^{-1}, \\
\hat{L}^H_{2121}(\lambda) &= \langle \hat{L}_{2121} - (L_{1221})^2 (\hat{L}_{1212})^{-1} \rangle + \langle \hat{L}_{1221}(\hat{L}_{1212})^{-1} \rangle^2 \langle (\hat{L}_{1212})^{-1} \rangle^{-1}, \\
\hat{L}^H_{1221}(\lambda) &= \langle \hat{L}_{1221}(\hat{L}_{1212})^{-1} \rangle \langle (\hat{L}_{1212})^{-1} \rangle = \hat{L}^H_{2112}(\lambda), \\
\hat{L}^H_{1212}(\lambda) &= \langle (\hat{L}_{1212})^{-1} \rangle^{-1}.
\end{aligned} \tag{3.4.22}$$

The corresponding invariant are :

$$\begin{aligned}
I^H_2(\lambda) &= (\hat{L}^H_{1111}\hat{L}^H_{2222} + \hat{L}^H_{1212}\hat{L}^H_{2121}) - (\hat{L}^H_{1122}) + \hat{L}^H_{2222})^2 (\hat{L}^H_{1212}\hat{L}^H_{2222})^{-1} \ , \\
I^H_4(\lambda) &= (\hat{L}^H_{1111}\hat{L}^H_{2121})(\hat{L}^H_{1212}\hat{L}^H_{2222})^{-1} \ .
\end{aligned} \tag{3.4.23}$$

Those invariants are equal to the previous ones, i.e $I^G_2(\lambda) = I^H_2(\lambda)$, $\quad I^G_4(\lambda) = I^H_4(\lambda)$

X_1 independent bifurcations

The last type of bifurcation considered are the truly 1D ones, i.e ones obtained when $\omega_1 H = 0$. In this case, using the same governing equations, we get that U_k are piecewise linear functions in X_2 within each layer. A non trivial solution $U_k(0, X_2)$ exists when $\hat{L}_{1212}(\lambda) = 0$ or $\hat{L}_{2222}(\lambda) = 0$ in any layer. Thus the buckling criteria is

$$\overset{\alpha}{\hat{L}}_{1212}(\lambda) = 0, \ \overset{\alpha}{\hat{L}}_{2222}(\lambda) = 0 \tag{3.4.24}$$

However, given the previous relations, and according to Santisi d'Avila et al. (2016), if such critical mode exists it will always be after the homogenized mode, so we no longer consider it.

3.5 Results

3.5.1 Purely mechanical loading

The equations provided in the previous part have to be solved numerically. We do that using the numpy library in python. First, to check our software implementation,

we compare our results to those already available in the literature. We are going to use the results from Triantafyllidis and Maker (1985) that provides the global buckling load, local buckling load and local buckling pulsation for a composite. According to section 4.2 of this article, when considering a Mooney-Rivlin Material (equivalent to our constitutive relation in the incompressible limit), the global mode critical load $\lambda_{1c}(0^+)$ is obtained with the following relations :

$$\begin{aligned} &\lambda_{1c}(0^+) = [(s-1)/s]^{1/4} \\ &s = [(1-\epsilon)/\mu_m + \epsilon/\mu_f][(1-\epsilon)\mu_m + \epsilon\mu_f] \quad (s \geq 1) \\ &V_f = L_f/(L_m + L_f) \end{aligned} \tag{3.5.1}$$

In the incompressible limit ($\nu = 0.49995$) and for a ratio of mechanical stiffness $\mu_m/\mu_f = 0.07$, the results from Triantafyllidis and Maker (1985) are reproduced in Figure 3.6 in solid line. We added our results as red dots (global mode) and green dots (local mode). As expected, those results are very similar. We also compare results

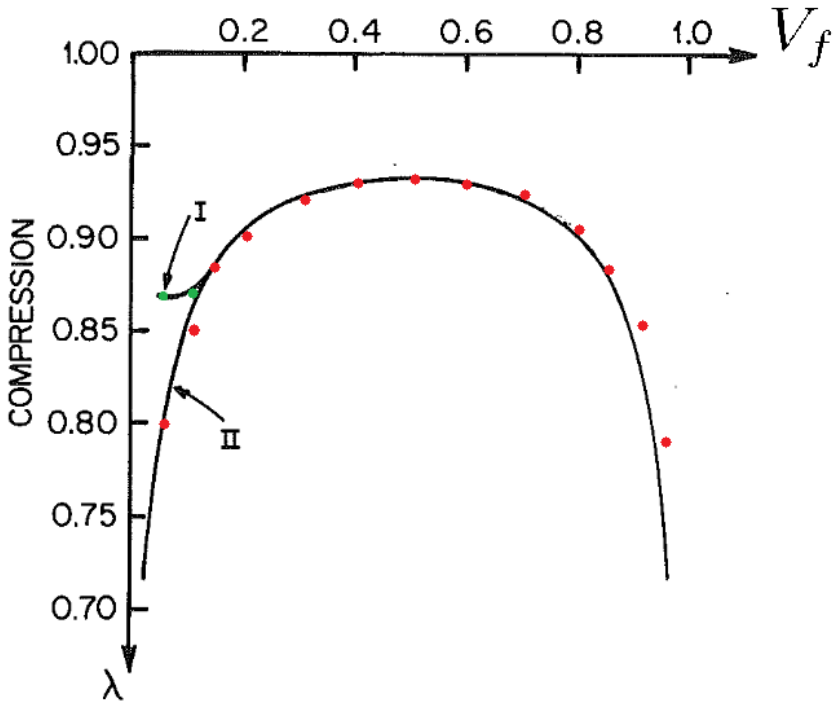

Figure 3.6: Solid line : Dependence of the microscopic (I) and macroscopic (II) critical stretch ratio λ on the fiber volume fraction V_f for the hyperelastic composite with $\mu_m/\mu_f = 0.07$ (Taken from Triantafyllidis and Maker (1985) Fig.6)
Red dots : global buckling results obtained using the previously described method.
Green dots : local buckling results obtained using the previously described method.

with Fig 5 from Triantafyllidis and Maker (1985) that is reproduced in Figure 3.7. It shows the critical compression $\lambda_{1c}(\omega_1)$ to obtain a local critical mode for various values of ω_1 at $V_f = 1/10$ and $\mu_m/\mu_f = 0.07$. The reader should be aware that in the article the definition of H is not similar to ours. To avoid confusion, in this figure we plot our results using the articles definition. The slight differences probably come from our imperfect incompressibility.

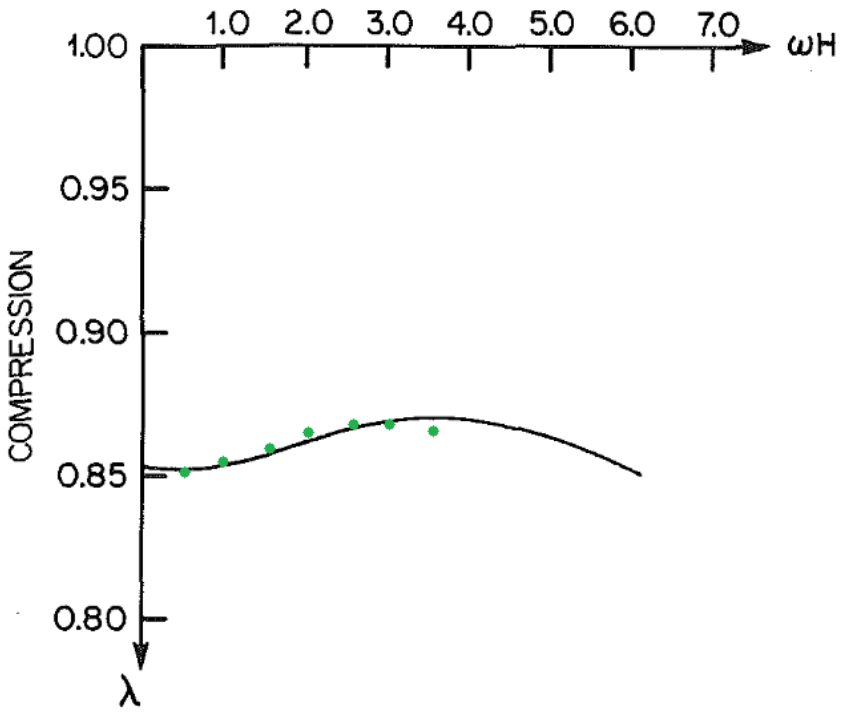

Figure 3.7: Solid line :Dependence of the critical stretch ratio X on the non-dimensionalized eigenmode frequency ω H for the hyperelastic composite with $\mu_m/\mu_f = 0.07$, $V_f = 0.1$ (Taken from Triantafyllidis and Maker (1985) Fig.5)
Green dots : same but using the previously described method.

3.5.2 Electric and magnetic loading under no axial stretch

We now consider the results of the stability analysis under a purely magnetic loading ($\lambda_1 = 1$). We do not expect instabilities as the loading will be purely vertical, which is extremely stable in this geometry. And indeed, for the range of parameters provided in Table 3.1, we detect no instability either global or local. Considering larger loading would not be reasonable given the ranges of validity of the constitutive laws (especially the mechanical one). In detail, we considered a fiber close to steel in properties, thus a Poisson ratio of 0.3 and a Young's modulus of 210 GPa. We considered a wide range of values for the matrix. The matrix Poisson ratio is limited to 0.4999 as numerical stability is fragile for a more incompressible material. The minimum Poisson ratio is taken at 0.1 as materials below that are very uncommon. The matrix Young's modulus is taken between 2 MPa, a value corresponding to the weakest foams, and 100 GPa, a value very close to the fibers one. The volume fraction of fiber considered is above 5% for numerical stability. The maximum value for b_{ext} is given by the electromagnet. The maximum value of κ is far above anything reasonable, it is chosen to show the extreme stability of the system under this loading.

	minimum value tested	maximum value tested
ν_m	0.3	0.4999
E_m (Pa)	2×10^6	1×10^{11}
ν_f	0.3	
E_f (Pa)	2×10^{11}	
V_f	5%	50%
w_1	0.01	100
$b_{ext}(T)$	0	2
$\kappa(A/m)$	0	1×10^8

Table 3.1: range of the various parameters considered when looking for potential buckling mode

3.5.3 Impact of electric and magnetic loading on the buckling caused by axial compression

In this part we focus on the more reasonable case where for a given magnetic loading, we progressively increase axial compression and study both local and global buckling modes. Then we compare the critical λ_{1c} to the case where no magnetic loading is applied. We will consider steel fiber ($E_f = 210$ GPa and $\nu_f = 0.3$) and some weaker plastic or foam ($E_m = 20$ MPa and $\nu_m = 0.4$) *Global mode* First we look

at the global modes for various values of volume ratio of fiber. The results are provided in Figure 3.8 for various magnetic loadings. The key takeaway is that the magnetic loadings can make the material easier to destabilize, but it requires strong magnetic loadings to achieve something significant. In particular, the current seems to have a destabilizing effect, while the external magnetic fields seems to have a smaller stabilizing effect. Overall, the required current is absolutely not thermally reasonable. *Local mode* Doing the same analysis for the local modes, we will provide

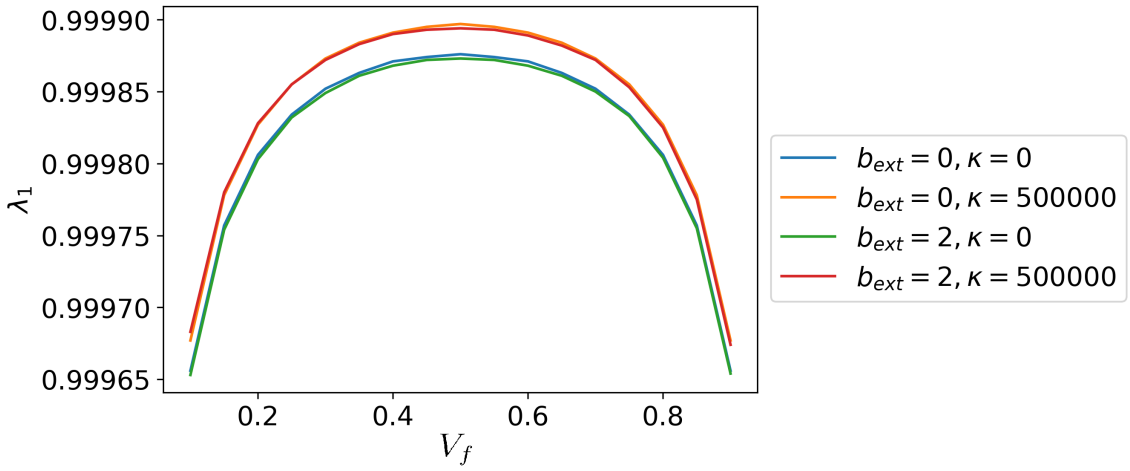

Figure 3.8: Dependence of the macroscopic critical stretch ratio λ_1 on the fiber volume fraction V_f for the hyperelastic composite with ($E_f = 210$ GPa, $\nu_f = 0.3$,$E_m =$ 20 MPa and $\nu_m = 0.4$) for various magnetic loading.

results for $V_f = 0.1$. We consider the same materials. The results are provided for various loadings in Figure 3.9. The results are very similar to the global mode, currents having a small but noticeable destabilizing effect. However the required current is far too high to be reasonable. Once again it is possible to affect the stability of the system in a measurable way, but at the cost of enormous and unreasonable loads. This result stays true for other values of V_f.

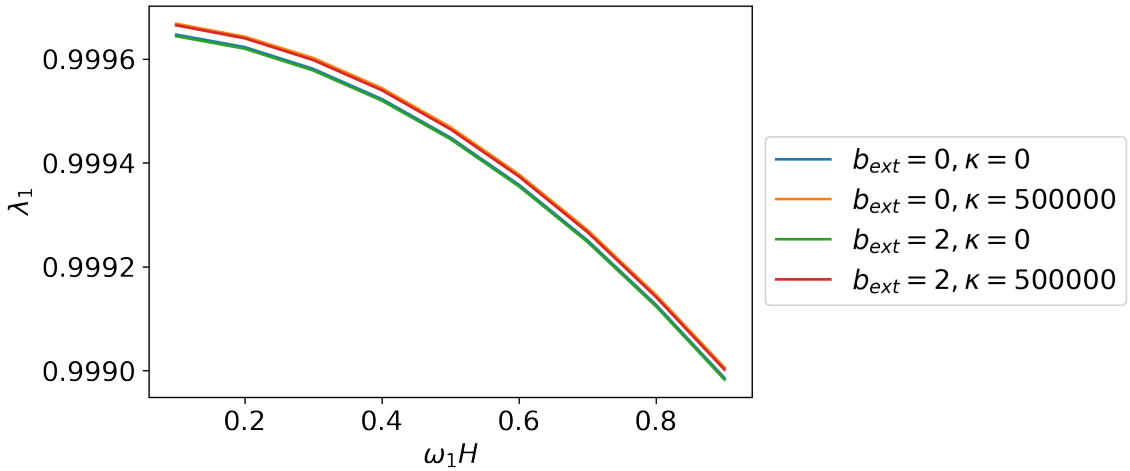

Figure 3.9: Dependence of the macroscopic critical stretch ratio λ_1 on the pulsation ω_1 H for the hyperelastic composite with (E_f = 210 GPa, ν_f = 0.3,E_m = 20 MPa and ν_m = 0.4) for various magnetic loading and a fiber volume fraction V_f of 0.1. The orange line is slightly above the red one. The bleu line is slightly above the green line.

3.6 Conclusion and future work

We provided a detailed analysis of the stability of a 2D composite made of magnetizable conductive fibers and a non conductive matrix under an external magnetic field, currents, and mechanical loadings. Under reasonable electromagnetic loadings as described in Chapter 1, the impact of those on stability is very limited. Given the geometry, the behaviour laws and the directions of the loadings, it is not surprising. As a rule of thumb, the Lorentz forces (without magnetisation) leads to a stress that can be approximated by $b_{ext}\kappa$. For this stress to have a significant impact compared to the Young's modulus (at the very least 10^6 Pa), we need massive surface current. Such high currents are not compatible with the thermal limits derived in Section 1.4, as $\kappa = 10^6$A/m correspond for a fiber of 1mm thickness an equivalent current density of $j = 10^9$A/m that would burn the composite in no time. It must be pointed out that this result is caused by the choice of geometry, as in a different case, namely conductive solenoid, Elliott and Triantafyllidis (2023) obtains significant instabilities for reasonable loadings. However the effect on stability of the electromagnetic loadings in our geometry is strong enough to enable us to test a FE code solving the same problem. The work on this code is largely done, and will be finished in the future. This implementation is straightforward with polynomial quadrilateral elements for both magnetic potential and displacement. To study stability it implements the Bloch theorem with a significant performance improvement described in Triantafyllidis et al. (2005) that enables us to study for each pulsation only the eigenvalues of a system with a size of half the boundary d.o.f.s.

Conclusion

The goal of the current thesis is to explore the possibilities offered by magneto-mechanical metallic metamaterials with non-linear magnetization laws, under both external magnetic fields and electric currents. The novelty of the present work lies in the fact that, to the best of the author's knowledge, no previous work has addressed metamaterials that are both current carrying and magnetizable.

We provide a general, coupled magneto-mechanical model for this problem in Chapter 1, with some adjustment in Chapter 3 for the case when an external magnetic field is imposed in current configuration. As an application to the general theory, two different designs will be considered as simple metamaterials involving electric current-carrying magnetizable conductors subjected to external magnetic fields: a planar grid and a two dimensional layer of metallic sheets separated by elastomeric layers.

- In Chapter 1 we address the problem of the influence of magnetic response of the conductors on the Lorentz forces generated between them for the case of two parallel conductors and also for the case of infinite arrays of parallel conductors. A surprising find of this investigation is that in the case of an infinite array of same direction parallel conductors their magnetic properties have no influence at all, while for an infinite array of alternating direction parallel conductors the Lorentz forces are lower than in the case of non-magnetizable materials!

- In Chapter 2 we study a square unit-cell geometry current-carrying planar truss under an external magnetic field perpendicular to its plane. We investigate the principal solution and its stability and find the instability patterns for an infinite grid.

- Finally in Chapter 3, we investigate the case of a 2D fully coupled composite made of magnetizable conductive layers connected by non-conductive elastomeric layers under an external magnetic field, currents, and mechanical loadings. For this analytically tractable, simple geometry we find that the current, and to a lesser extent the external magnetic field, have only a minor impact on the principal solution and its stability, unlike the imposed axial compression.

With the present thesis we show that using electric currents and magnetic fields to control the behavior of new metamaterials is possible. In the simple geometries

considered here, obtaining significant mechanical effects requires unrealistically high electric currents and magnetic fields. However, different, more complex geometries can be analyzed, where lower currents are required to obtain significant overall mechanical strains, such as in solenoids (see Elliott and Triantafyllidis (2023)). It would be interesting to investigate different composite geometries that might enhance the electro-mechanical coupling and investigate the stability of such designs, based on the general theory proposed here. Finally we would like to offer some general suggestions for potential long-term expansions of the research presented in this thesis. First, one could consider a metamaterial already easy to destabilize, and use the magnetic loadings to nudge the post-bifurcation behavior in one direction rather than the other. By doing so, the limited amplitude of the magnetic forces is no longer an issue. Alternatively, the usage of both electric currents and magnetization while keeping somewhat soft materials could be made possible by using Magnetorheological Elastomers for the magnetization aspect, and pairing them with thin current-carrying wires or sheets. Such a solution would enable the generation of Lorentz forces while minimizing the associated mechanical stiffness. However it would lead to significant thermal limitations.

Appendix A

Complete formulation of the energy in the case of the composite

We provide all the non null derivatives required to solve the problem studied in chapter Chapter 3. First the ones required for the analytical solvers, then the additional terms used in the finite element software

Derivative of I_1 by F_{ij} and $\tilde{B}$

$$\frac{\partial I_1}{\partial F_{kl}} = \frac{\partial I_1}{\partial C_{ij}}\frac{\partial C_{ij}}{\partial F_{kl}} = \delta_{ij}(\delta_{li}F_{kj} + \delta_{lj}F_{ki}) = 2F_{kl}$$
$$\frac{\partial^2 I_1}{\partial F_{ij}\partial F_{kl}} = 2\delta_{ik}\delta_{jl}$$

Derivative of I_2 by F_{ij} and $\tilde{B}$

As $\frac{\partial I_1}{\partial C} = \mathbf{I}_d$ and $\frac{\partial I_2}{\partial C} = I_1\mathbf{I}_d - \mathbf{C}^T$

$$\frac{\partial I_2}{\partial F_{kl}} = \frac{\partial I_2}{\partial C_{ij}}\frac{\partial C_{ij}}{\partial F_{kl}} = (I_1\delta_{ij} - C_{ij})(\delta_{li}F_{kj} + \delta_{lj}F_{ki}) = \sum_o [(I_1\delta_{ol} - C_{ol})]2F_{ko}$$
$$\frac{\partial^2 I_2}{\partial F_{ij}\partial F_{kl}} = (\frac{\partial^2 I_2}{\partial C_{pj}\partial C_{dl}} + \frac{\partial^2 I_2}{\partial C_{pj}\partial C_{ld}} + \frac{\partial^2 I_2}{\partial C_{jp}\partial C_{dl}} + \frac{\partial^2 I_2}{\partial C_{jp}\partial C_{ld}})F_{ip}F_{kq} + (\frac{\partial I_2}{\partial C_{lj}} + \frac{\partial I_2}{\partial C_{jl}})\delta_{ik}$$
$$\text{where} \qquad \frac{\partial^2 I_2}{\partial C_{ij}\partial C_{kl}} = \delta_{ij}\delta_{kl} - \delta_{kj}\delta_{il}$$

Rq : $\frac{\partial I_2}{\partial C}$ is symmetric, however, $\frac{\partial I_2}{\partial C_{pj}\delta C_{dl}}$ only symmetry is exchanging both $p \longleftrightarrow j$ and $d \longleftrightarrow l$

Derivative of B by F_{ij} and $\tilde{B}$

$$\frac{\partial B}{\partial F_{kl}} = \frac{1}{2} I_2^{-1/2} \frac{\partial I_2}{\partial F_{kl}} b_0 = \frac{1}{2} I_2^{-1/2} (\sum_o [(I_1 \delta_{ol} - C_{ol})] 2F_{ko}) b_0$$
$$\frac{\partial B}{\partial \tilde{B}} = 1$$
$$\frac{\partial^2 B}{\partial F^2} = \frac{1}{2} I_2^{-1/2} \frac{\partial I_2^2}{\partial F^2} b_0 + \frac{-1}{4} I_2^{-3/2} \frac{\partial I_2}{\partial F} \frac{\partial I_2}{\partial F} b_0$$

Derivative of J_1 by F_{ij} and $\tilde{B}$

$$\frac{\partial J_1}{\partial F_{kl}} = 2B \frac{\partial B}{\partial F_{kl}} = 2B \frac{1}{2} I_2^{-1/2} (\sum_o [(I_1 \delta_{ol} - C_{ol})] 2F_{ko}) b_0$$
$$\frac{\partial J_1}{\partial \tilde{B}} = 2B \frac{\partial B}{\partial \tilde{B}} = 2B$$
$$\frac{\partial^2 J_1}{\partial F^2} = 2 \frac{\partial B}{\partial F} \frac{\partial B}{\partial F} + 2B \frac{\partial^2 B}{\partial F^2}$$
$$\frac{\partial^2 J_1}{\partial F \partial \tilde{B}} = 2 \frac{\partial B}{\partial F}$$
$$\frac{\partial^2 J_1}{\partial \tilde{B}^2} = 2$$

Derivative of P_5

$$\frac{\partial P_5}{\partial I_2} = \rho_0 \frac{\partial \phi_m}{\partial J_1^*} J_1 \frac{-1}{I_2^2}$$
$$\frac{\partial P_5}{\partial J_1} = \rho_0 \frac{\partial \phi_m}{\partial J_1^*} \frac{1}{I_2}$$
$$\frac{\partial^2 P_5}{\partial I_2^2} = \rho_0 \frac{\partial^2 \phi_m}{\partial J_1^{*2}} \frac{J_1^2}{I_2^4} + \rho_0 \frac{\partial \phi_m}{\partial J_1^*} \frac{2J_1}{I_2^3}$$
$$\frac{\partial^2 P_5}{\partial J_1^2} = \rho_0 \frac{\partial^2 \phi_m}{\partial J_1^{*2}} \frac{1}{I_2^2}$$
$$\frac{\partial^2 P_5}{\partial J_1 \partial I_2} = \rho_0 \frac{\partial^2 \phi_m}{\partial J_1^* \partial J_1^*} J_1 \frac{-1}{I_2^3} + \rho_0 \frac{\partial \phi_m}{\partial J_1^*} \frac{-1}{I_2^2}$$

Derivative of P_4

$$\frac{\partial P_4}{\partial I_1} = \rho_0 \frac{\partial \phi_{el}}{\partial I_1}$$
$$\frac{\partial P_4}{\partial I_2} = \rho_0 \frac{\partial \phi_{el}}{\partial I_2}$$
$$\frac{\partial^2 P_4}{\partial I_1^2} = \rho_0 \frac{\partial^2 \phi_{el}}{\partial I_1^2}$$
$$\frac{\partial^2 P_4}{\partial I_2^2} = \rho_0 \frac{\partial^2 \phi_{el}}{\partial I_2^2}$$
$$\frac{\partial^2 P_4}{\partial I_1 \delta I_2} = \rho_0 \frac{\partial^2 \phi_{el}}{\partial I_1 \partial I_2}$$

Derivative of P_3

$$\frac{\partial P_3}{\partial I_2} = -\frac{J_1}{4\mu_0} I_2^{-\frac{3}{2}}$$
$$\frac{\partial P_3}{\partial J_1} = \frac{1}{2\mu_0} I_2^{-\frac{1}{2}}$$
$$\frac{\partial^2 P_3}{\partial I_2^2} = \frac{3J_1}{8\mu_0} I_2^{-\frac{5}{2}}$$
$$\frac{\partial^2 P_3}{\partial J_1 \partial I_2} = -\frac{1}{4\mu_0} I_2^{-\frac{3}{2}}$$

Full system

We now focus on the terms P_3, P_4, P_5, as P_2 and P_1 are dependent on $\tilde{A}$ dealt with latter.

For any $p \in \{3, 4, 5\}$, the first and second derivatives of the P_p are obtained by using

$$\frac{\partial P_p}{\partial F_{ij}} = \frac{\partial P_p}{\partial I_1}\frac{\partial I_1}{\partial F_{ij}} + \frac{\partial P_p}{\partial I_2}\frac{\partial I_2}{\partial F_{ij}} + \frac{\partial P_p}{\partial J_1}\frac{\partial J_1}{\partial F_{ij}}$$

$$\frac{\partial P_p}{\partial \tilde{B}} = \frac{\partial P_p}{\partial I_1}\frac{\partial I_1}{\partial \tilde{B}} + \frac{\partial P_p}{\partial I_2}\frac{\partial I_2}{\partial \tilde{B}} + \frac{\partial P_p}{\partial J_1}\frac{\partial J_1}{\partial \tilde{B}}$$

$$\frac{\partial^2 P_p}{\partial F_{ij}\partial F_{kl}} = \frac{\partial^2 P_p}{\partial I_1^2}\frac{\partial I_1}{\partial F_{ij}}\frac{\partial I_1}{\partial F_{kl}} + \frac{\partial P_p}{\partial I_1}\frac{\partial^2 I_1}{\partial F_{ij}\partial F_{kl}} + \frac{\partial^2 P_p}{\partial I_2^2}\frac{\partial I_2}{\partial F_{ij}}\frac{\partial I_2}{\partial F_{kl}} + \frac{\partial P_p}{\partial I_2}\frac{\partial^2 I_2}{\partial F_{ij}\partial F_{kl}} + \frac{\partial^2 P_p}{\partial J_1^2}\frac{\partial J_1}{\partial F_{ij}}\frac{\partial J_1}{\partial F_{kl}} + \frac{\partial P_p}{\partial J_1}\frac{\partial^2 J_1}{\partial F_{ij}\partial F_{kl}}$$

$$\frac{\partial^2 P_p}{\partial F_{ij}\partial \tilde{B}} = \frac{\partial^2 P_p}{\partial I_1^2}\frac{\partial I_1}{\partial F_{ij}}\frac{\partial I_1}{\partial \tilde{B}} + \frac{\partial P_p}{\partial I_1}\frac{\partial^2 I_1}{\partial F_{ij}\partial \tilde{B}} + \frac{\partial^2 P_p}{\partial I_2^2}\frac{\partial I_2}{\partial F_{ij}}\frac{\partial I_2}{\partial \tilde{B}} + \frac{\partial P_p}{\partial I_2}\frac{\partial^2 I_2}{\partial F_{ij}\partial \tilde{B}} + \frac{\partial^2 P_p}{\partial J_1^2}\frac{\partial J_1}{\partial F_{ij}}\frac{\partial J_1}{\partial \tilde{B}} + \frac{\partial P_p}{\partial J_1}\frac{\partial^2 J_1}{\partial F_{ij}\partial \tilde{B}}$$

$$\frac{\partial^2 P_p}{\partial \tilde{B}\partial \tilde{B}} = \frac{\partial^2 P_p}{\partial I_1^2}\frac{\partial I_1}{\partial \tilde{B}}\frac{\partial I_1}{\partial \tilde{B}} + \frac{\partial P_p}{\partial I_1}\frac{\partial^2 I_1}{\partial \tilde{B}\partial \tilde{B}} + \frac{\partial^2 P_p}{\partial I_2^2}\frac{\partial I_2}{\partial \tilde{B}}\frac{\partial I_2}{\partial \tilde{B}} + \frac{\partial P_p}{\partial I_2}\frac{\partial^2 I_2}{\partial \tilde{B}\partial \tilde{B}} + \frac{\partial^2 P_p}{\partial J_1^2}\frac{\partial J_1}{\partial \tilde{B}}\frac{\partial J_1}{\partial \tilde{B}} + \frac{\partial P_p}{\partial J_1}\frac{\partial^2 J_1}{\partial \tilde{B}\partial \tilde{B}}$$

Finite element

For the sake of completeness, we add the the expressions for a finite element implementation where N^I are the shape functions and q_i^I the related coefficients.

$$u_i = \sum_I q_i^I N^I(x,y)$$
$$\tilde{A}_i = \sum_I q_{i+2}^I N^I(x,y)$$
$$u_{i,j} = \sum_I q_i^I N_{,j}^I(x,y)$$
$$\tilde{A}_{i,j} = \sum_I q_{i+2}^I N_{,j}^I(x,y)$$

first derivative of F_{ij} and $\tilde{B}$

$$\frac{\partial u_i}{\partial q_m^I} = \delta_{im} N^I(x,y)$$
$$\frac{\partial \tilde{A}_i}{\partial q_{m+2}^I} = \delta_{im} N^I(x,y)$$
$$\frac{\partial \tilde{B}}{\partial q_{m+2}^I} = \frac{\partial \tilde{A}_{2,1}}{\partial q_{m+2}^I} - \frac{\partial \tilde{A}_{1,2}}{\partial q_{m+2}^I} = \delta_{2,m} N^I_{,1}(x,y) - \delta_{1,m} N^I_{,2}(x,y)$$
$$\frac{\partial F_{ij}}{\partial q_m^I} = \frac{\partial u_{i,j}}{\partial q_m^I}$$

first derivative of P_3, P_4, P_5

$$\frac{\partial P_p}{\partial q_m^I} = \frac{\partial P_p}{\partial F_{ij}} \frac{\partial F_{ij}}{\partial q_m^I}$$
$$\frac{\partial P_p}{\partial q_{m+2}^I} = \frac{\partial P_p}{\partial \tilde{B}} \frac{\partial \tilde{B}}{\partial q_m^I}$$
$$\frac{\partial^2 P_p}{\partial q_m^I \partial q_n^J} = \frac{\partial P_p}{\partial F_{ij} \partial F_{kl}} \frac{\partial F_{ij}}{\partial q_m^I} \frac{\partial F_{kl}}{\partial q_n^J}$$
$$\frac{\partial^2 P_p}{\partial q_{m+2}^I \partial q_n^J} = \frac{\partial P_p}{\tilde{B} \partial F_{kl}} \frac{\tilde{B}}{\partial q_{m+2}^I} \frac{\partial F_{kl}}{\partial q_n^J}$$
$$\frac{\partial^2 P_p}{\partial q_{m+2}^I \partial q_{n+2}^J} = \frac{\partial P_p}{\tilde{B}\tilde{B}} \frac{\tilde{B}}{\partial q_{m+2}^I} \frac{\tilde{B}}{\partial q_{n+2}^J}$$

first derivative of P_2

$$\frac{\partial P_2}{\partial q_{m+2}^I} = \frac{\tilde{A}_{1,1} + \tilde{A}_{2,2}}{\xi} \frac{\partial (\tilde{A}_{1,1} + \tilde{A}_{2,2})}{\partial q_{m+2}^I} = \frac{\tilde{A}_{1,1} + \tilde{A}_{2,2}}{\xi} N^I_{,m}(x,y)$$
$$\frac{\partial^2 P_2}{\partial q_{m+2}^I \partial q_{n+2}^J} = \frac{1}{\xi} N^J_{,n}(x,y) N^I_{,m}(x,y)$$

first derivative of P_1

$$\frac{\partial P_1}{\partial q_{m+2}^I} = -\frac{\partial A}{\partial q_{m+2}^I}.J = -\frac{\partial A_1 J_1 + A_2 J_2}{\partial q_{m+2}^I} = -(\delta_{1m} N^I(x,y) J_1 + \delta_{2m} N^I(x,y) J_2) = -N^I(x,y) J_m$$

APPENDIX A. COMPLETE FORMULATION OF THE ENERGY IN THE CASE OF THE COMPOSITE

Résumé en Francais

L'objectif de cette thèse est d'explorer les possibilités offertes par les couplages magnéto-mécaniques dans des métamatériaux métalliques ayant des lois de magnétisation non linéaires, sous l'influence à la fois de champs magnétiques extérieurs, de courants électriques et de chargements mécaniques. La principale nouveauté de ce travail réside, selon les connaissances de l'auteur dans le fait qu'aucun travail antérieur n'a abordé les métamatériaux porteurs de courant électrique et magnétisables.

Nous proposons tout d'abord un modèle général magnéto-mécanique couplé pour ce problème. Les ajustements nécessaires pour le cas où un champ magnétique externe est imposé en configuration déformée et non en configuration de référence sont aussi présentés. Pour traiter des géométries plus complexes, une approche variationnelle est fournie pour une analyse par la méthode des éléments finis. En utilisant cette théorie générale, deux exemples de métamatériaux simples impliquant des conducteurs magnétisables porteurs de courant électrique soumis à des champs magnétiques externes seront considérés : une grille plane et une couche bidimensionnelle de feuilles ferromagnétiques séparées par des couches élastomères.

Dans le premier cas, la grille plane, nous étudions l'effet de la réponse magnétique des conducteurs sur les forces de Lorentz générées, tant pour deux fils conducteurs parallèles que pour un réseau infini de fils conducteurs parallèles. Notre premier résultat est de montrer que, dans ce cas précis, il est possible de découpler les problèmes magnétique et mécanique. Il découle de ce découplage que le calcul des forces électromagnétiques peut être réalisé uniquement à partir d'une intégrale de contour des contraintes électromagnétiques. Les résultats pour un réseau infini de conducteurs parallèles, espacés de manière égale, sont plutôt surprenants, sinon contre-intuitifs. Pour des courants orientés dans la même direction, les propriétés magnétiques des conducteurs n'ont aucune influence sur les forces de Lorentz en raison des arguments de symétrie. Dans le cas où les courants d'un fil sur deux sont orientés dans la direction opposée, les propriétés magnétiques des conducteurs réduisent seulement légèrement les forces de Lorentz en raison des interactions dipolaires, et ces forces dépendent essentiellement de manière linéaire à la fois du champ magnétique et du courant appliqué. Des réseaux plus complexes, multicouches de conducteurs, peuvent être analysés de la même manière.

Utilisant ces résultats, et dans le but d'étudier le comportement mécanique de la grille complète, nous étudions une cellule unitaire rectangulaire sous l'effet des forces de Lorentz calculées précédemment. Nous examinons la solution principale et fournissons une solution analytique. En utilisant le théorème de Bloch, la stabilité peut être étudiée et nous identifions les modes d'instabilité pour une grille infinie. Ces modes, ainsi que leurs chargements critiques, sont cohérents avec ceux estimés par des modèles plus simples. Les valeurs de chargement électromagnétique requises pour obtenir une instabilité ne sont pas atteignables avec nos équipements expérimentaux. Nous avons fait cette analyse de stabilité en supposant que le flambage n'aurait pas de compression à longue portée.

Enfin, nous étudions le cas d'un composite 2D constitué de couches conductrices magnétisables reliées par des couches élastomères non conductrices sous l'effet d'un champ magnétique externe, de courants et de charges mécaniques. Dans ce cas, le problème magnéto- mécanique est traité directement comme un problème couplé. Pour cette géométrie simple, nous sommes capables de fournir une résolution analytique et nous constatons que le courant, et dans une moindre mesure le champ magnétique externe, n'ont qu'un impact mineur sur la solution principale et sa stabilité, contrairement à la compression axiale imposée. Cependant, l'effet sur la stabilité des charges électromagnétiques dans notre géométrie est suffisamment fort pour nous permettre de tester un code par éléments finis résolvant le même problème. Le travail sur ce code est en grande partie réalisé, et sera achevé dans le futur.

En conclusion, cette thèse démontre la possibilité d'utiliser des courants électriques et des champs magnétiques pour contrôler le comportement de nouveaux métamatériaux et fournit les outils nécessaires à cet effet. Dans les configurations simples étudiées, la génération d'effets mécaniques significatifs nécessite des courants électriques et des champs magnétiques irréalistement élevés. Toutefois, des configurations plus complexes pourraient nécessiter des courants plus faibles pour induire des déformations mécaniques significatives. Il serait bénéfique d'explorer différentes géométries composites pour améliorer le couplage électromécanique et d'analyser la stabilité de ces conceptions à partir de la théorie générale proposée.

Bibliography

Anderson, P.I., Moses, A.J., Stanbury, H.J., 2007. Assessment of the stress sensitivity of magnetostriction in grain-oriented silicon steel. IEEE Transactions on Magnetics 43, 3467–3476. doi:10.1109/TMAG.2007.893534.

Aydin, U., Rasilo, P., Martin, F., Singh, D., Daniel, L., Belahcen, A., Rekik, M., Hubert, O., Kouhia, R., Arkkio, A., 2017. Magneto-mechanical modeling of electrical steel sheets. Journal of Magnetism and Magnetic Materials 439, 82–90. URL: https://www.sciencedirect.com/science/article/pii/S0304885317300859, doi:https://doi.org/10.1016/j.jmmm.2017.05.008.

Bao, S., Gu, Y., Fu, M., Zhang, D., Hu, S., 2017. Effect of loading speed on the stress-induced magnetic behavior of ferromagnetic steel. Journal of Magnetism and Magnetic Materials 423, 191–196. URL: https://www.sciencedirect.com/science/article/pii/S0304885316306552, doi:https://doi.org/10.1016/j.jmmm.2016.09.092.

Baudouin, P., Belhadj, A., Breaban, F., Deffontaine, A., Houbaert, Y., 2002. Effects of laser and mechanical cutting modes on the magnetic properties of low and medium si content nonoriented electrical steels. IEEE Transactions on Magnetics 38, 3213–3215. doi:10.1109/TMAG.2002.802418.

Bieńkowski, A., Kulikowski, J., 1980. The magneto-elastic villari effect in ferrites. Journal of Magnetism and Magnetic Materials 19, 120–122. URL: https://www.sciencedirect.com/science/article/pii/0304885380905703, doi:https://doi.org/10.1016/0304-8853(80)90570-3.

Brown, W.F., 1966. Magnetoelastic Interactions. Springer-Verlag, New York.

Budiansky, B., Fleck, N., 1993. Compressive failure of fibre composites. Journal of the Mechanics and Physics of Solids 41, 183–211. URL: https://www.sciencedirect.com/science/article/pii/002250969390068Q, doi:https://doi.org/10.1016/0022-5096(93)90068-Q.

Casperson, L.W., 2002. Forces on permeable conductors in magnetic fields. American Journal of Physics 70, pp. 163 – 168.

Combescure, C., Henry, P., Elliott, R.S., 2016. Post-bifurcation and stability of a finitely strained hexagonal honeycomb subjected to equi-biaxial in-plane loading. International Journal of Solids and Structures 88-89, 296–318. URL: https://www.sciencedirect.com/science/article/pii/S0020768316000780, doi:https://doi.org/10.1016/j.ijsolstr.2016.02.016.

Côté, F., Deshpande, V., Fleck, N., Evans, A., 2004. The out-of-plane compressive behavior of metallic honeycombs. Materials Science and Engineering: A 380, 272–280. URL: https://www.sciencedirect.com/science/article/pii/S0921509304003387, doi:https://doi.org/10.1016/j.msea.2004.03.051.

Côté, F., Russell, B.P., Deshpande, V.S., Fleck, N.A., 2009. The Through-Thickness Compressive Strength of a Composite Sandwich Panel With a Hierarchical Square Honeycomb Sandwich Core. Journal of Applied Mechanics 76, 061004. URL: https://doi.org/10.1115/1.3086436, doi:10.1115/1.3086436.

Danas, K., 2017. Effective response of classical, auxetic and chiral magnetoelastic materials by use of a new variational principle. Journal of the Mechanics and Physics of Solids 105, 25 – 53.

Daniel, L., Hubert, O., 2009. An equivalent stress for the influence of multiaxial stress on the magnetic behavior. Journal of Applied Physics 105. doi:10.1063/1.3068646. cited by: 38.

Elliott, R.S., Triantafyllidis, N., 2023. Mechanical response of metal solenoids subjected to electric currents. Journal of Elasticity URL: https://doi.org/10.1007/s10659-023-10015-y, doi:10.1007/s10659-023-10015-y.

Elliott, R.S., Triantafyllidis, N., Shaw, J.A., 2006. Stability of crystalline solids—i: Continuum and atomic lattice considerations. Journal of the Mechanics and Physics of Solids 54, 161–192. URL: https://www.sciencedirect.com/science/article/pii/S0022509605001468, doi:https://doi.org/10.1016/j.jmps.2005.07.009.

Geymonat, G., Müller, S., Triantafyllidis, N., 1993. Homogenization of nonlinearly elastic materials, microscopic bifurcation and macroscopic loss of rank-one convexity. Archive for Rational Mechanics and Analysis 122, 231–290. URL: https://doi.org/10.1007/BF00380256, doi:10.1007/BF00380256.

Hall, E.H., 1879. On a new action of the magnet on electric currents. American Journal of Mathematics 2, pp. 287–292.

Hammer, J.H., Ryutov, D.D., 1999. Linear stability of an accelerated, current carrying wire array. Physics of Plasmas 6, 3302–3315. URL: https://doi.org/10.1063/1.873598, doi:10.1063/1.873598.

Hanappier, N., 2021. Coupled Electro-Magneto-Thermo-Mechanical Modeling of Electric Motors. Ph.D. thesis. Ecole Polytechnique.

Hanappier, N., Charkaluk, E., Triantafyllidis, N., 2021. A coupled electromagnetic–thermomechanical approach for the modeling of electric motors. Journal of the Mechanics and Physics of Solids 149, 104315.

Hanappier, N., Charkaluk, E., Triantafyllidis, N., 2022. Multiphysics simulation of electric motors with an application to stators. Intl. Journal Solids and Structures 253, 111406–1–111406–14.

Kovetz, A., 2000. Electromagnetic theory. volume 975. Oxford University Press Oxford.

Kumar, R., Senthamaraikannan, P., Saravanakumar, S., Khan, A., Ganesh, K., Vijay Ananth, S., 2020. 8 - electroactive polymer composites and applications, in: Bouhfid, R., el Kacem Qaiss, A., Jawaid, M. (Eds.), Polymer Nanocomposite-Based Smart Materials. Woodhead Publishing. Woodhead Publishing Series in Composites Science and Engineering, pp. 149–156. URL: https://www.sciencedirect.com/science/article/pii/B978008103013400008X, doi:https://doi.org/10.1016/B978-0-08-103013-4.00008-X.

Kyriakides, S., Arseculeratne, R., Perry, E., Liechti, K., 1995. On the compressive failure of fiber reinforced composites. International Journal of Solids and Structures 32, 689–738. URL: https://www.sciencedirect.com/science/article/pii/002076839400157R, doi:https://doi.org/10.1016/0020-7683(94)00157-R. time Dependent Problems in Mechanics.

Lax, M., Nelson, D.F., 1976. Maxwell equations in material form. Phys. Rev. B 13, 1777–1784. URL: https://link.aps.org/doi/10.1103/PhysRevB.13.1777, doi:10.1103/PhysRevB.13.1777.

Lefevre, V., Danas, K., 'Lopez-pamies, O., 2020. Two families of explicit models constructed from a homogenization solution for the magnetoelastic response of mres containing iron and ferrofluid particles. International Journal of Non-Linear Mechanics 119, pp. 103362.

Lopez, S., Cassoret, B., Brudny, J.F., Lefebvre, L., Vincent, J.N., 2009. Grain oriented steel assembly characterization for the development of high efficiency ac rotating electrical machines. IEEE Transactions on Magnetics 45, 4161–4164. doi:10.1109/TMAG.2009.2023243.

Lowes, F.J., 1973. Force on a wire in a magnetic field. Nature 246, pp. 208 – 209.

McDonald, K.T., 2003. Methods of calculating forces on rigid magnetic media. arXiv:physics/0312027.

Müller, S., Triantafyllidis, N., Geymonat, G., 1993. Homogenization of nonlinearly elastic materials, microscopic bifurcation and macroscopic loss of rank-one convexity. Archive for Rational Mechanics and Analysis 122. doi:10.1007/BF00380256.

Pearson, J., Squire, P., Maylin, M., Gore, J., 2000. Biaxial stress effects on the magnetic properties of pure iron. IEEE Transactions on Magnetics 36, 3251 – 3253. doi:10.1109/20.908758. cited by: 35.

Perevertov, O., 2017. Influence of the applied elastic tensile and compressive stress on the hysteresis curves of fe-3% si non-oriented steel. Journal of Magnetism and Magnetic Materials 428, 223–228. URL: https://www.sciencedirect.com/science/article/pii/S0304885316327482, doi:https://doi.org/10.1016/j.jmmm.2016.12.040.

Raposo, V., Garcia, J., González, J., Vázquez, M., 2000. Long-range magnetostatic interactions in arrays of nanowires. Journal of Magnetism and Magnetic Materials 222, 227–232. URL: https://www.sciencedirect.com/science/article/pii/S0304885300005631, doi:https://doi.org/10.1016/S0304-8853(00)00563-1.

Reyne, G., Sabonnadiere, J., Imhoff, J., 1988. Finite element modelling of electromagnetic force densities in dc machines. IEEE Transactions on Magnetics 24, 3171–3173. doi:10.1109/20.92371.

Russell, B., Deshpande, V., Wadley, H., 2008. Quasi-static deformation and failure modes of composite square honeycombs. Journal of Mechanics of Materials and Structures - J MECH MATER STRUCT 3, 1315–1340. doi:10.2140/jomms.2008.3.1315.

Santisi d'Avila, M., Triantafyllidis, N., Wen, G., 2016. Localization of deformation and loss of macroscopic ellipticity in microstructured solids. Journal of the Mechanics and Physics of Solids 97, 275–298. URL: https://www.sciencedirect.com/science/article/pii/S0022509616304677, doi:https://doi.org/10.1016/j.jmps.2016.07.009. sI:Pierre Suquet Symposium.

Schraad, M.W., Triantafyllidis, N., 1997. Scale Effects in Media With Periodic and Nearly Periodic Microstructures, Part II: Failure Mechanisms. Journal of Applied Mechanics 64, 763–771. URL: https://doi.org/10.1115/1.2788980, doi:10.1115/1.2788980.

Slesarenko, V., 2020. Planar mechanical metamaterials with embedded permanent magnets. Materials 13. URL: https://www.mdpi.com/1996-1944/13/6/1313, doi:10.3390/ma13061313.

Surjadi, J.U., Gao, L., Du, H., Li, X., Xiong, X., Fang, N.X., Lu, Y., 2019. Mechanical metamaterials and their engineering applications. Advanced Engineering Materials 21, 1800864. URL: https://onlinelibrary.wiley.com/doi/abs/10.1002/adem.201800864, doi:https://doi.org/10.1002/adem.201800864, arXiv:https://onlinelibrary.wiley.com/doi/pdf/10.1002/adem.201800864.

Tao, Y., Li, W., Wei, K., Duan, S., Wen, W., Chen, L., Pei, Y., Fang, D., 2019. Mechanical properties and energy absorption of 3d printed square hierarchical honeycombs under in-plane axial compression. Composites Part B: Engineering 176, 107219. URL: https://www.sciencedirect.com/science/article/pii/S1359836819302641, doi:https://doi.org/10.1016/j.compositesb.2019.107219.

Thomas, J., Triantafyllidis, N., 2009. On electromagnetic forming processes in finitely strained solids: Theory and examples. Journal of the Mechanics and Physics of Solids 57, 1391 – 1416. URL: http://www.sciencedirect.com/science/article/pii/S0022509609000465, doi:https://doi.org/10.1016/j.jmps.2009.04.004.

Triantafyllidis, N., Maker, B.N., 1985. On the Comparison Between Microscopic and Macroscopic Instability Mechanisms in a Class of Fiber-Reinforced Composites. Journal of Applied Mechanics 52, 794–800. URL: https://doi.org/10.1115/1.3169148, doi:10.1115/1.3169148.

Triantafyllidis, N., Nestorović, M.D., Schraad, M.W., 2005. Failure Surfaces for Finitely Strained Two-Phase Periodic Solids Under General In-Plane Loading. Journal of Applied Mechanics 73, 505–515. URL: https://doi.org/10.1115/1.2126695, doi:10.1115/1.2126695.

Triantafyllidis, N., Schnaidt, W.C., 1993. Comparison of microscopic and macroscopic instabilities in a class of two-dimensional periodic composites. Journal of the Mechanics and Physics of Solids 41, 1533–1565. URL: https://www.sciencedirect.com/science/article/pii/002250969390039I, doi:https://doi.org/10.1016/0022-5096(93)90039-I.

Vogler, T., Hsu, S.Y., Kyriakides, S., 2001. On the initiation and growth of kink bands in fiber composites. part ii: analysis. International Journal of Solids and Structures 38, 2653–2682. URL: https://www.sciencedirect.com/science/article/pii/S002076830000175X, doi:https://doi.org/10.1016/S0020-7683(00)00175-X.

Wang, C., Gao, R., Zhang, H., 2014. Treatment of elastically restrained ends for beam buckling in finite difference, microstructured and nonlocal beam models. Acta Mechanica 226. doi:10.1007/s00707-014-1195-0.

Xue, Z., Hutchinson, J.W., 2006. Crush dynamics of square honeycomb sandwich cores. International Journal for Numerical Methods in Engineering 65, 2221–2245. URL: https://onlinelibrary.wiley.com/doi/abs/10.1002/nme.1535, doi:https://doi.org/10.1002/nme.1535, arXiv:https://onlinelibrary.wiley.com/doi/pdf/10.1002/nme.1535.

INSTITUT POLYTECHNIQUE DE PARIS

Titre : ETUDE THEORIQUE ET EXPERIMENTALE DES MATERIAUX ARCHITECTURES METALLIQUES SOUS CHARGEMENT MECANIQUE ET ELECTROMAGNETIQUE

Mots clés : Probleme en multiphysique ; electromagnetisme ; materiaux architecturés

Résumé : Des développements récents qui ont lieu dans les domaines des meta-matériaux et des couplages magnéto-mécaniques visent à la fois à améliorer des propriétés existantes ainsi que de créer de nouveaux comportements. Le but de cette thèse est d'étudier plus particulièrement les couplages entre matériaux magnétisables, courants électriques et comportements mécaniques. Tout d'abord nous détaillons le modèle multi-physique requis pour traiter ce problème. Lorsque c'est possible une résolution analytique est fournie. Néanmoins, pour traiter des géométries plus complexes une approche variationnelle est fournie pour une analyse par éléments finis. Nous traitons alors deux cas concrets : un treillis partiellement magnétisable et parcouru par des courants unidirectionnels, puis un composite 2D partiellement magnétisable et conducteur. Nous en étudions le comportement sous sollicitation magnétique et mécanique ainsi que leur stabilité.

Title : THEORETICAL & EXPERIMENTAL STUDY OF METALLIC ARCHITECTED MATERIALS UNDER MECHANICAL AND ELECTROMAGNETIC LOADS

Keywords : Multiphysics problem ; electromagnetics ; architected materials

Abstract : Recent developments in the fields of metamaterials and magneto-mechanical couplings aim to both enhance existing properties and create new behaviors. The goal of this thesis is to specifically study the interactions between magnetizable materials, electric currents, and mechanical behaviors. Firstly, we detail the multi-physics model required to address this issue. Whenever possible, an analytical solution is provided. However, to handle more complex geometries, a variational approach is employed for finite element analysis. We then examine two practical cases : a partially magnetizable mesh subjected to unidirectional currents and a partially magnetizable, conductive 2D composite. We investigate their behavior under magnetic and mechanical loading, as well as their stability.

Institut Polytechnique de Paris
91120 Palaiseau, France